ISSN 2435-7499
October 2020

LASTI
Annual Report

Laboratory of Advanced Science and Technology for Industry
University of Hyogo

Vol.21 (2019)

PREFACE

This annual report reviews the research activities of the Laboratory of Advanced Science and Technology for Industry (LASTI) in the academic year of 2019 which is from April 2019 to March 2020) including research activities using NewSUBARU light source at the SPring-8 site and other research activities of the micro and nanoscale are carried out energetically at the Center for Advanced Science and Technology (CAST) II.

NewSUBARU facility has a 1.0-1.5 GeV electron storage ring, which provides light beams from IR to Soft X-ray regions, and the largest synchrotron light facility operated by the university in Japan.

The researches which are carried out are the light sources for next generation through a machine R and D, and the industrial applications such as EUVL lithography, LIGA process, material analysis.

The annual report describes mainly that topics of the NewSUBARU research activities of this year including 1) the research and development of gamma ray application at BL1 beamline, 2) the next generation lithography by Extreme UltraViolet (EUV) lithography at BL3, BL9B, BL9C, and BL10 beamlines, 3) Lithographie, Galvanoformung, and Abformung (LIGA) process technology at BL2 and BL11 beamlines, 4) the chemical analysis using soft X-ray absorption fine structure at (BL5, BL9A, and BL7 beamlines and soft X-ray emission spectroscopy at BL5 and BL9A beamlines at soft X-ray energy region.

Most of our research activities are being conducted in collaboration research works with industries, research institutes, and other universities, inside and outside Japan.

We will continue to respond to the community's demand by offering new science and novel technology.

For the near future planning, the new injector for NewSUBARU are going to construct from August in 2020 to May in 2021. We would like to appreciate Harima RIKEN with their huge contributions. Furthermore, we would like to appreciate the users with their understanding.

Takeo Watanabe

Director of Laboratory of
Advanced Science and
Technology for Industry,
University of Hyogo

Staff of NewSUBARU
(Under the online meeting of LASTI)

The Organization of
Laboratory of Advanced Science and Technology for Industry
University of Hyogo

The organization

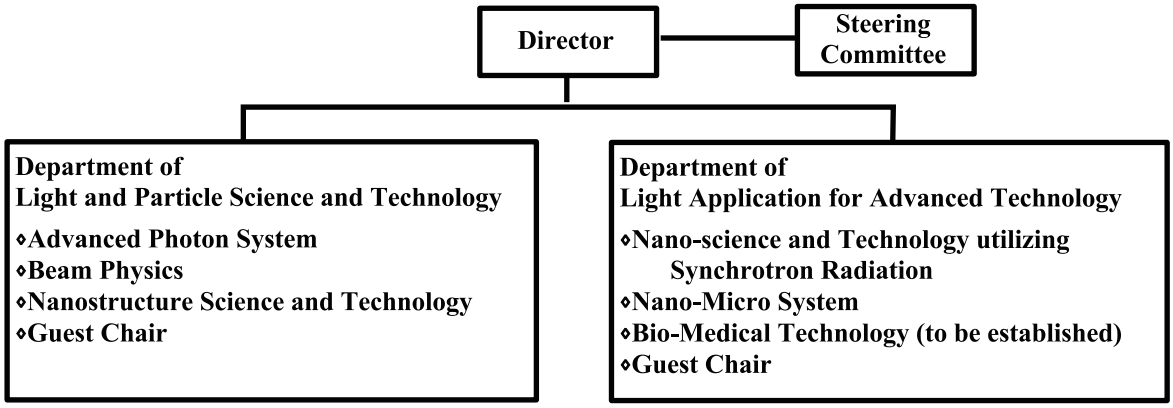

Staff (FY 2019)

Research and faculty staff
WATANABE Takeo, Professor, Director
KANDA Kazuhiro, Professor
UTSUMI Yuichi, Professor
SUZUKI Satoru, Professor
NIIBE Masahito, Associate Professor
SHOJI Yoshihiko, Associate Professor
HARUYAMA Yuichi, Associate Professor
YAMAGUCHI Akinobu, Associate Professor
HASHIMOTO Satoshi, Associate Professor
HARADA Tetsuo, Associate Professor
AMANO Sho, Research Associate

Specially appointed staff
TERANISHI Nobukazu, Professor
MIYAMOTO Shuji, Professor
NAKANISHI Kouji, Associate Professor

Administrative staff
HAYASHI Masahiko, General Manager
ISHIHARA Yasunori, Manager
KAYAHASHI Hidetoshi, Chief
KUWATA Ayami, NewSUBARU
HASEGAWA Miwa, CAST
AKAMATSU Sumiyo, CAST
SAKASHITA Yukiko, CAST
KONO Kimi, CAST
MITOME Naruhito, CAST
SENBA Ayako, CAST
KUSUMOTO Kumi, CAST

Coordinator
MIYAMOTO Shuji, NewSUBARU

Guest staff
MOCHIZUKI Takayasu, Professor
OHKUMA Haruo, Professor
ASANO Yoshihiro, Professor
BAN Hiroshi, Professor
KUDOU Hiroto, Professor
WATANABE Yoshio, Professor
HORIBE Hideo, Professor
HARADA Yoshihisa, Professor
NAMAZU Takahiro, Professor
SUGIYAMA Munehiro, Professor
NAGATA Yutaka, Assistant Professor

Contact address

Advanced Research Building
3-1-2 Kouto, Kamigori-cho, Ako-gun, Hyogo, 678-1205 JAPAN.
T:+81-791-58-0249 F:+81-791-58-0242
NewSUBARU Synchrotron Radiation Facility
1-1-2 Kouto, Kamigori-cho, Ako-gun, Hyogo, 678-1205 JAPAN.
T:+81-791-58-2503 F:+81-791-58-2504
Web URL http://www.lasti.u-hyogo.ac.jp/, http://www.lasti.u-hyogo.ac.jp/NS/
e-Mail lasti@lasti.u-hyogo.ac.jp
Access http://www.lasti.u-hyogo.ac.jp/NS-en/access/

CONTENTS

List of publications

Part 1. Current Status of NewSUBARU and Other Light Source

Klystron Gallery Building

（Completed on March 25, 2019）

NewSUBARU storage ring

Satoshi Hashimoto
LASTI, University of Hyogo

1. Introduction

NewSUBARU synchrotron light facility has a 1.5 GeV electron storage ring, which is the largest accelerator among universities in Japan. The general layout of the ring is shown in Figure 1. The ring is consisted with 6 DBA cells with an inverse bending magnet. There are 6 straight sections between each cell, and they are used for an injection septum, an accelerating RF cavity, two undulators and a laser Compton scattering gamma ray source. Electrons are injected from the linac of SPring-8 through the beam transport line (L4BT). The main parameters are listed in Table I.

Table I Main parameters of the NewSUBARU storage ting

Circumference	118.73 m
Lattice	DBA + inv. Bends
Number of bends	12
Radius of curvature	3.217 m
RF frequency	499.955 MHz
Harmonic number	198
Betatron tunes	6.29(H), 2.22 (V)
Number of IDs	2
Radiation loss per turn	33.4 keV (@1.0GeV)

2. Operation Status

The ring has two operation modes for user-time, 1.0 GeV top-up mode and 1.5 GeV current decay mode. The basic operation time is 9:00 - 21:00 of weekdays. Monday is used for machine R&D, Tuesday is for 1.5 GeV user time, Wednesday and Thursday are for 1.0 GeV top-up user time, Friday is for 1.0 GeV or 1.5 GeV user time. Weekday night and weekend can be used for additional machine study or user time with the special mode, such as a single bunch operation or an operation with arbitrary electron energy. Range of the electron energy is from 0.5 GeV up to 1.48 GeV with 1 MeV step.

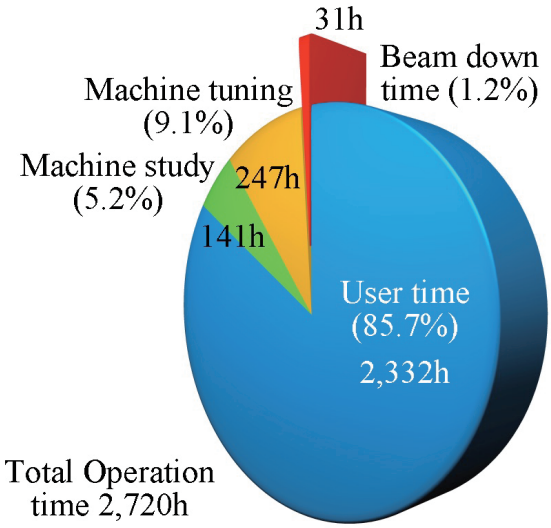

Fig. 2. Operation time of NewSUBARU in FY2019.

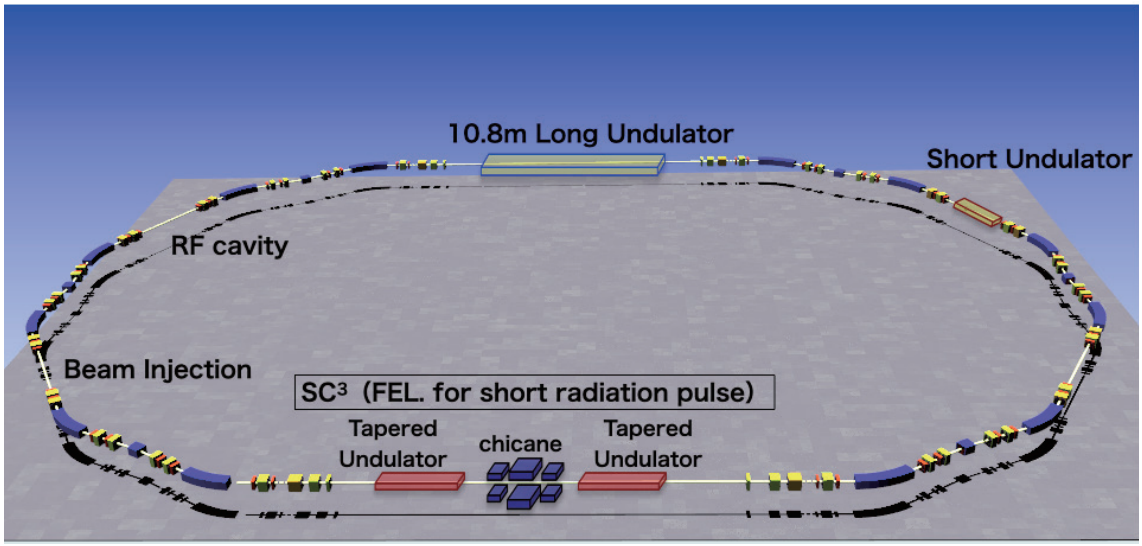

Fig.1. General layout of the NewSUBARU storage ring. Electron beams are injected from the 1.0 GeV linac of SPring-8 to the ring through L4BT beam transport line.

The total machine time in FY2019 was 2,720 hours, 141% of that of FY2018, excluding the beam down time. Figure 2 shows the breakdown of operation time of the electron storage ring. The beam down time includes not only the down by a failure, but also off-beam periods by a beam abort or others due to the beam instability. The total down time due to the machine trouble in FY2019 was 31hours, 1.2 % of the total operation time.

3. Machine Trouble

The typical hardware troubles in FY2019 were as follows.

3-1. Failures of the magnet power supplies.

The current oscillation of bending magnets made beam injection impossible. This was due to the stop of one of several fans located at upper side of the power supply. Temperature rise in the power supply racks caused instability. Repairing the fan made it possible to resume operation.

Power supplies for quadruple magnet families often showed “Heat” alarm at start up time. The current oscillation of sextupole magnets was observed a few times a year. We are planning to update these power supplies.

3-2. Failure of pulsed bump power supply.

At the moment of beam injection, the stored current decreased several times. This was due to aged deterioration of thyratron in a power supply for bump magnets. We are monitoring the future situation.

3-3. Instantaneous voltage drops in facility.

Due to a voltage drop with a relatively long period, the cooling water pumping system in facility was down and a stored beam was aborted due to stop of magnet power supplies and a RF klystron.

3-4. Software bugs and human errors.

The real-time precise measurement and correction system of betatron tune has been developed and started to be used in user-time in 2019. Early in operation of the system, beam aborts occurred a few times due to bugs in software for analyzing betatron signals and for controlling correction coils. The repair of the software defect has been completed and it is now operating normally.

Other beam aborts occurred due to human errors of operators. To avoid mis-operation, we are working on developing a control system that is easy to handle.

3-5. Trouble in beam line interlock system.

A failure of an equipment on radiation safety in a beamline hutch made beam abort a few times.

4. Machine Study

In this section, several topics of the machine R&D are reported.

4-1. SC^3 project (mono-cycle FEL)

Under the collaboration with RIKEN and University of Hyogo Graduate School of Material Science, we are running the SC^3 (Slippage-Controlled Coherent radiation by Chirped micro-bunching) project, where the generation of the extremely short radiation pulse corresponding to only a few wavelengths will be experimentally proved at NewSUBARU using tapered undulators, a magnetic chicane and a chirped seed laser. Main parameters of modulator, radiator and chicane are shown in Table II.

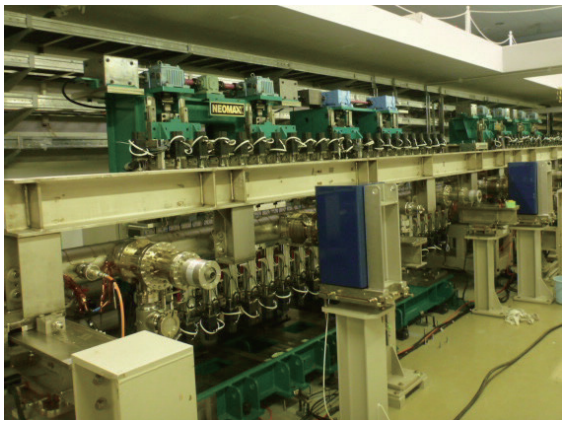

Fig. 3. The new insertion device for generating mono-cycle FEL light pulse. Modulator and radiator with high K parameter and a magnetic chicane between them.

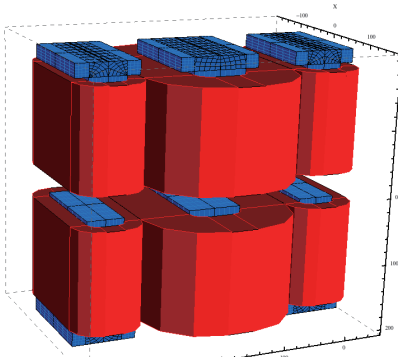

Fig. 4. Chicane magnet of SC3 (field calculation model using RADIA). It consists of one main electromagnet and two sub electromagnets.

The existing insertion device (Optical Klystron) in the 11m long straight section was removed and the new undulators for SC[3] were installed in March 2020 (Fig. 3). We reused the dispersive section as a magnetic chicane of SC3 (Fig.4). Magnetic chicane is. In addition, the seed laser system and the high precision synchronous timing system for Free Electron Laser (FEL) have been installed. The first beam experiment started in April 2020.

Table II Main parameters of SC[3] insertion device.

[Modulator/Radiator]	
magnet	permanent
wavelength	15 cm
Number of periods	24
Total length	7.2 m
Max. field	0.7 T
Max. K parameter	10
Gap	280~50 mm
(gap can be longitudinally tapered)	
[Chicane]	
Magnet	Electromagnet
Number of coils	Main x1, Sub x2
Total length	600 mm
Max. field	0.7 T

4-2. Change of Filling pattern in user-time

The unique point in the operation of our storage ring is using a Full-Fill-like filling pattern. The filling pattern called "70+70 over Full-Fill" shown in Figure 5 has been used in user-time for a long time. Two 70 bunch trains are set over the fully-filled 198 buckets. In general, the "Full-Fill" pattern should not be used in the operation of circular accelerators to avoid beam instabilities such as ion trap instability. However, we used "70+70 over Full-Fill" to meet user's request to increase the stored beam current and to extend the Touschek beam lite-time.

Horizontal and vertical tunes ν_x, ν_y with the two patterns are shown in Figure 6. In the "70+70 over Full-Fill", both horizontal and vertical tunes fluctuate according to the stored current. Furthermore, horizontal tune increases with the current. The beam injection efficiency depends on horizontal tune and is reduced near $\nu_x \sim 0.33$. In the "110 over Full-Fill", on the other hand, the oscillation amplitudes in both horizontal and vertical are relatively small and horizontal drift is also small. Therefore, we have adopted this pattern in usual user-time, with the real-time tune correction system described below.

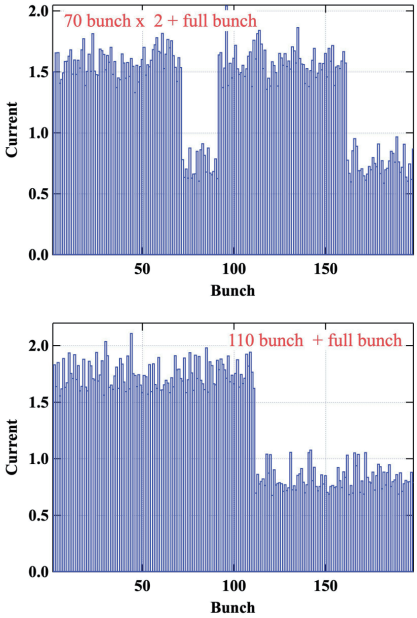

Fig. 5. The filling patterns: "70+70 over Full-Fill" (upper) and "110 over Full-Fill" (lower). The harmonic number is 198.

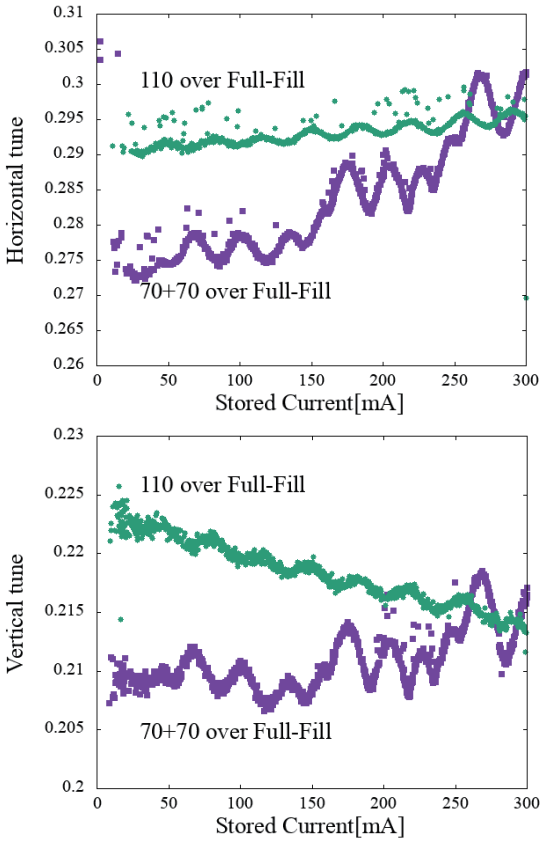

Fig. 6. Horizontal (upper) and vertical (lower) tunes vs. stored current in the two filling patterns. "110+Full-Fill" has smaller amplitude of oscillations.

4-3. Automatic Betatron tune feedback

Betatron tunes drift and fluctuate due to stored current, energy ramping, filling pattern, ID gap and so on. These also depend on the small change of environmental temperatures in a year and a day.

To resolve these problems, we developed the real-time tune measurement and feedback correction system in FY2018 and started using this system during user-time in FY2019. Using this system, the averaged injection efficiency from the linac to the ring could be increased and maintained at 80 to 90 %.

Figure 7 shows changes of horizontal and vertical tunes, and the stored current over time in the 1.5 GeV decay mode. By keeping tunes to optimized values ν_x/ν_y = 0.295/0.215, the beam lifetime could be increased. This system was developed on PXI platform and has been operating stably.

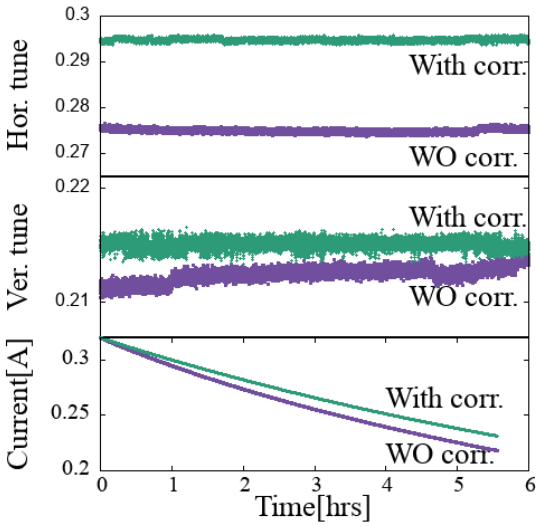

Fig. 7. Changes in horizontal tune (top), vertical tune (middle) and stored current (bottom) over time in the 1.5 GeV decay operation mode. The optimum tunes are ν_x/ν_y = 0.295/0.215.

5. Preparation for Installation of New Injector

Our storage ring has been supplied with electron beams from 1.0 GeV electron linac of SPring-8. However, RIKEN/JASRI decided to shutdown this linac and to inject electron beams from 8.0 GeV linac of SACLA to the main ring. Therefore, a new 1.0 GeV injector is needed, and with the cooperation of RIKEN and JASRI, we are preparing a new linac exclusively for NewSUBARU.

In March 2019 the new building was completed adjacent to the existing L4BT tunnel. This building is used as a klystron gallery for the new 1.0 GeV injector. In FY2019 additional equipment such as crane, cooling water piping, dehumidifier and high precision flat floor for precision alignment of klystrons have been installed. One S-band and four C-band klystrons were installed with the cooperation of RIKEN/JASRI/SES.

In first quarter of FY2020, local RF aging test of klystrons is conducted. Removal of existing equipment and construction of the new linac in L4BT tunnel will begin in August 2020. Until December 2020, the construction of new linac will be completed. After RF aging of klystrons and acceleration tubes of the new linac will be carried out until February 2021. Beam commissioning will begin in March 2021 and user operation will restart in May 2021.

Fig. 8. The new building for klystron gallery of the new injector.

Fig. 9. C-band klystron installed at the klystron gallery for the new injector.

Acknowledgements

We are greatly thanks to Dr. Yasuyuki Minagawa, Mr. Kazuyuki Kajimoto and Mr. Yousuke Hamada of JASRI for stable operation of our facility. We also would like to thanks to all the staff of RIKEN, JASRI and SES for their co-operation in the operation of our facility, the construction of the new building for klystron gallery and the installation work of the new injector.

Beamlines

Masahito Niibe
LASTI, University of Hyogo

The arrangement of the beamlines in the NewSUBARU synchrotron radiation (SR) facility is shown in Fig.1. Total nine beamlines are operating in the NewSUBARU SR facility.

Four beamlines of BL01, 03, 06 and 11 were constructed until 1999. Three beamlines of BL07, 09 and 10 were started the operation from 2000.

BL02 beamline was constructed for the usage of LIGA in 2003.

BL03B beamline branched from the BL03 beamline propose for the usage of the EUVL (extreme ultraviolet lithography) microscope for the EUVL finished mask inspection.

BL05 beamline was constructed in response to a demand in the industrial world in 2008, which is the enhancement of the analysis ability in the soft X-ray region with the development of nanotechnology.

BL09B beamline branched from BL09 beamline for the usage of the EUV interference lithography to evaluate. And BL09C beamline branched from BL09B beamline for the usage of the thickness measurement of the carbon contamination originated to the resist outgassing during the EUV exposure.

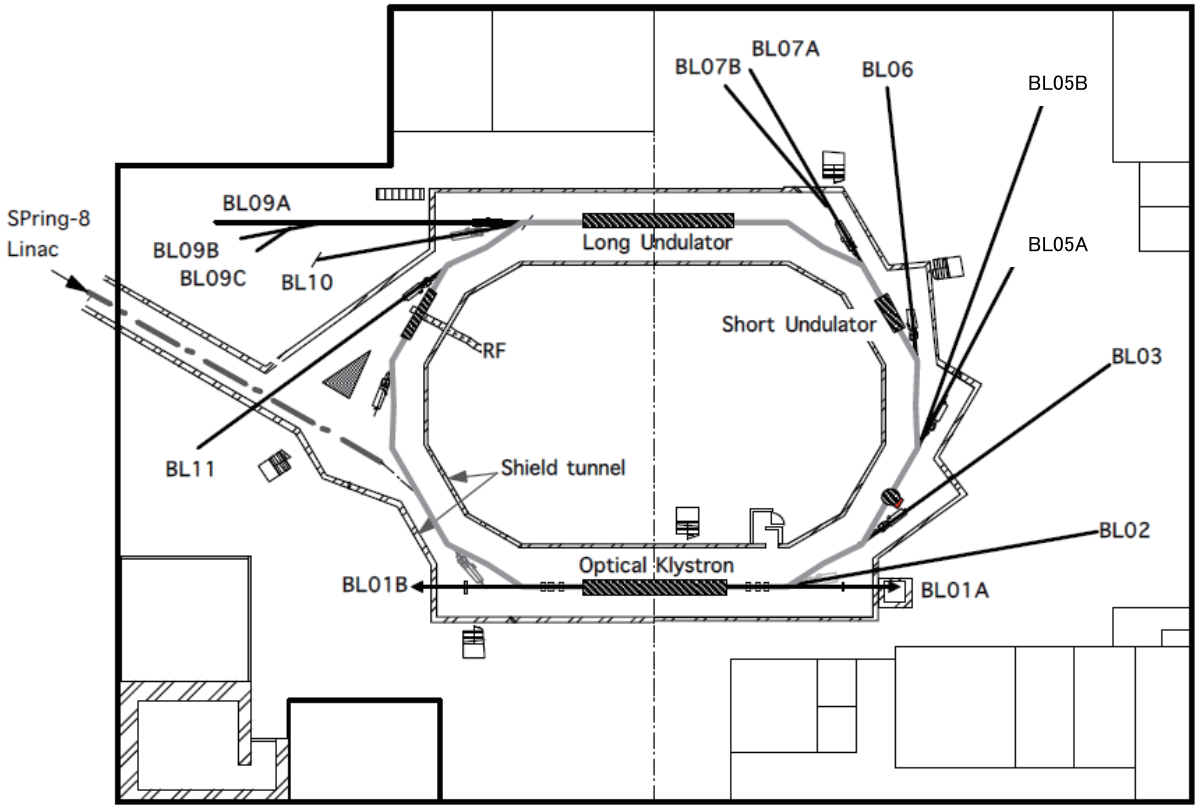

Fig. 1 Beamline arrangement in NewSUBARU.

I. BL01

BL01 is a beamline for research and developing new light sources. This beamline is one of two long straight section on NewSUBARU. Optical klystron was installed at this straight section. Upstream side of this beamline (BL01B) is intended to be used for visible and infrared light generated from free electron laser (FEL) or synchrotron radiation (SR). Downstream side of this beamline (BL01A) is used for laser Compton scattering gamma-rays source. Gamma-ray beamline hutch just outside of the storage ring tunnel was constructed in 2004 for gamma-ray irradiation experiments. Specification of this gamma-ray sources are listed in Table 1. New gamma-ray irradiation hutch "GACKO" was installed at BL01A, collaborating with Konan University. Table 2 shows the specification of "GACKO".

Table 1. Specification of BL01 gamma beam

CO_2 laser 10.52 □m 5W	Gamma energy : 1.7 - 4 MeV Gamma flux* : 9 x106 γ/s : 6 x105 γ/s (1.5-1.7 MeV) (with 3mmφ collimator)
Nd laser 1.064 □m 0.532 □m 5 W	Gamma energy : 17 - 40 MeV Gamma flux* : 7.5 x106 γ/s : 3 x105 γ/s (15-17 MeV) (with 3mmφ collimator)

*Electron beam energy : 1-1.5 GeV
*Electron beam current : 250 mA
*Gamma-ray beam divergence : 0.5 mrad

Table 2. Specification of "GACKO"

Maximum gamma-ray power	0.33 mW
Maximum gamma-ray energy	1.7 MeV - 73 MeV
CO2 laser, wavelength/power	10.59 μm / 10W
1-1.7MeV gamma-ray flux	2×10^7 γ/sec@10W/300mA
Nd:YVO4 laser, wavelength/power	1.064 μm/ 30W, 0.532 μm/20W
10-17 MeV gamma-ray flux	5×10^7 γ/sec@30W/300mA

II. BL02

The LIGA (abbreviated name of Lithogaphic, Galvanoformung and Abformung) process which consists from deep X-ray lithography, electroforming, and molding process is one of the promising candidates for such 3D micofabrication. More than hundreds aspect ratio for microstructure can be attained by the usage of the higher energy X-rays (4-15 keV) from synchrotron radiation (SR) with deeper penetration depth to the photosensitive resist. In this system we have succeeded to enlarge the exposure area up to A4 size and the fabrication dimension from submicron to millimeter by varying the energy of the X-ray source in accordance with the size of desired microparts. Microstructure with high aspect ratio over several hundred will be achieved using the X-rays over 10 keV since high energy X-ray has deep penetration depth to the photo-sensitive resist materials. Whereas, in the case of lithography for low energy X-rays from 1 keV to 2 keV, submicron structures with high aspect ratio will be achieved using the X-rays mask with precise line-width and thinner absorber, since low energy X-rays has low penetration depth. Based on this principle, the beamline for x-ray exposure have constructed with continuous selectivity of X-rays from 100 eV to 15 keV by using the X-ray mirrors (plane and cylindrical mirror) and Be film filters. The horizontal angle of the outgoing SR could be obtained up to 12.5 mrad, which corresponds to the horizontal size of 220 mm (A4 horizontal size) at the exposure position. The second characteristic performance of the beamline is the high efficiency differential pumping system. This was necessary for maintain the vacuum difference between the storage ring ($<10^{-9}$ Pa) and the end-station ($<10^{-9}$ Pa) at which gasses for substrate cooling will be introduced in the exposure apparatus.

The flexibility for the shapes and functions of microstructure will be enlarged by achieving 3D microfabrication process using multi step exposure at various configuration between X-ray mask and

substrates. The relative positions between X-ray mask and substrates, tilt and rotation angle to the SR incident direction can be moved simultaneously during SR exposure using 5 axis stages. The movement of each axis is controlled by the PC in terms of the scanning speeds, scanning length, and repetition number. In order to decrease the heat load of sample substrate suffered during SR irradiation helium introduction and substrate cooling mechanism were also equipped. Specification of spectrometer is listed in Table 3.

Table 3. Specification of the LIGA exposure system

Optics	Plane and cylindrical mirror, Be filters
Exposure energy	100 - 2 keV, and 4 – 15 keV
Exposure method	Proximity and multi-step exposure
Wafer size	A4 or 8 inch
Exposure area	230 mm(H) ×300 mm(V)
Exposure environment	< 1 atm (He-gas)

III. BL03

BL03 is a beamline for the developing the next generation lithographic technology so called extreme ultraviolet (EUV) lithography. The extreme ultraviolet lithography (EUVL) is a promise technology for fabricating a fine pattern less than 7-nm node. There are (1) a EUV resist-sensitivity evaluation tools, (2) a VUV reflectometer, and (3) an EUV microscope with Schwarzschild optics. At (1) tool, EUV resist is exposed with SR light of EUV monochromatized by 7 Mo/Si multilayer mirrors. The exposure spectrum of this tool was same as the ASML exposure tools. The monochromator of (2) reflectometer was UV – VUV reflectometer. At EUV lithography, out-of-band radiation (100 – 300 nm) of EUV source degrades image quality. Thus, optics and resist property of out-of-band region was essential to evaluate, for example EUV mask reflectivity, and EUV resist sensitivity. The monochromator specification was shown in Table 4. The EUV microscope (3) has Schwarzschild optics, which were fabricated with collaboration of Dr. Toyoda (Tohoku Univ.). The spatial resolution was quite high of less than 28 nm, which was equal to 7 nm at wafer printing size.

Table 4. VUV monochromator specification

Mount type	Collimate plane grating monochromator
Grating	Plane Grating (1,000 l/mm)
Energy range	4 - 120 eV (UV ～ VUV)
Resolving power (E/ΔE)	～1000

IV. BL05

BL05 was constructed in response to a demand in the industrial world, which is enhancement of the analysis ability in the soft x-ray region with the development of nanotechnology. BL05 consists of two branch lines for use in the wide range from 50 eV to 4000 eV. BL05A and BL05B are designed to cover the energy range of 1300-4000 eV and 50-1300 eV, respectively. The incident beam from the bending magnet is provided for two branch lines through different windows of a mask. Therefore, these two branch lines can be employed simultaneously. At the end stations of each branch, the transfer vessel systems were mounted for the measurements of sample without exposure to air. In addition, globe box was placed for the preparation of samples into transfer vessel.

1) The double crystal monochromator was installed at the BL05A. InSb, Ge, Si, SiO_2, Beryl and KTP crystals are prepared for a double-crystal monochromator. Toroidal mirrors are used as a pre-mirror and a focusing mirror of BL05A. XAFS measurement in the total electron yield mode and fluorescence XAFS measurement using SSD (SII Vortex) can be performed. The fluorescence XAFS spectra can be measured for samples at the end station

filled with He gas. Table 5 shows the specification of monochromator.

Table 5. Monochromator specification

Monochromator	Double crystal monochromator
Monochromator crystals	SiO2 (1010) , InSb (111) , Ge (111) , Beryl (1010) , KTP (110) , Si (111)
Energy range	1300-4000 eV
Resolution	E/⊿E=3000

2) The constant-deviation monochromator consisting of a demagnifying spherical mirror and a varied-line-spacing plane grating (VLSPG), which can provide high resolution, simple wavelength scanning with fixed slits, was mounted on BL05B. The optical system consists of a first mirror (M0), a second mirror (M1), an entrance slit (S1), a pre-mirror (M2), and three kinds of plane grating (G), an exit slit (S2) and a focusing mirror (M3). The including angle of the monochromator is 175°. Two measurement chambers are prepared at the end station of BL05B. The XAFS spectra in the total electron yield mode and fluorescence XAFS spectra using SDD (Ourstex) can be measured in a high vacuum chamber. In addition, the photoelectron spectrum can be measured using spherical electron analyzer (VG Sienta, R3000) in an ultrahigh-vacuum chamber. The chambers can be replaced by each other within 1 hour. Table 6 shows the specification of the monochromator.

Table 6. Monochromator specification

Monochromator	Varied-line-spacing plane grating monochromator
Grating	100 l/mm, 300 l/mm, 800 mm/l
Energy range	50-1300 eV
Resolution	E/⊿E=3000

V. BL06

BL06 has been mainly developed for irradiation experiments such as photochemical reaction, SR-CVD, photo-etching, surface modification. The white radiation beam from bending magnet is introduced to the sample stage using a pair of mirror, whose incident angle was 3°. The SR at BL06 sample stage had a continuous spectrum from IR to soft x-ray, which was lower than 1 keV. A differential pumping system can be utilized for experiments in a gas atmosphere, which is difficult in the soft x-ray region. A sample holder can install four pieces of samples at a time. By using heater set in the sample holder, the sample can be heated from room temperature to 220°C. The temperature of sample is monitored using a Cr-Al thermocouple mounted on the sample holder.

VI. BL07A and BL07B

This beamline was designed for the development of new materials by SR technology. This beamline consists of two branch lines, which are provided with an incident beam from a 3-m-long undulator by switching the first mirror. One of them is a high photon-flux beamline with a multilayered-mirror monochromator for the study of SR-process (BL07A) and another is a high-resolution beamline with a varied line spacing grating monochromator for the evaluation of nano-structure characteristics by SR-spectroscopy (BL07B). The useful range of emitted photons from 50 to 800 eV is covered at both beamlines. The light source of BL07 is a 3-m length planar undulator, which consists of 29 sets of permanent magnets, a period length of which is 76 mm. The incident beam from the undulator is provided for two branch lines by translational switching of first mirror.

1) BL07A

The multilayered-mirror (MLM) monochromator, which has high reflectivity in the soft X-ray region, was installed at the BL07A. It consists of a switching mirror chamber, a slit chamber, a MLM

monochromator, a filter chamber and a reaction chamber. To obtain a large photon flux, we decided to use only first mirror (switching mirror), M0, for focusing. The MLM monochromator is designed to cover an energy range of up to about 800 eV by combination of three kinds of mirror pairs with 4 kinds of filter. The flux deliver by this design is estimated to be between a maximum of 10^{17} photons/s at 95 eV and a minimum 2×10^{14} photons/s at 300 eV for a 500 mA ring current. Table 7 shows the summary of BL07A. In addition, X-ray fluorescence (XRF) apparatus using spherical varied line spacing grating was mounted at the downstream of irradiation chamber. The poly capillary was used to enhance beam-condensing efficiency. Measurement energy range was from 30 eV to 450 eV. This XRF apparatus was expected to utilize the chemical analysis on the light metals, Li and Be, and light elements, B, C and N.

Two novel vacuum chambers were installed in 2019 for the measurement of inverse Compton scattering of soft X-rays. One large chamber with a size of W1120×D820×H610 mm3 was set up 16.7 m downstream of the undulator center. A multi-layer mirror was placed on high precision auto-stages inside this chamber with cooling water circulation. The other chamber was installed 2.6 m upstream of the large mirror chamber, in order to monitor radiated and reflected X-rays.

Table 7. Summary of BL07A.

Energy range (eV)	Multilayer mirror					Filter	
	Material	spacing	Thickness Ratio	number of layers	ΔE/E	material	Thickness
50-60	Mo/Si	20 nm	0.8	20	6.2 %	Al	100 nm
60-95						None	—
90-140	Mo/B_4C	11 nm	0.5	25	3.3 %		
140-194						Ag	100 nm
190-400	Ni/C	5 nm	0.5	60	2.5 %		
400-560						Cr	500 nm
550-800						Ni	500 nm

2) BL07B

The constant-deviation monochromator consisting of a demagnifying spherical mirror and varied line spacing plane grating (VLSPG), which can provide to high resolution, simple wavelength scanning with fixed slits, was mounted on BL07B. The optical system consists of a first mirror (M0), an entrance slit (S1), a premirror (M1), and three kinds of plane grating (G), an exit slit (S2) and two focusing mirrors (M2 and M3). The monochromator is designed to cover the energy range 50-800 eV with three gratings, of which including angle are 168°. The VLSPG has been well known to obtain high resolution in extreme ultraviolet region by diminishing various kinds of aberration. The total resolving power about 3000 can be realized in the whole energy region. Table 8 shows the specification of the monochromator.

Table 8. Monochromator specification

Mount type	Hettrick-Underwood type
Grating G1, G2, G3	Plane VLS (600, 1200, 2400 l/mm)
Energy range	50-150 eV, 150 – 300 eV, 300-800 eV
Resolving power (E/ΔE)	～3000

VII. BL09

A purpose of this beamline is studies on a soft x-ray interferometry or a holographic exposure experiment with making use of highly brilliant and coherent photon beams radiated from 11 m long undulator in NewSUBARU.

BL09 consists of M0 mirror, M1 mirror, G grating and M2 mirror. M0 mirror is used for horizontal deflection and beam convergence, M1 is used for vertical beam convergence at the exit slit, and M2 is used for vertical deflection and beam convergence. A monochromator is constructed by M1 and a plane grating. The maximum acceptance of the undulator beam is 0.64 mrad in horizontal and 0.27 mrad in vertical. The acceptance can be restricted by 4-jaw slits equipped at upstream of the M0 mirror.

BL09A beamline is used for material analysis: X-ray absorption spectroscopy (XAS) and X-ray photoelectron spectroscopy (XPS). In 2013, X-ray emission spectrometer (XES) was introduced at the end-station of the BL-09A. The energy range and resolving power of the XES system was designed to be about 50-600 eV and 1500, respectively.

BL09B beamline branched from BL09 beamline for the usage of the EUV interference lithography for the evaluation of the exposure characteristics of EUV resist. Coherence length of 1 mm at the resist exposure position was achieved using BL09B beamline. And BL09C beamline branched from BL09B beamline for the usage of the thickness measurement of the carbon contamination originated to the resist outgassing during the EUV exposure. Table 9 shows the specification of the monochromator.

Table 9. Monochromator specification

Mount type	Monk-Gillieson type
Grating	Plane VLS (300, 900, 1200 l/mm)
Energy range	50 – 750 eV
Resolving power (E/ΔE)	～3000

VIII. BL10

BL10 is for EUV reflectometry and soft X-ray analysis. M0 mirror is used for horizontal deflection and beam convergence, M1 is used for vertical beam convergence at the exit slit, and M2 is used for vertical deflection and beam convergence. A monochromator is constructed by M1 and a plane grating. At the beginning, the multilayer reflectivity measurement was carried out at this beamline. The characteristics of this beamline and the result of the Mo/Si multilayer measurement are carried out for the development of the EUV- mask technology.

BL10 utilizes a monochromator of the varied-line-spacing plane grating (VLS-PGM). The line density of the monochromator in central region of the gratings were 600, 1800 and 2,400 lines/mm. The reflectometer has a two axis vacuum goniometer. One axis carries the sample, which may be a mirror surface at the center of the reflectometer vacuum chamber (□-motion). The other (□-motion) carries the detector on a rotating arm. In addition there are linear motions to translate the sample in two orthogonal directions (x,y). All motors are controlled by computer. The reflectivity result obtained at BL10 has a good agreement with that at LBNL. Table 10 shows the specification the monochromator.

The micro-CSM tool was adapted at the most downstream of the BL10 beamline for the EUV mask defect inspection with coherent-diffraction-imaging method. This too is very effective for the inspection of the actinic patterned mask with phase imaging.

A large reflectometer was installed in a branch line for large EUV optical component including EUV collector mirrors. The reflectometer has a sample stage with y, z, □, □, and Tilt axis, which can hold large optical elements with a maximum weight of 50 kg, a diameter of up to 800 mm, and a thickness of 250 mm. The entire sample surface is able to be measured.

Table 10. Monochromator specification

Mount type	Monk-Gillieson type
Grating	Plane VLS (600, 1800, 2400 l/mm)
Energy range	50 – 1,000 eV
Resolving power (E/ΔE)	～1000

IX. BL11

A beam line BL11 is constructed for exposure Hard X-ray Lithography (DXL) in the LIGA (German acronym for Lithographite Galvanoformung and Abformung) process. LIGA process, that utilizes a useful industrial application of SR, is one of the promising technologies for fabrication of extremely tall three-dimensional (3D) microstructures with a large aspect ratio. This process was invented at the Institut Fur Mikrostrukturtechnik (IMT) of the Karlstuhe Nuclear Center (KfK) in 1980. Microstructures with height of over a few hundreds μm have been widely applied to various fields such as micro-mechanics, micro-optics, sensor and actuator technology, chemical, medical and biological engineering, and so on. This beam line was designed by the criteria ; photon energy range from 2 keV to 8 keV, and a density of total irradiated photons □ 10^{11} photons/cm^2. The BL11 can provide the most suitable photon energy for microfabrication in X-ray lithography, while the BL2 is equipped for fabricating fine pattern submicron-scale structure and microstructure with high aspect ratio by selectivity of X-rays using movable mirror system. That is, LIGA process in NewSUBARU can provide the best 3D microfabrication because the BL11 and BL2 are complementary. The beamline BL11 is consisting of an absorber chamber, a first-mirror chamber (M1), a 4-way slit chamber, a Be and polyimide window chamber, and an exposure chamber. The horizontal angle of the outgoing SR could be obtained up to 17.8 mrad, providing a beam spot size on the exposure stage □ 80 □□□□ mm^2. The micron-scale structure with high aspect ratio will be achieved using the toroidal typed mirror M1 which can produce a parallel collimated beam of X-rays. In addition, the homogeneity of the beam is excellently controlled by a novel adding system.

Using the precision stage in the exposure chamber, the flexibility for the shaped and functions of microstructure will be enlarged by achieving 3D microfabrication process using multi step exposure at various configuration between x-ray mask and substrates. The exposure area of 200 mm × 200 mm is brought to fruition. In order to decrease the heat load of sample substrate suffered during SR irradiation, helium introduction and substrate cooling system were also equipped. The specification of the LIGA exposure system is listed in Table 11.

Table 11. Specification of the LIGA exposure system

Exposure method	Proximity exposure
Wafer size	8 inch
Exposure area	200 mm(H)×200 mm(V)
Exposure environment	< 1atm (He-gas)

Establishment of Research Center for Advanced Synchrotron Radiation Analysis

In order to respond to diverse analysis needs from industries, it is necessary to advance technological development for analyzing beamlines (BLs) of NewSUBARU SR facility to advance integrated and strategic development of analyzing technology. For this reason, the Research Center for Advanced SR Analysis was launched in August 2016. As an organization crossing in university courses, this center is consulted and administered by all members of the LASTI related to analysis, and in collaboration with the SR Nanotechnology Center of Hyogo Prefecture, a wide range of energy from hard X-rays to soft X-rays. We aim to respond to various analysis needs of the area on a one-stop basis.

Acknowledgement

We would like to thank all the staff who work at NewSUBARU synchrotron radiation research facility for their help to describe the update details of the beamlines.

Part 2. Research Activities

Mr. Keisuke Tsuda won the Best Academic Poster Presentation Award in “Photomask Japan 2019” (April 18, 2019 Yokohama) "

Photofission and Photoneutron Cross Section Measurements by Neutron-multiplicity Sorting

T. Ari-izumi[1], H. Utsunomiya[1], G. Fan[2], H. Wang[2], D.M. Filipescu[3], M. Bjerke[4], K. Nishio[5], F. Suzaki[5], K. Hirose[5], T. Ohtsuki[6], M. Inagaki[6], I. Gheorghe[3], K. Stopani[7], S. Amano[8], and S. Miyamoto[8]
[1]Konan University, [2]Shanahi Advanced Research Institute, [3]IFIN-HH, [4]University of Oslo, [5]JAEA, [6]Institute for Integrated Radiation and Nuclear Science, Kyoto University, [7]Moscow State University, [8]LASTI, University of Hyogo

Abstract

We have measured photofission and photoneutron cross sections for ^{238}U and ^{232}Th with quasimonochromatic γ-rays produced in the laser Compton scattering. We separate photofission and photoneutron cross sections by direct neutron-multiplicity sorting with a flat-efficiency neutron detector in model dependent and independent analyses. Data reduction is in progress.

Introduction

Nuclear fission has been an important research objective linked to a source of nuclear energy since its discovery in 1938. In the middle of the 20th century, the nuclear response of electric dipole has highlighted the role of photonuclear reactions in the study of giant dipole resonance (GDR); Experiments with the γ-ray source of the positron annihilation in flight at the Lawrence Livermore National Laboratory and Saclay have made major contributions to the photonuclear data compilations [1,2]. At the entrance of the 21st century, photonuclear study has revived by the development of the laser Compton scattering γ-ray source and study of nucleosynthesis in nuclear astrophysics. The International Atomic Energy Agency (IAEA) launched a new project of photonuclear data [3] to update the preceding library [3], leading to the publication of IAEA Photonuclear Data Library 2019 [4]. As an extension of the IAEA library, we measured photofission and photoneutron cross sections with the methodology of direct neutron-multiplicity sorting with a flat-efficiency detector. Both model dependent and independent analyses are in progress to separate photofission and photoneutron cross sections.

Experiments

γ-ray beams in the energy range of 5.86 - 21.12 MeV were produced in laser Compton scattering (LCS) of 1064 nm photons from the INAZUMA Nd:YVO_4 laser on relativistic electrons. Target samples of 8.62 g ThO_2 and 4.06 g U_3O_8 were irradiated with LCS γ-ray beams. Neutrons were detected with a flat-efficiency detector (FED) shown in Fig. 1 that consists of three concentric rings of total 31 ^{3}He proportional counters embedded in a polyethylene moderator. The measurement covered 42 energy points ranging from the fission barrier to above 3n threshold for ^{238}U and ^{232}Th.

Fig. 1 Flat-efficiency neutron detector

The data analysis is based on the methodology of direct neutron-multiplicity sorting with the FED [4]. This methodology enables one to determine (γ,xn) cross sections by solving a set of equations for experimental observables, *i*-fold neutron coincidence events. The innovative methodology has contributed to resolving the long-standing discrepancy between the Livermore and Saclay data of photoneutron cross sections in the IAEA project.

However, there found a problem with the methodology when applied to photofission data. The neutron-multiplicity stays low in photoneutron reactions at energies up to 40 MeV in the investigation of GDR. While the number of neutrons is constrained by neutron thresholds in photoneutron emission, a large number of neutrons can be emitted thermally from fission fragments in prompt photofission

(γ,fxn). Ideally, one must solve a set of equations involving high-order terms of *i*-fold neutron coincidence events with *i* being as high as 9.

The problem is related to poor counting statistics and instability of the set of equations for higher-order terms. Let the highest-order term which is statistically valid be *i*=6. One can write a set of equations as ***N***=***FR***, where ***N*** is a 6 x 1 vector with elements being experimental observables, the number of *i*-fold neutron events N_i (*i* = 1, 2, 3, …, and 6), ***R*** is a 6 x 1 vector with elements being the number of unknown reactions R_j (*j* = 1, 2, 3, …, and 6) that emit *j* neutrons, and ***F*** is a 6 x 6 matrix with elements F_{ij} expressed by $F_{ij} = {}_jC_i\varepsilon^i(1-\varepsilon)^{j-i}$, where ε is the neutron detection efficiency. The number of *i*-fold neutron events N_i is given by $N_i = \sum_j F_{ij}R_j$, where in each of R_j reactions that emit *j* neutrons, we observe *i* neutrons; The number of ways to choose *i* neutrons out of j is ${}_jC_i$; The probability of observing *i* neutrons is ε^i, while that of unobserving ($j-i$) neutrons is $(1-\varepsilon)^{j-i}$.

When one directly solves a set of equations, ***R***=$\boldsymbol{F^{-1}N}$ by using experimental values of ***N*** with large error bars, one obtains ***R*** and resulting cross sections that progressively oscillate between positive and negative values. The set of equations becomes highly unstable to solve with increasing the order of the term because the matrix element F_{ij} in the *i*-th row becomes very small for a large *j*. This is always the case independent of a choice of the highest-order term at which the set of equations is truncated.

The oscillatory problem can be overcome if we solve the set of equation not directly but by introducing an appropriate distribution of neutron-multiplicity (*M*) for photofission. It is customary in the field of nuclear fission [5] to use the Terrell model [6] for the distribution based on the statistical model for the emission of thermal neutrons from fission fragments. The *M* distribution of the Terrell model is similar to the Gaussian distribution with three parameters, a central value, a width, and an absolute normalization.

In the energy region below 2*n* threshold, for example, the cross section with *M*=1 represents a sum of (γ,1n) and (γ,f1n) cross sections, while the cross section with $M \geqq 2$ stems from fission. Thus, the set of equations ***N***=***FR*** can be solved by means of the least-squares fitting with three parameters of the Terrell model for (γ,fxn) with $x \geqq 2$ and one parameter for (γ,1n). In this way, we can separate photofission and photoneutron cross sections. We performed a least-squares fitting in the set of equations ***N***=***FR*** with ***F*** extended to a 6 x 9 matrix to obtain preliminary ***R*** and corresponding cross sections which we refer to as model-dependent cross sections.

As the next step of data reduction, we challenge to deducing photofission and photoneutron cross section in a model-independent way on the basis of experimental histograms corresponding to detection times of *i*-th neutrons out of *j*-fold neutron events in our neutron detection system, taking into account multiple firings of photoneuron and photofission reactions.

References

[1] B.L. Berman, S.C. Fultz, Rev. Modern Phys. 47 (1975) pp. 713-761.

[2] S.S. Dietrich, B.L. Berman, At. Data Nucl. Data Tables 38 (1988) pp. 199-338.

[3] IAEA-TECDOC-1178 IAEA, October, 2000.

[4] T. Kawano *et al*., Nuclear Data Sheets 163, (2020) pp. 109-162.

[5] J.T. Caldwell, E.J. Dowdy, R.A. Alvarez, B.L. Berman, P. Meyer, Nucl. Sci. Eng. 73 (1980) pp. 153-163.

[6] J. Terrell, Phys. Rev. 108 (1957) 783.

Spatial and Energy Profiles of Laser Compton-scattering γ-ray Beams

M. Kiniwa[1], T. Goto[1], S. Tanaka[1], K. Ohgaki[1], K. Kasahara[1],
T. Ari-izumi[1], H. Utsunomiya[1], S. Amano[2], and S. Miyamoto[2]
[1]Konan University, [2]LASTI, University of Hyogo

Abstract

γ-ray beams were produced in inverse Compton scattering of laser photons on relativistic electrons. Spatial profiles of laser Compton-scattering γ-ray beams were measured with a MiniPIX X-ray camera. Energy profiles were investigated by measuring γ-ray beams with $LaBe_3$(Ce) and NaI(Tl) detectors. A consistent understanding of spatial and energy profiles is necessary in terms of the electron beam emittance.

Introduction

The spatial and energy profiles are two important characteristics of γ-ray beams produced in laser Compton scattering (LCS). The former profile determines the size of materials to be irradiated, while the latter defines energy monochromaticy of LCS γ-rays with which photonuclear reactions are induced.

We usually determine the energy profile by measuring LCS γ-rays with a large-volume $LaBr_3$(Ce) detector [1]. Response functions of the profile-monitor detector to LCS γ-rays are analyzed with a GEANT4 code that incorporates the kinematics of laser Compton scattering. By reproducing experimental response functions, best-fit values of the electron-beam emittance are obtained with which one can determine the energy distribution of the LCS γ-ray beam.

In contrast to the energy profile, the spatial profile of the LCS γ-ray beam has sparsely been investigated. We carried out a systematic investigation of the spatial and energy profiles of the LCS γ-ray beam.

Experiments

γ-ray beams were produced in scatterings of 1064 nm photons from the INAZUMA Nd:YVO_4 laser on relativistic electrons at energies (E_e) from 549 to 1460 MeV, 10.59μm photons from a CO_2 laser at E_e = 974 and 1460 MeV and 532 nm photons from the Talon laser at E_e = 974 MeV. Two collimators each made of 10-cm-thick Pb with an aperture of 3-mm and 2-mm diameters, respectively, were located at 1547 m and 1847 m from the most efficient collision point between laser photons and electrons. Response functions to LCS γ-rays produced with the INAZUMA laser were measured with a 3.5" x 8.0" $LaBr_3$(Ce) detector except at 549 MeV. Spatial profiles of all LCS γ-rays were measured with a MiniPIX X-ray camera with 256 x 256 pixels and the pixel pitch 55μm [2].

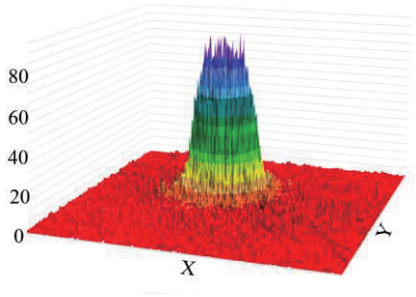

Fig.1 3d spatial profile of 17 MeV LCS γ-rays

Figure 1 shows a 3d spatial profile of the 17 MeV γ-rays produced at E_e = 974 MeV. Horizontal and vertical distributions obtained by projecting the 3d profile on x and y axes are shown in Figs. 2 and 3, respectively.

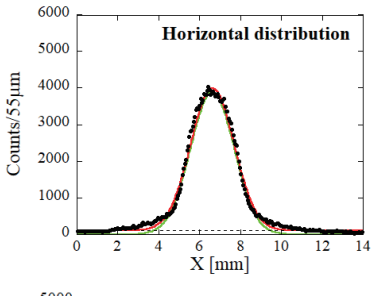

Fig. 2 Horizontal distribution of 17 MeV LCS γ-rays

The horizontal and vertical distributions are well reproduced with a Gaussian function plus constant background. The standard deviation (σ) of the Gaussian function is 1.07 mm corresponding to 2.52 mm in full width at half

maximum (FWHM) for the horizontal distribution and 1.01 mm corresponding to 2.36 mm in FWHM for the vertical distribution, showing a slightly elliptical shape.

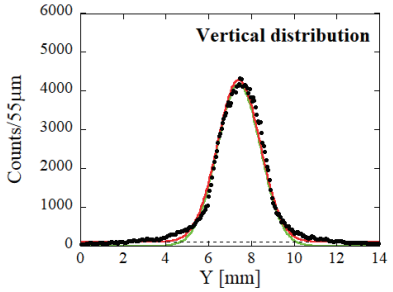

Fig. 3 Vertical distribution of 17 MeV LCS γ-rays

Figure 4 shows the dependence of the experimental FWHM value on the γ-ray energy for the horizontal and vertical distributions. One

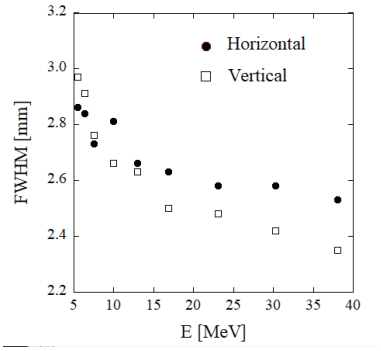

Fig. 4 Experimental value of FWHM for the horizontal and vertical distributions as a function of LCS γ-ray energy

may see that the FWHM apparently depends on the γ-ray energy. The lower the γ-ray energy, the larger the FWHM. However, this energy dependence cannot take place in view of the fact that γ-ray photons behave as particles unlike classical waves that undergo diffraction, being independent of their energies. In other words, the size of the LCS γ-ray beam is geometrically determined by the size of the γ-ray emitting source, the location and aperture of the collimator, and finally the location of observing the LCS γ-ray beam. The larger the size of the γ-ray emitting source, the larger the size of the LCS γ-ray beam at the observation point.

The size of the γ-ray emitting source is defined by the electron beam size in the laser Compton scattering. The electron beam size in standard deviation of the Gaussian function is 0.3 mm horizontally and 0.18 mm vertically at the collision point between 1064 nm laser photons and 974 MeV electrons [3]. Therefore, the apparent dependence of the spatial profile on the γ-ray energy shown in Fig. 4 should be reinterpreted as the dependence on the electron beam size. Namely, Fig. 4 suggests that the electron beam size increases with decreasing the electron beam energy in the storage ring.

Our study of the energy profile of the LCS γ-ray beam shows that the electron beam emittance (ε) increases with decreasing the electron beam energy. Horizontal (ε_x) and vertical (ε_y) emittances obtained in the present study are shown in Fig. 5. The emittance characterizes the spatial size and angular dispersion of the electron beam. The nominal value is ε_x = 5 x 10^{-5} mmrad and ε_y = 5 x 10^{-6} mmrad at E_e = 974 MeV [4].

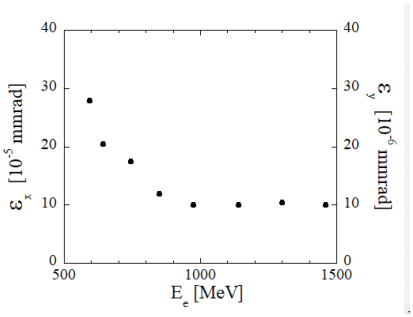

Fig. 5 Horizontal and vertical electron beam emittances as a function of the beam energy

By combining the experimental information on the spatial profile of the LCS γ-ray beam which reflects the size of the electron beam and on the energy profile which reflects the emittance, we can pin down the spatial size and angular dispersion of the electron beam in the interaction region of laser photons with relativistic electrons in the storage ring.

References

[1] T. Kawano *et al*., Nuclear Data Sheets 163, (2020) pp. 109-162.
[2] https://advacam.com/camera/minipix-tpx3
[3] S. Amano *et al*., Nucl. Instrum. Meth. A602, (2009) pp. 337 – 341.
[4] https://www.lasti.u-hyogo.ac.jp/NS/facility/ring/para.html

Study of low-energy dipole strength in neutron-rich nickel isotopes observed via (γ, n) reaction near neutron threshold

D. Arimizu[1], H. Ikoma[1], N. Ogata[1], N. Ogio[1], R. Tsuji[1], K. Tsutsumi[1], S. Yamammura[1], Y. Hijikata[1], A. Sakaue[1], H. Utsunomiya[2], T. Ari-izumi[2], S. Miyamoto[3], K. Yoshida[1], Y. Kanada[1], and J. Zenihiro[1].
[1]Kyoto University, [2]Konan University, [3]LASTI, University of Hyogo

Abstract

To investigate the neutron skin structure in a neutron-rich nucleus, we measured photoneutron cross sections for ^{58,64}Ni above neutron threshold energy by using quasimonochromatic gamma ray beams. Liquid scintillator arrays were used to detect emitted neutrons from (γ, n) reaction. By utilizing TOF technique with a single-bunch mode of the storage ring, neutron energy spectra were also obtained.

Introduction

Understanding the equation of state (EOS) of nuclear matter is one of the most important issues in modern nuclear physics. Especially, so-called symmetry energy parameters, which characterize the pure neutron matter like neutron stars, are now known to be strongly correlated with neutron skin of finite neutron-rich nuclei. Excess neutrons are pushed out to the nuclear surface, forming a region where only neutrons exist. This is called “neutron skin”.

Recently, in the measurement of the E1 transition strengths of neutron-rich nuclei including unstable ones, concentrations of transition strength near the neutron emission threshold were observed. Several theoretical studies suggest that this low-energy E1 resonance is interpreted as an oscillation mode of core and neutron skin. Therefore, the measurement of E1 strength near the neutron threshold can be a probe to extract the neutron skin structure. In fact, theoretical calculations for various nuclei in the Hartree-Fock plus random-phase approximation with several Skyrme interactions were performed and the clear emergences of low-energy E1 are predicted [1]. Thus, we proposed an experiment to measure the precise structure of the E1 mode of ^{64}Ni above the neutron threshold at BL01 beam line in the NewSUBARU storage ring facility.

Experiment

Measurements were performed at BL01 beam line in February 2020. We utilized the quasimonochromatic gamma ray beams, which were produced by the inverse laser Compton scattering (LCS) from electrons circulating in the storage ring. 1GeV electron beams were injected from a linear accelerator into the ring. We used a single-bunch mode to measure time of flight (TOF) information of emitted neutrons, which enables the clear particle identification and the energy spectrum measurements. A typical current of stored single-bunch electrons was 30 mA and its lifetime is about 3 hours. A Nd:YVO4 laser system (Inazuma) provided linearly polarized laser photons with a pulse length of 60 ns and a wavelength of 1064 nm. The energy of electrons was changed from 764 MeV to 974 MeV, which corresponds to LCS gamma ray beam energy from 10 MeV to 16.6 MeV. The LCS gamma ray beams were collimated by two lead blocks with 6 and 4 mm-diameter holes in the BL01 beamline. Collimated beams were finally transported to the nickel isotope target (^{58,64}Ni : 2.58 and 1.16 mm-thick) in the experimental hutch, GACKO (Gamma Collaboration Hutch of Konan University). Emitted neutrons from (γ, n) reaction above neutron thresholds (^{58,64}Ni : 12.22 and 9.66 MeV) were measured with three liquid scintillation (LS) detectors (BC-501A) as shown in Fig. 1. During the measurements, the intensity of the incident gamma rays was monitored with a large-volume NaI(Tl) detector (8inch-phi x 12inch-long). For each energy setting, the energy profile of the incident gamma rays was measured with a LaBr3(Ce) detector, which was installed in front of the target before each (γ, n) measurement.

Result & Discussion

Particle identification was performed by pulse shape discrimination (PSD) and TOF techniques. Figure 2 shows the two-dimensional (2D) spectrum of tail component versus total charge of analogue signals from one of the LS detectors. A clear separation of neutron and gamma rays

can be seen by the PSD method. In the case of low energy reaction near threshold, the PSD is not good at separation. Thus, we used the TOF method. During the experiment, however, it was found that the single-bunch mode did not work well, and another small bunch was accidentally contaminated close to the true bunch. Figure 3 is the monitor of the electron bunch condition. A fake bunch comes 20 ns after a true bunch, which causes a fake gamma ray events. Figure 4 shows the 2D plot of tail-to-total charge ratio versus TOF spectrum at $E\gamma$ = 15.3 MeV. TOF of fake gamma ray events overlaps with the low-energy neutron events. As a result, the S/N ratio of the (γ, n) measurements at low-energy gamma ray beam settings near neutron threshold became bad. By using the PSD and TOF methods, we deduced the yields of the ^{64}Ni(γ, n) reaction events. The averaged beam intensity during each measurement was obtained from an analysis of a multi-photon spectrum of NaI(Tl) with Poisson-fitting method [2]. The efficiencies of the liquid scintillators were determined by ^{252}Cf fission neutron source and the simulation results of the SCINFUL-CG code [3]. Finally, total cross sections of ^{64}Ni(g, n) reaction were obtained as shown in Fig 5. The obtained data is compared with data taken from Ref. [4]. The absolute values are different, but the behaviour of the excitation energy seems to be simillar with each other. Detailed analysis is still in progress, and we will compare our data with mean-field calculations.

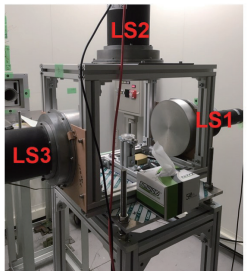

Fig. 1 Photo of the experimental setup. Three liquid scintillator are located at 90 degrees from the beam line. The flight length is 20 cm from the nickel isotope target.

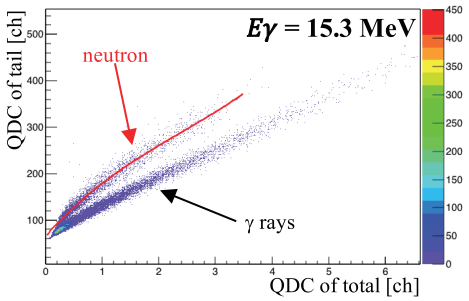

Fig. 2 2D plot of the tail component and the total charge of the analogue signals from (γ, n) raction at $E\gamma$ = 15.3 MeV.

Fig.3 The monitor of stored electrons in the storage ring.

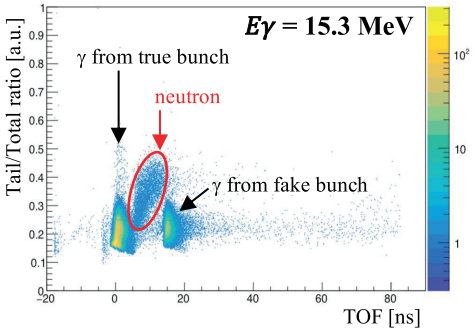

Fig. 4 2D plot of tail-to-total charge ratio vs. TOF.

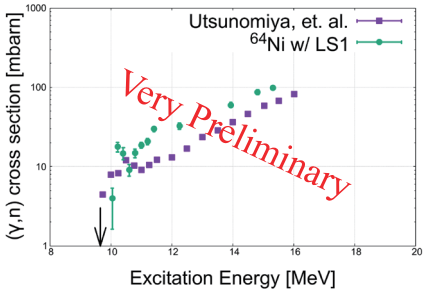

Fig. 5 Obtained cross sections of (g, n) reaction (green dot) and data from Ref. [3] are shown.

References

[1] T. Inakura and H. Nkada, Phys. Rev. C92, 064302 (2015), T. Inakura, et al., Phys. Rev. C84, 021302(R) (2011).

[2] H. Utsunomiya, *et al.*, Nucl. Inst. and Methods in Phys. Res. A 896 103-107 (2018).

[3] Eunjoo KIM, *et al.*,Journal of Nucle. Sci. and Tech., 39, 693-696 (2002).

[4] H. Utsunomiya, *et al.*, Phys. Rev. C98, 054619 (2018).

Development and performance verification of a 3-D position-sensitive Compton camera for imaging MeV gamma rays

H. Hosokoshi[1], J. Kataoka[1], S. Miyamoto[2]
[1] Graduate School of Advanced Science and Engineering, Waseda University, [2] LASTI, University of Hyogo, Laboratory of Advanced Science and Technology for Industry

Abstract

In gamma-ray astronomy, the 1-10 MeV range is one of the most challenging energy bands to observe owing to low photon signals and a considerable amount of background contamination. This energy band, however, comprises a substantial number of nuclear gamma-ray lines that may hold the key to understanding the nucleosynthesis at the core of stars, spatial distribution of cosmic rays, and interstellar medium. Although several studies have attempted to improve observation of this energy window, development of a detector for astronomy has not progressed since NASA launched the Compton Gamma Ray Observatory (CGRO) in 1991. In this work, we first developed a prototype 3-D position-sensitive Compton camera (3D-PSCC), and then conducted a performance verification at NewSUBARU, Hyogo in Japan. To mimic the situation of astronomical observation, we used a MeV gamma-ray beam produced by laser inverse Compton scattering. As a result, we obtained sharp peak images of incident gamma rays irradiating from incident angles of 0° and 20°. The angular resolution of the prototype 3D-PSCC was measured by the Angular Resolution Measure and estimated to be $3.4^\circ \pm 0.1^\circ$(full width at half maximum (FWHM)) at 1.7 MeV and $4.0^\circ \pm 0.5^\circ$ (FWHM) at 3.9 MeV.

Introduction

Technologies for imaging gamma rays in astronomy have been developed in both high and low energy range. For example, Imager On-Board the INTEGRAL (International Gamma Ray Astrophysics Laboratory) Satellite (IBIS), launched in 2002, demonstrates good sensitivity to soft gamma rays up to sub-MeV using a coded aperture mask[1]. Moreover, large area telescopes aboard the Fermi Gamma-ray Space Telescope were launched in 2008 for imaging high energy gamma rays between 100 MeV and 300 GeV[2]. The angular resolution was ~5° at 100 MeV and 0.8° at 1 GeV, which led to the discovery of several unidentified sources[3]. In the middle of these energy bands, however, 1-10 MeV gamma rays can easily penetrate a collimator similar to a coded aperture mask. Therefore, it is impossible to acquire images using photo-absorption within the detector. In addition, pair-production does not occur adequately, and therefore, it is difficult to obtain a back projection image using tracking detectors, such as silicon strip detectors. A Compton camera is commonly used for identifying the direction of MeV gamma-ray sources based on Compton kinematics. However, the sensitivity of the MeV energy range is currently low by a few orders compared to other energy range values. Compton Telescope (COMPTEL), which was a huge Compton camera loaded on CGRO, demonstrated the highest sensitivity in the 1-10 MeV range[4]. CGRO-COMPTEL succeeded in producing a 1-30 MeV image of the entire sky for the first time; however, only 32 gamma-ray sources have been detected.

Establishing a method to image 1-10 MeV gamma rays has been much anticipated, because there is a substantial number of nuclear gamma-ray lines in this narrow range. These lines may hold the key to understand the nucleosynthesis process that happens at the core of stars or the spatial distribution of cosmic ray and interstellar medium. Some lines, such as 1.807 MeV from ^{26}Al and 1.156 MeV from ^{44}Ti were detected by CGRO and INTEGRAL; however, the nuclear deexcitation lines have not been detected so far.

For future astronomical observation, we demonstrated that the proposed Compton camera can provide a high quality image in the MeV energy range. To verify the performance of this camera, we irradiated 17 positions of it with MeV gamma-ray beam to mimic signals from celestial gamma-ray sources. Then, a clearly separated image of gamma rays from each incident angle, 0° and 20°, was obtained in the experiment.

Experiments

The 3D-PSCC was originally developed for imaging MeV gamma rays in proton therapy[5]. The target energy band of the 3D-PSCC is from 300 keV to 5 MeV. A schematic view of the 3D-PSCC is shown in Figure 1. Two scatterers comprising $42 \times 42 \times 1$ arrays of $0.5 \times 0.5 \times 3.0\,\mathrm{mm}^3$ cubes were placed apart from each other by 11 mm. In contrast, $22 \times 22 \times 10$ arrays of $2.0 \times 2.0 \times 4.0\,\mathrm{mm}^3$ cubes were used as an absorber. Each pixel was divided by a reflector ($BaSO_4$ with thickness of about 0.1 mm) in the XY direction defined in Fig. 1(a). The absorber's pixels aligned along the Z direction were also divided by a thin layer of air, enabling easier measurement of the depth of interaction (DOI)[6]. Moreover, a bismuth germanate (BGO) active shield was placed behind the absorber, while tungsten passive shields were placed in front of the scatterer and absorber, as shown in Fig. 1(b).

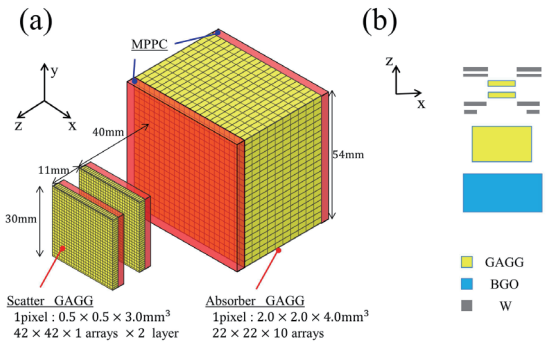

Figure 1. Schematic view of the 3D-PSCC

NewSUBARU is a synchrotron radiation facility located in the site of Spring8, Hyogo in Japan. High-energy electrons from Spring8 are used for various experiments in 11 beam lines. Our experiment was conducted in BL01, which treats a quasi-monochromatic MeV gamma-ray beam. The gamma rays are produced by inverse Compton scattering of a CO_2 laser ($\lambda = 10.6\,\mu$m) with 1 or 1.5 GeV electrons. Here, the upper limits of incident energy were estimated at 1.7 MeV and 3.9 MeV. These gamma rays pass through a thick Pb collimator to form a quasi-monochromatic gamma-ray beam. To simulate the situation of an astronomical observation, we used the MeV gamma-ray beam assuming signals from celestial gamma-ray sources. Considering the symmetry of the camera, irradiating points of 1.7 MeV beams (shown in Figure 2(a)) are selected to cover 17 positions (shown in Fig.2(b)) so that the 3D-PSCC is exposed to gamma rays as uniformly as possible. Eight out of these 17 positions are assuming background events that enter the absorber directly. By contrast, only the center of the 3D-PSCC was irradiated with the 3.9 MeV gamma-ray beam due to time restrictions of the experiment. A geometry of the experiment is shown in Fig. 2(c). A 5 cm thick Pb block was placed in front of an irradiating port considering the rate tolerance of the 3D-PSCC. The measurement times for 1.7 MeV and 3.9 MeV were 5 min and 30 min respectively.

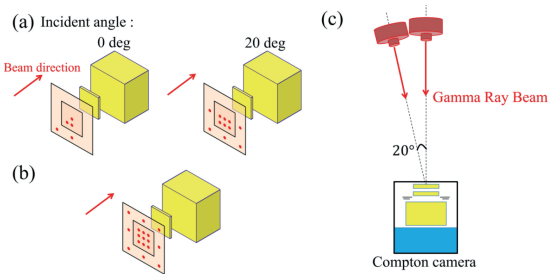

Figure 2. (a) Positions irradiated with a 1.7 MeV gamma-ray beam for each incident angle, represented as red points. (b) All 17 positions covered considering the symmetry of the camera. (c) Experimental setup for imaging MeV gamma-ray beams.

Figure 3 shows images of the 1.7 MeV (upper) and 3.9 MeV (lower) gamma-ray beam with an incident angle of 0° (left) and 20° (right). The energy window was 1.4-1.9 MeV for 1.7 MeV imaging, and 3.0-4.2 MeV for 3.9 MeV. Both 1.7 MeV and 3.9 MeV images appeared concentrated around the position corresponding to each incident angle. Specifically, the peak locations derived from 1-D projection along the X-axis were $1.7^\circ \pm 1.1^\circ$ and $19.6^\circ \pm 1.4^\circ$ for each 1.7 MeV image, and $1.4^\circ \pm 2.4^\circ$ and $17.4^\circ \pm 2.1^\circ$ for each 3.9 MeV image.

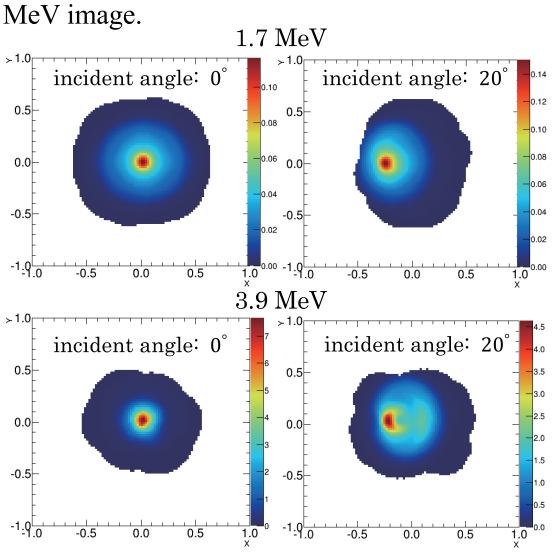

Figure 3. Images of the gamma-ray beam

To evaluate the angular resolution of the 3D-PSCC, we used Angular Resolution Measure (ARM), which represents the difference between the geometrical scatter angle and the scatter angle calculated using energy deposit. The ARM spectra are displayed in Fig. 4. An experimental value of the ARM spectra was fitted by Gaussian to evaluate angular resolution. The angular resolution at 1.7 MeV was estimated as $3.4^\circ \pm 0.1^\circ$ (FWHM) and $3.8^\circ \pm 0.1^\circ$ (FWHM) for each incident angle. These experimental values and their dependence on the incident angles agreed well with Geant4 simulation. Note that the angular resolution of COMPTEL aboard CGRO was 3.9° (FWHM) at 1.7 MeV. Moreover, the angular resolution at 3.9 MeV was $4.0^\circ \pm 0.5^\circ$ and $4.6^\circ \pm 0.4^\circ$ for each incident angle, which is again consistent with the simulation.

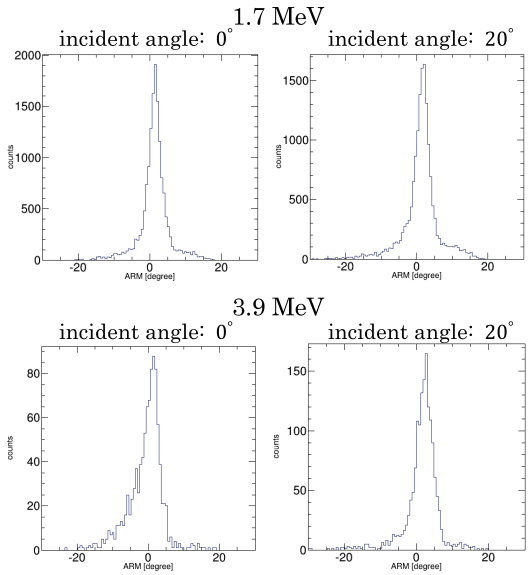

Figure 4. ARM spectra for each condition

In actual astronomical observation, we need to image gamma rays with different incident angles corresponding to different sources in the FoV. To mimic such a situation, we superposed an image of 1.7 MeV gamma-ray beams with incident angles of 0° and 20°. Flux and measurement time are the same for both 0° and 20°. The intensities of the two sources, however, will not be identical without correction because a Compton camera shows a different response to each source within the FoV. Therefore, we inspected the response of the 3D-PSCC to the sources which were distributed uniformly on a hemispheric surface using Geant4 simulation beforehand. The generated *sensitivity maps* were used to correct the intensity of gamma-ray sources within the FoV. Figure 5 (left) shows a simple back-projection image of two gamma-ray beams. The good angular resolution of the 3D-PSCC at 1.7 MeV enables the images of the two sources to be clearly separated. The maximum likelihood-expectation maximization (ML-EM) analysis was also performed, as shown in Figure 5 (right). Further, the intensities of the two gamma-ray beams from 0° and 20° were nearly the same, as expected. This means the sensitivity map correctly anticipated the response of the 3D-PSCC to the sources at 0° and 20°.

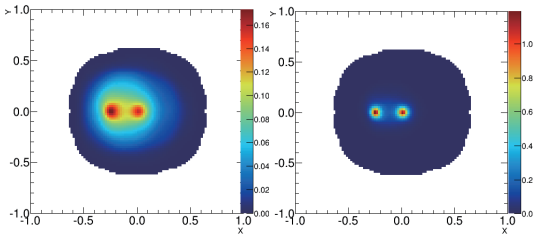

Figure 5. Images of 1.7 MeV gamma-ray beam irradiating from 0° and 20° off the axis of the camera.

The results of the experiment are validated by Geant4 simulation. Figure 6 shows the simulated angular resolution of the 3D-PSCC at various incident energies, compared with the experimental value. The energy window for the simulation was $0.9E_i<E<1.1E_i$, where E_i denotes the incident energy of gamma rays. The angular resolution of a Compton camera is affected by energy resolution, position resolution and the Doppler broadening effect. In this case, the energy resolution dominates the angular resolution below 1 MeV. However, position resolution, which is determined by the pixel size of the scatterer and absorber, dominates the angular resolution above 1 MeV. The Doppler broadening effect is caused by a momentum distribution of bound atomic electrons, but its influence on the angular resolution is negligible in the MeV-energy range.

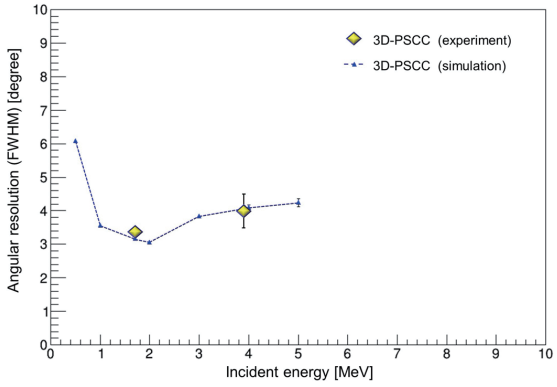

Figure 6. Comparison of the angular resolution simulated using Geant4 and the experimental value.

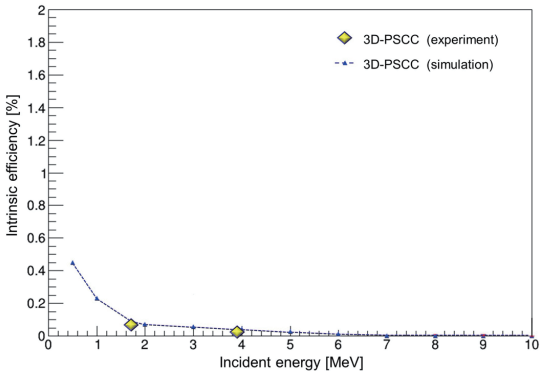

Figure 7. The simulated intrinsic efficiency and the experimental value.

The results in the experiment (yellow plots) agreed well with the Geant4 simulation (blue). Both the experiment and the simulation confirmed that the 3D-PSCC has better angular resolution than COMPTEL in the energy range below 2 MeV, despite its compact structure. However, the angular resolution of the 3D-PSCC decreases in the range above 3 MeV. In the high-energy range, energy uncertainty caused by the increased escape events dominates the angular resolution. As gamma rays above 3 MeV are considerably more energetic and cannot be easily stopped with the current configuration of 3D-PSCC, we applied a broad energy window to increase the number of proper events for imaging. The broad energy window also contains a substantial number of escape events where only a part of the incident energy was deposited within the detector. The discrepancy between the incident energy and the observed one caused degradation of the angular resolution, which led to the results in the energy range above 3 MeV.

References

[1] Ubertini, P. *et al*., Astronomy&Astrophysics, **411**, L131-L139 (2003).
[2] W. B. Atwood. *et al.*, The Astrophysical Journal, **697**, 1071-1102, (2009).
[3] Acero, F. *et al.*, The Astrophysical Journal Supplement Series, **218**, 23-64, (2015).
[4] Schönfelder, V. *et al*., The Astrophysical Journal Supplement Series, **86**, 657-692, (1993).
[5] S. Mochizuki. *et al*., Nucl Instruments Methods Phys Res Sect A in press, (2018).
[6] A. Kishimoto. *et al*., IEEE Transactions on Nuclear Science, **60**, 38-43, (2013).

Measurement of Neutron Energy and Angular Distribution From Tens of MeV Polarized Photons on Medium-Heavy Targets

Tran KimTuyet[1], Toshiya Sanami[1,2*], Hirohito Yamazaki[1,2], Toshiro Itoga[3], Yoichi Kirihara[4], Yasuhito Sakaki[1,2], Akihiro Takeuchi[1], Shuji Miyamoto[5], Hiroshi Nakashima[6] and Yoshihiro Asano[2,5]

[1]SOKENDAI, [2]KEK, [3]JASRI, [4]Japan atomic energy agency,
[5]LASTI, University of Hyogo, [6] Hokkaido University

Abstract

Experiments have been performed to measure neutron energy and angular distribution from photo-nuclear reactions for tens of MeV mono-energetic polarized photons on medium-heavy nuclei at NewSUBARU BL01 facility. An overview of the experiment and an example of the results for the target mass and incident photon energy dependence of the neutron energy spectrum are presented.

Introduction

Neutrons from photonuclear reactions play an important role in the shielding design of high-energy electron accelerators, which are widely used in physics, medical, and industrial applications [1]. The accelerated electrons interact with the targets or other materials, generating energetic photons that cause photonuclear reactions. The photonuclear reactions generate secondary hadrons, including neutrons. The neutrons can penetrate thick shielding walls and induce activation in air, water, and materials surrounding the accelerator. Thus, the reduction of neutron flux is important for the shielding design.

To design accelerator shielding, secondary particle generation and transport from the energetic electron beam were computed using radiation transport code including a photonuclear reaction model. Several such models have been established for decades, and tested by comparison with experimental data. Most of the data have been taken for unpolarized photon beams with broad energy width [2][3]. The data provide cumulative yield and spectra for neutron production for incident photon energy. Less experimental data are available for the polarization dependency of neutron production and energy distribution.

Recently, a new fully polarized photon source with a narrow energy width has been developed using the laser Compton back scattering (LCS) technique at NewSUBARU's BL01 facility [4][5]. This photon source is suitable for studies of photonuclear reactions. Because the beamline provides a photon beam with variable energy and polarization, the facility is the only one in the world that can provide this type of detailed photoneutron production data.

For this reason, we have been conducting an experimental study of photoneutron production at this beamline since 2015. By using this facility, we successfully obtained the photoneutron energy spectrum and angular dependence for a gold target under a 16.6 MeV polarized photon [6]. As a next step of this study, we apply this methodology to obtain data for other medium-heavy targets, in order to provide systematic data for reaction model evaluation. By using thinner targets, we intended to obtain photon-induced neutron emission reaction, (γ,xn), data as a function of energy and angle, normalized with the number of target atoms and incident photons – i.e, double differential cross section (DDX). This series of experiments was performed in 2019 and 2020. In this paper, we present

* Corresponding author: Email toshiya.sanami@kek.jp

an overview of the experiments, along with part of the results.

Experiments

The experimental procedure and data analysis for this experiment were almost the same as in the previous one [6], except for the target composition and thickness, incident photon energy, and number of detectors. Thus, these items are discussed in this section after explaining the beamline layout and experimental setup are explained.

Figure 1 displays the beamline layout and experimental setup at BL01, a facility at NewSUBARU. The LCS photon beam was prepared by a 20 W NdYAG laser, a single-bunch electron beam circulating in the storage ring, and two collimators (C1 and C2 in the storage ring enclosure and Hutch 1, respectively). After collimation, the LCS beam was sent to Hutch 2, named GACKO, which contained neutron detectors and a target for (γ,xn) reactions.

The chosen target materials were Pb, Au, Sn, Cu, Fe, and Ti. Gold was selected to confirm the consistency of these experimental results with the previous data [6]. Lead, copper, and iron are materials used frequently in shielding electron accelerators. Sn was chosen for its mass number, between those of Au and Cu. Ti was also used in the accelerator, and was chosen for having a mass number less than that of Fe. Another reason tin and titanium were chosen is because they have relatively few isotopes. Aluminum and carbon were not used in this experiment, because their low densities make them low-yield. They will be studied in the future.

The target thicknesses were chosen to obtain sufficient statistics within a reasonable time and reduce photon attenuation as much as possible. The photon attenuations for each material were obtained as the ratio of the average track length of the incident photon to the total length of the target. The average track length was calculated using a Monte-Carlo simulation code called PHITS. Table 1 summarizes the target material, thicknesses, and photon attenuation for 17 MeV incident photons.

Table 2 lists the combination of targets and incident photon energies in this experiment. 17 MeV was the standard energy because it was obtained under top-up operation of the NewSUBARU storage ring, which gives maximum beam intensity. The other energies were obtained from the storage ring's decay mode. In the 2019 experiment, we took data for 17 MeV photons to assess target mass dependence at this energy. In the 2020 experiment, we took data for 13, 20, and 23 MeV photons to assess energy dependence. Note that the energies are nominal. For precise values, the actual setup of collimators must be considered. For example, the nominal 17 MeV energy yields a 16.95 MeV maximum and 16.6 MeV average energy after evaluation through Monte-Carlo simulation.

Table 1: List of targets for experiment

Material	Length	Attenuation
Pb	1 cm	0.73
Au	1 cm	0.60
Sn	2 cm	0.69
Cu	2 cm	0.75
Fe	2 cm	0.80
Ti	4 cm	0.78

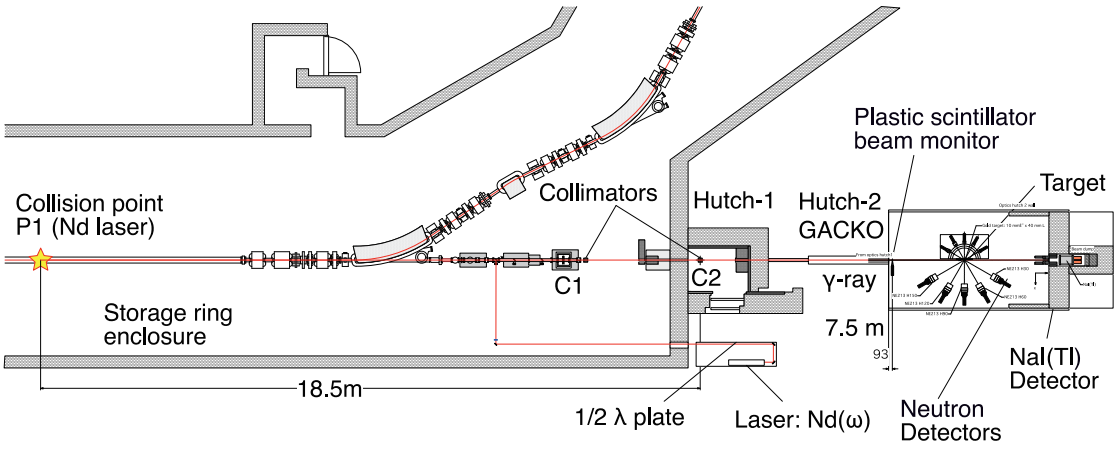

Figure 1: Layout of the beam line and experimental setup

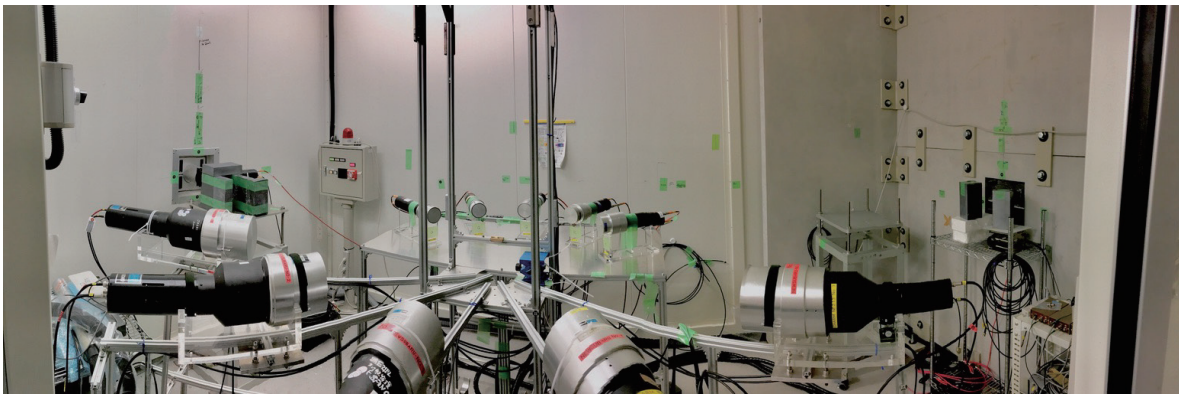

Figure 2: Panorama view of experimental setup

Table 2: List of energy and target combination.

Photon energy	Targets
13 MeV	Au
17 MeV	Pb, Au, Sn, Cu, Fe, Ti
20 MeV	Au, Cu, Ti
23 MeV	Cu, Ti

Figure 2 shows a panorama view of the experimental setup in Hutch 2. LCS photons came from the left-hand side of this figure. The photons went through a plastic scintillator placed at Hutch 2's entrance to monitor beam intensity, then hit the target placed at the center of this setup. Part of the photon beam induces photonuclear reactions; and the remaining part reaches the opposite side of the Hutch 2 wall. The neutrons were measured using organic liquid scintillators placed several tens of centimeters from the target, permitting use of time-of-flight technique.

In the 2019 experiment, five neutron detectors were placed on the right-hand side from the photon direction at 30°, 60°, 90°, 120°, and 150°, to determine the angular dependence of neutron emission. In addition, one more neutron detector was placed just above the target. The polarization direction of the photons was set parallel to the floor to enhance the effect of polarization. All neutron detectors were cylindrical, of 12.5 cm in diameter, and 12.5 cm long.

In the 2020 experiment, we also employed five small neutron detectors, 5 cm in diameter and 5 cm long, on the left-hand side from the photon direction. These measured low energy neutrons to help determine the total neutron yield.

The DDXs, $d^2\sigma/dEd\Omega$, were obtained from the following equation:

$$\frac{d^2\sigma}{dEd\Omega}(E) = \frac{Y(E)/\eta(E)}{Nl(\tau\phi)\varepsilon(E)\Delta E\Delta\Omega}$$

where $Y(E)$ is the neutron energy spectrum obtained by time-of-flight spectrum, $\eta(E)$ is the neutron attenuation factor due to scattering in the target, N [#/cm^3] is the number of atoms in the target, l [cm] is the target thickness, τ is the photon attenuation factor listed in Table 1, ϕ [#/cm^2] is the LCS photon flux neutron yield, $\varepsilon(E)$ is the detection efficiency of the neutron detector, ΔE [MeV] is the energy bin width of the neutron energy spectrum, and $\Delta\Omega$ [sr] is the solid angle subtended by the neutron detector. $\eta(E)$ and τ were obtained by neutron and photon transport calculations using the PHITS code [7]. ϕ was determined from counts of the plastic scintillator, with counting efficiency determined by simulation using the EGS5 code [8]. $\varepsilon(E)$ was obtained experimentally using a ^{252}Cf fission neutron source and SCINFUL-QMD code [9][10]. A more detailed procedure for data analysis and uncertainty evaluation can be found in the references [6] [10] [11].

Results and Discussion

These experimental data were used to examine the photonuclear reaction. These results are summarized in papers under preparation as of this writing. As examples of the data, two topics we presented in the Atomic Energy Society meeting [12][13] are presented in this section.

Figure 3 shows the DDXs of the Pb, Au, Cu, Fe and Ti (γ,xn) at 90 degrees for 17 MeV horizontally polarized photons. We can observe two components of the neutron spectra, as pointed out in ref [6], not only for gold targets but for the other targets. Below 4 MeV, the evaporation component is dominant. The slope of the evaporation component depends on target mass. The evaporation component increases with increasing target mass number. Above 4 MeV,

non-evaporation component, that is direct component mentioned in ref [6], is observed for all targets. The magnitude of this component increased with increasing target mass. These features will be parameterized in an upcoming paper.

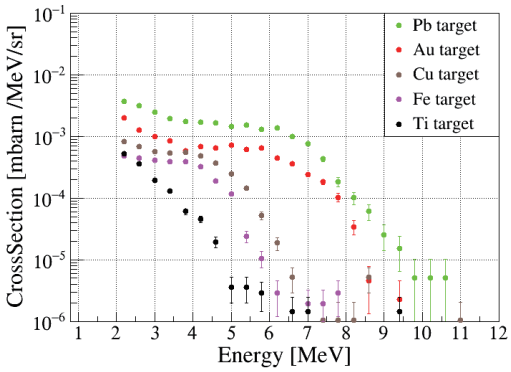

Figure 3: DDX of the Pb, Au, Cu, Fe and Ti (γ,xn) at 90 degrees for 17 MeV horizontally polarized photons

Figure 4 shows DDXs of the ^{197}Au(γ,xn) at 30 to 150 degrees for 13 and 17 MeV. From this result, the slope of the evaporation component looks independent of incident photon energy. Only the non-evaporation component decreases with decreasing incident photon energy. Thus, the ratio of non-evaporation to evaporation neutrons depends on incident photon energy. More information is expected from the data for 20 and 23 MeV incident photon energy, which we are processing and reviewing as of this writing.

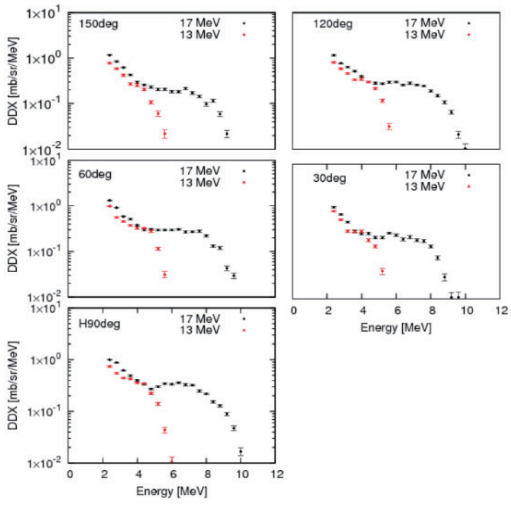

Figure 4: DDXs of ^{197}Au(γ,xn) at 30 to 150 degrees for 13 and 17 MeV

Conclusion

Experiments were performed to measure the neutron energy spectrum as a function of photon energy, target atom, and solid angle, at several angles. Double differential cross sections were found for photonuclear reactions on tens of MeV mono-energetic polarized photons on Pb, Au, Sn, Cu, Fe, and Ti targets. An overview of the experimental procedure and examples of results are presented. The results of this experiment will be summarized as an original scientific paper.

References

[1] W.P.Swanson, "Radiological safety aspects of the operation of electron linear accelerators", IAEA Technical reports series No.188, IAEA, Vienna 1979, ISBN 92-0-125179-3.

[2] A.V.Varlamov, V.V Varlamov, D.S. Rudenko, Atlas of giant dipole resonances. Parameters and graphs of photonuclear reaction cross section. IAEA Tech Rep. INDC(NDS)-394. IAEA; 1999.

[3] A.I. Blokhin, M.B. Chadwick, T. Fukahori, et al., Handbook on photonuclear data for applications: cross sections and spectra. Vienna: IAEA; 2000.

[4] S.Miyamoto, Y.Asano, S.Amano et al., *Radiat. Meas.* (2007), 179-185.

[5] Y.Asano, S.Miyamoto. *Prog. Nucl. Sci. Tech.* (2014) , 252-256.

[6] Y. Kirihara et al., *J. Nucl. Sci. Tech.* (2019) , 444-456

[7] T. Sato et al, *J. Nucl. Sci. Tech.* 2013,50,913-923.

[8] H. Hirayama et al., The EGS5 code system, SLAC-R-730 and KEK-REPORT-2005-8.

[9] D. Satoh, et al. , *J. Nucl Sci Tech.* (2002), 657-660.

[10] T.K.Tuyet et al., *"Experimental approach to determine detection efficiency of organic liquid scintillators with different volumes",* Proc. 2020 Symp. on Radiation detectors and their uses., *15-17, Jan 2020, KEK, Tsukuba, Japan* (*to be published*).

[11] T.K.Tuyet et al., *"Comparison between experimental and calculation neutron spectra of the ^{197}Au(γ,sn) reaction for 17 MeV polarized photon"*, Proc. Nuclear Data Symposium 2019, 28-30 Nov. 2019, Kyushu University, Japan (*to be published*).

[12] T. K. Tuyet et al., Presentation of 2M02, AESJ 2019 autumn at Toyama University Sep 11-13

[13] T. K. Tuyet et al., Presentation of 2O06, AESJ 2020 spring at Fukushima University Mar. 16-18

Nuclear resonance fluorescence measurements for nuclear security

Toshiyuki Shizuma[1], M. Omer[2], R. Hajima[2], M. Koizumi[2], T. Takahashi[2], S. Miyamoto[3], and S. Amano[3]
[1]National Institutes for Quantum and Radiological Science and Technology, [2]Japan Atomic Energy Agency,
[3]LASTI, University of Hyogo

Abstract

Non-destructive detection based on nuclear resonance fluorescence (NRF) was demonstrated by using a quasi-monoenergetic γ-ray beam produced by laser Compton scattering (LCS) at the NewSUBARU synchrotron radiation facility. The LCS γ-ray beam with the maximum energy of 7.4 MeV was used to bombard a ^{208}Pb target which was enclosed in a thick iron box. NRF γ rays at 7.332 MeV emitted from the target were observed for the detection of the ^{208}Pb material. The counting rate is comparable with a result from the previous simulation study for non-destructive detection of ^{235}U hidden in a 5-mm-thick iron container.

Introduction

The non-destructive detection of nuclear materials is crucial for nuclear security [1], nuclear waste management [2], and non-proliferation of nuclear materials [3]. Nuclear resonance fluorescence (NRF) may be only method that can be used to perform quantitative assay of such shielded materials. NRF is a fundamental process where a discrete nuclear state resonantly absorbs a γ ray, and then decays by γ-ray emission, either to the ground states or an excited state [4]. The γ-ray energy for absorption is precisely determined from the level energy. Because the level energy varies for each nuclide, the NRF assay that detects characteristic γ rays can provide isotope-specific signatures.

At the NewSUBARU synchrotron radiation facility [5,6], we developed measurement technology for demonstration experiments on non-destructive detection of ^{208}Pb which was a simulant of nuclear materials. We first installed a 2-micron laser system and generated quasi-monoenergetic γ rays produced by laser Compton scattering (LCS). By using the LCS γ-ray beam, we carried out a demonstration experiment for non-destructive detection of a simulant material of ^{208}Pb enclosed in a thick iron box.

Experiments and Results

A quasi-monoenergetic, linearly polarized γ-ray beam was generated in backward Compton scattering of laser light with high energy electrons circulated in the NewSUBARU electron storage ring. A Q-switch Tm laser with a wavelength of 1993 nm operated at a frequency of 25 kHz was used for the incident laser photons. The electron energy was chosen to be 885 MeV to generate a quasi-monoenergetic γ-ray beam with the maximum energy of 7.4 MeV which is above the strong NRF transition at 7.332 MeV in ^{208}Pb [7]. A 10 cm thick Pb collimator with a 4-mm aperture was used to produce a γ-ray beam with $\Delta E/E \cong 5\%$. The average γ-ray flux was 1.2x10^5 photons/s which was measured by an 8”x10” NaI(Tl) scintillation detector. The target was 10-g ^{208}Pb enriched to 98% with a diameter of 8 mm. Two high-purity Ge detectors with an efficiency of 140% relative to a 3”x3” NaI scintillation detector were used to measure NRF γ rays from the target. The Ge detectors were placed horizontally at a scattering angle of 90°. The energy distribution of the incident photon beam was measured by one of the Ge detectors. A Monte Carlo simulation code EGS-5 [8] was used to analyze the response of the Ge detector for extraction of the energy distribution of the incident photon beam [9]. The energy distribution of the incident photon beam is shown in Fig. 1.

Figure 2 shows a photograph of the experimental setup. The ^{208}Pb target was placed at the center of an iron plate which could be moved by the automatic stage. We enclosed the ^{208}Pb target inside the iron box. The target was irradiated with the LCS γ-ray beam from outside the iron box. The horizontal position of the iron box was changed by 2mm step. We measured NRF γ rays at 9 different positions from x=-8 to +8 mm. Here, x is the difference between the center of the LCS γ-ray beam and the ^{208}Pb target. Figure 3(a) shows a γ-ray spectrum at x=0 where the LCS γ-ray beam hit the center of the target. The NRF peak of ^{208}Pb at 7.332 MeV is clearly observed. In contract, Fig. 3(b) shows an energy spectrum at x=+8 mm where the LCS γ-ray beam is off the target. No NRF peak associated with ^{208}Pb is observed. The NRF peaks of ^{208}Pb,

shielded inside the iron container, are observed, when the LCS γ-ray beam hit the ^{208}Pb target. The ^{208}Pb material can be detected by the present technique based on NRF, although it is contained in the 1-3 cm-thick iron box.

The counting rate for the detection of the 7.332 MeV NRF peak is 0.035 cps in the present measurement. Using a typical level width for actinides, the expected flux of the LCS γ-ray beam [2], and the more realistic distance between the target and Ge detectors, the counting rate is estimated as 18 cps. This value is consistent with a result from the previous simulation study showing the capability of non-destructive detection of 1-kg ^{235}U hidden in a 5 mm-thick iron container [10].

This work was a part of the study of NRF phenomenon aiming at nuclear security and safeguards applications, being supported by the sabsidy for "promotion of strengthening nuclear security or the like" of the Ministry of Education, Culture, Sports, Science, and Technology (MEXT), Japan.

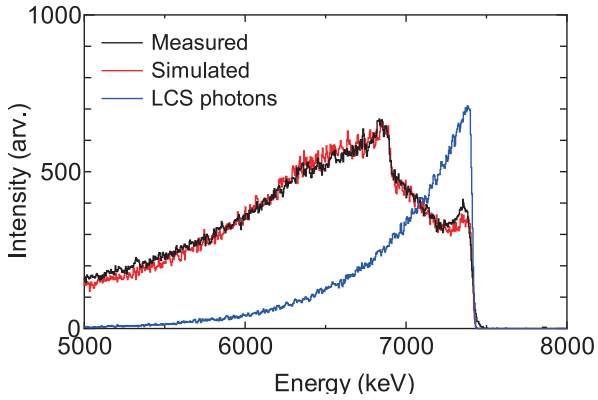

Figure 1 Energy distribution of the incident LCS γ-ray beam measured using the HP-Ge detector (black line). The original photon spectrum, shown by the blue line, was obtained by unfolding the simulated energy distribution (red line).

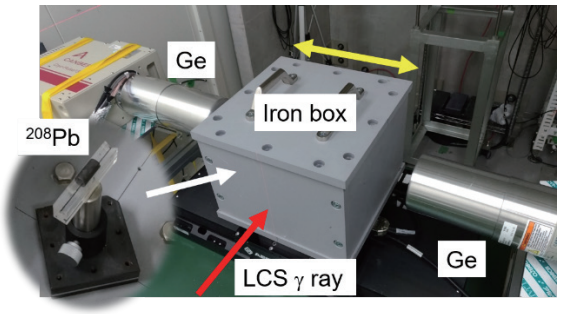

Figure 2 Experimental setup. The ^{208}Pb target is irradiated with the LCS γ-ray beam from outside the iron box. Emitted NRF γ rays are detected by two HP-Ge detectors. The iron box can be moved horizontally by the automatic stage.

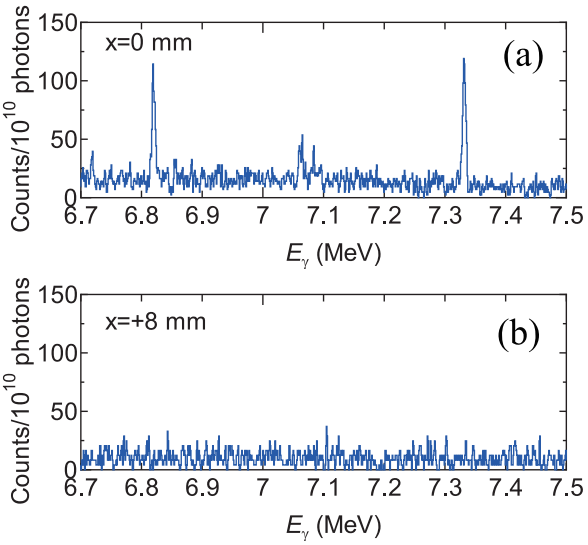

Figure 3 γ-ray spectra at x=0 where the LCS γ-ray beam hit the center of the target (a) and at x=+8 mm where the LCS γ-ray beam is off the target (b).

References

[1] W. Bertozzi et al., Nucl. Instrum. and Methods Phys. Res. Sect. B 241, 820 (2005).
[2] R. Hajima et al., J. of Nucl. Sci. Tech. 45, 441 (2008).
[3] B.J. Quiter et al., Nucl. Instrum. and Methods Phys. Res. Sect. B 269, 1130 (2011).
[4] U. Kneissl et al., Prog. Part. Nucl. Phys. 37, 349 (1996).
[5] S. Miyamoto et al., Radiat. Meas. 41, S179 (2006)
[6] S. Amano et al., Nucl. Instrum. Methods Phys. Res. Sect. A 602, 337 (2009).
[7] T. Shizuma et al., Phys. Rev. C 78, 061303(R) (2008).
[8] H. Hirayama et al., The EGS5 code systems, SLAC Report 730 (2010).
[9] T. Shizuma et al., Phys. Rev. C 96, 044316 (2017).
[10] H.H. Negm et al., Proceedings of the IEEE (HST) International Symposium (2015).

Local structure analysis of Si-containing DLC films

Kazuhiro Kanda[1], and Takayuki Hasegawa[1,2]
[1] LASTI, University of Hyogo, [2] Synchrotron Analysis LLC

Abstract

Structural analysis by the measurement of silicon K-edge near-edge x-ray absorption fine structure (NEXAFS) using synchrotron radiation was performed on 12 kinds of silicon-containing diamond-like carbon (Si-DLC) films fabricated with various synthesis methods. It was found that the position of the absorption edge and spectral profile in Si K-edge NEXAFS is mostly not influenced by ratio of Si/C, unlike the C K-edge NEXAFS. In other words, Si atoms are incorporated in the carbon network in Si-DLC film in the range of Si/C ratio in the present work.

Introduction

Many working groups were reported the several properties of DLC films were improved by doping a hetero element in last decade. Especially, Si-doped DLC films have been widely investigated because it is expected improve sliding properties, burning resistance, and oxidation resistance. The near-edge X–ray absorption fine structure (NEXAFS) spectroscopy using synchrotron radiation is known to be sensitive to the local structure around the absorber carbon atom and we have reported structural analysis by the measurement of carbon K-edge NEXAFS of silicon-containing diamond-like carbon (Si-DLC) films in previous work[1]. In the present study, local structures of 12 kinds of Si-DLC films were studied using Si K-edge NEXAFS spectroscopy.

Materials and Methods

In the present study, the 12 kinds of Si-DLC films, which were provided by enterprises, public organizations and universities, analyzed by the measurement of Si K-edge NEXAFS. These samples were collected in the international round robin test in 2009 by international standard development of METI. These DLC samples were synthesized by the various methods, which contained physical vapor deposition (PVD) and chemical vapor deposition (CVD). Si-DLC films were deposited on the Si substrate with film thickness of 200 nm. The elementary analysis of sample Si-DLC film was performed by using the combination of Rutherford backscattering spectrometry (RBS) and elastic recoil detection analysis (ERDA). The ratio of Si/C in Si-DLC film ranged of 0.03 ~0.64.

The Si K-edge NEXAFS spectra were measured at BL05A. In BL05A, synchrotron radiation provided from bending magnet was dispersed by a double crystal monochromator (DXM)[2]. The Si K-edge NEXAFS spectra were measured in the energy range of 1830–1880 eV using InSb(111) as a dispersive crystal. Monochromatized synchrotron radiation was irradiated on the sample film at 54.7° (magic angle) with respect to the surface normal of the samples. The detection of electrons coming from the sample was performed in the total electron yield (TEY) mode. The intensity of the incident photon beams, I0, was measured by monitoring the photocurrent from a gold film. The absorption signal was given by the ratio between the out-coming electron intensity from the sample, I_s, and the intensity from the gold film, I_0.

Results and Discussion

Fig. 1 shows Si K-edge NEXAFS spectrum of a Si-DLC film (Sample XX) and several reference materials: Si wafer, a-Si:H film, SiC powder, and SiO_2 powder. Si K-edge NEXAFS spectrum of SiO_2 has intense peak

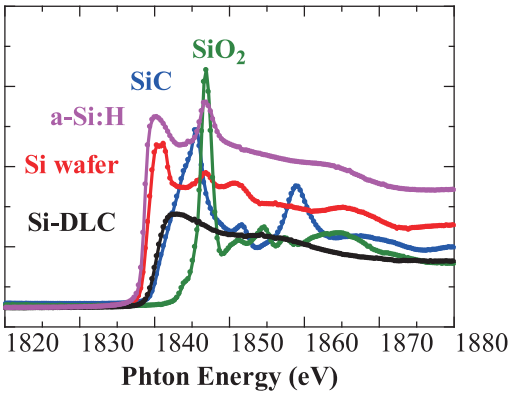

Fig. 1 Si K-edge NEXAFS spectra of Si-DLC and reference materials: Si wafer, a-Si:H chip, SiC powder, and SiO_2 powder .

at 1847 eV. In the spectra of Si wafer and a-Si:H film, the peak is observed at same position. This indicates that Si wafer and a-Si:H film were naturally oxidized.

The Si atoms in Si-DLC films can be expected to couple with Si, C, and H. The chemical environment around the absorbing atom will determine the white line intensity and the position of the absorption edge, E_o, which is usually defined as the first inflection point in the absorption spectrum. As can be seen in Fig. 1, E_o shifts towards higher energy with increasing positive charge on the absorber, and increasing electronegativity of the ligand causes an increase in the white line amplitude. The edge position of Si-DLC film (E_o ~ 1841 eV) is higher than those of Si wafer and a-Si:H film (E_o ~ 1840 eV), and lower than that of SiO_2 powder (E_o ~ 1847 eV). The edge position and the amplitude of the white line in Si-DLC samples are somewhat similar to those of SiC powder. As a result, the chemical environment of Si atoms in Si-DLC films can be regarded to be similar to Si atoms in SiC.

Left side of Fig. 2 shows Si K-edge NEXAFS spectra of the 12 kinds of Si-DLC films. Spectra were displayed in high order of Si/C ratio in samples below from the top. In the Si K-edge spectrum of the seventh sample from the top, the intense peak was observed at 1847 eV. This peak was assigned to oxidized Si as shown in spectrum of SiO_2 of Fig. 1.

Right side of Fig. 2 shows C K-edge NEXAFS spectra of same Si-DLC films reported in ref. 1. Spectral profiles of C K-edge NEXAFS of the Si-DLC films change by ratio of Si/C in film. As increasing Si/C ratio in film, 1) shrinking of the σ^* band was due to the change from σ(C–C) to σ(C–Si) and 2) broadening of the π peak can be considered to be due to increase in the composition ratio of C=C–Si sites. On the other hand, the position of the absorption edge, E_o, and spectral profile in Si K-edge NEXAFS is mostly not influenced by ratio of Si/C and H content in film. This indicate that the energy of C atoms, which couple with only C atoms in DLC film, is shifted largely by the formation of C-Si bonding, but Si atoms in Si-DLC film form only Si-C bonding not Si-Si bonding in the range of Si/C ratio in the present work. In other words, the formation of clusters composed primarily of Si atoms does not occur; instead, Si atoms are incorporated in the carbon network in Si-DLC film.

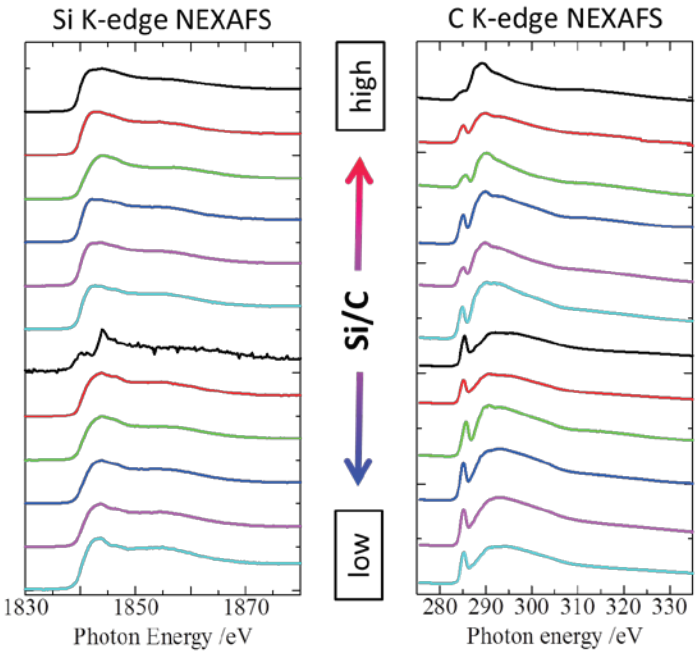

Fig. 2 Si K-edge NEXAFS spectra (left side) and C K-edge NEXAFS spectra (right side) of Si-DLC films in high order of Si/C ratio in samples below from the top.

References

[1] K. Kanda *et al.*, J Jpn. J. Appl. **52** (2013) 095504.
[2] K. Kanda *et al.*, J. Phys.: Conf. Ser. **425** (2013) 132005.

Measurement of Positron Lifetimes of Various Diamond-like Carbon Thin Films

Kazuhiro Kanda[1], Hiroki Akasaka[2], Fuminobu Hori[3], Atsushi Yabuuchi[4], and Atsushi Kinomura[4]
[1] LASTI, University of Hyogo, [2] School of Engineering, Tokyo Institute of Technology,
[3] Graduate School of Engineering, Osaka Prefecture University,
[4] Institute for Integrated Radiation and Nuclear Science, Kyoto University

Abstract

Positron annihilation lifetime spectroscopy system for the measurement of thin films was constructed at were at the slow positron beam system (B-1) at Kyoto University research Reactor (KUR) and measurement of positron annihilation lifetimes of diamond-like carbon thin films with film thickness of several hundred nm were succeeded. Positron annihilation lifetime obtained was found to show good correlation with nano-indentation hardness.

Introduction

Diamond-like carbon (DLC) film, which is amorphous carbon film consisting of carbon and hydrogen, has several excellent properties, such as high mechanical hard-ness, chemical inertness, low frictional coefficient, and abrasion resistance [1]. The film properties of DLC film is depended on its three kinds of structural factors, that is, sp^2/sp^3 ratio of carbon atom, hydrogen content, and free volume [2]. The sp^2/sp^3 ratio of carbon atom in the DLC film can be determined from the measurement of NEXAFS spectrum with a high precision [3]. Hydrogen content in the DLC film is able to estimate from the combination measurements of elastic recoil detection analysis (ERDA) and Rutherford back scattering (RBS) [4]. On the other hand, free volume in the DLC film has been macroscopically evaluated as film density, but microscopic discussion on it has not been carried out yet. In the pre-sent study, free volume in the 4 kinds of DLC films, which were synthesized by various deposition methods and deposition conditions, was discussed on the results of positron annihilation spectroscopy (PAS). We also measured the nano-indentation hardness of these DLC films. Indentation hardness is expected to decrease as quantity and the size of the free volume increase.

Experiments

We prepared 4 kinds of DLC films for the present study. The first DLC film was deposited by using a plasma enhanced chemical vapor deposition (PE-CVD) method. On the present plasma condition, hydrogen-rich soft DLC film is expected to be deposited. The second DLC film was prepared by the ion plating (IP) method, which is very familiar to the industrial field as hard protective coating. Last DLC films were is synthesized by filtered cathodic vacuum arc (FCVA) method. Two kinds of DLC films were deposited using this method with the different bias voltage, 100 and 400 V. All DLC films were deposited on Si wafer with the film thickness of several hundred nm. The hardness of these DLC films was estimated by an indentation test using a Vickers diamond tip. To obtain the hardness of a film of nm-order thickness, a high-resolution indenter (HM500: Fisher Instruments) with picometer depth resolution was used. The indentation load reached 1 mN at 30 s.

PAS measurement was performed at the slow positron beam system (B-1) at Kyoto University research Reactor (KUR). Doppler broadening profiles of annihilation γ-rays were obtained using a Ge detector for each positron energy. The-low momentum part of spectra was characterized by the line-shape S parameter, which is defined as the number of annihilation events over the range of 511 ± 0.80 keV. S parameters as a function of energy (S-E curves) were measured in the range of 0 - 30 keV. Positron annihilation lifetime spectroscopy (PALS) were performed at an energy of 2 keV, corresponding to the DLC film on Si. Figure 1 shows lifetime spectra for the DLC films formed by the FCVA method. A

Kapton (polyimide) film was measured before and after measurements of the DLC samples as a control sample. Obtained lifetime spectra were analyzed by the PALSfit code assuming one lifetime component.

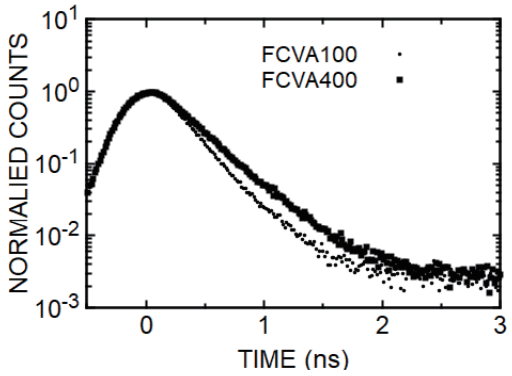

Fig. 1 Lifetime spectra for the DLC samples formed by the FCVA method with different bias voltage.

Results and discussion

Experimental results obtained from PAS measurements were summarized in Table 1 with indentation hardness. Relative S parameter of each DLC film was obtained in comparison with that of and Si.

Table 1. positron lifetime and *S* parameter obtained from PAS measurements with nano-indentation hardness of each DLC films

Deposition method	Bias voltage [V]	Positron lifetime [ns]	Relative S parameter	Indentation hardness [N/mm2]
PE-CVD		0.379	0.932	2488
IP		0.339	0.952	75960
FCVA	400	0.267	0.914	62303
FCVA	100	0.202	0.891	211795

PAS techniques give information on voids consisting of the free volume. It should be noted that positron lifetimes reflect void sizes and S parameters reflect void densities in addition to void sizes. The DLC film, which is synthesized by FCVA method with the bias voltage of 100 V, has very high indentation hardness and its positron lifetime and relative S parameter are smaller than those of other DLC films. The DLC film deposited by PE-CVD method, which has low hardness, has a large positron lifetime and relative S parameter. As described above, positron lifetime decreases with increasing hardness. The relative S parameter also shows a tendency similar to a positron lifetime, but does not completely agree. PAS techniques give information on voids consisting of the free volume. It should be noted that positron lifetimes reflect void sizes but S parameters reflect void densities in addition to void sizes. We think that the hydrogen in the DLC film influenced the results of the S parameter. For deeper consideration, we are planning to obtain the hydrogen content and the sp^2/sp^3 ratio of carbon atom in these films by measuring ERDA and RBS using an electrostatic accelerator and near-edge x-ray fine structure (NEXAFS) using synchrotron radiation, respectively

References

[1] S. Aisenberg et al., J. Appl. Phys. 42, 3963 (1971).
[2] J. Robertson, Surf. Coat. Technol. 50, 185 (1992).
[3] K. Kanda, et al., Jpn. J. Appl. Phys. 41, 4295 (2002).
[4] K. Kanda, et al., Jpn. J. Appl. Phys. 49, 06GH06 (2010).

A demonstration examination about electronic cam control for symmetrical layout type double crystal monochromator

Masato Okui[1) 2)], Atsushi Shimoguchi[1)], Naoki Yato[1)], Ichiro Tsuboki[1)],
Norio Murayama[1)], Tomio Tsuru[1)], Isao Kikuchi[1)] and Norihiro Moriyama[1)]
[1)]Kohzu Precision Co., Ltd., [2)] LASTI, University of Hyogo

Abstract

NGM-RD1 type monochromator was set temporally on BL06 in New SUBARU in August 2019 and have been used for the demonstration examination there since October 2019. This monochromator was designed that is symmetric arrangement both 1st crystal unit and 2nd crystal unit so that its center of gravity would be able to almost perfectly keep to the center of rotation when the main axis is rotated from 5 deg to 70 deg. The monochromator is controlled by the electronic cam algorithm consisted on a new developed control board in order to keep fixed beam exit position. Since the maximum scan speed is up to 5 deg/sec, it is can be expected that a work efficiency of various experiment, for example EXAFS, would improve than a mechanical cam type monochromator.

Introduction

Recently, a specification for monochromator for synchrotron might trend to change from it of the previous generic monochromator mainly used for academic research to suitable specifications for specific experiment with increasing industrial use for synchrotron radiation. High cost performance and economical shall be required in the monochromator for industrial use than the academic use. The economical would be gotten by designing based on common platform. Furthermore, it will be necessary that high throughput from experiment would be done by high-speed rotation of the main axis than previous monochromator.

In Kohzu Precision Co., Ltd, NGM-RD1 type double crystal monochromator was developed by reconsidering and consolidated our available technology and know-how given through designing and manufacturing various our double crystal monochromator [1] [2] [3] [4] [6] that we supplied to the world for 45 years. The main aim of this trial production is in order to show empirically the possibility of our new technology for manufacturing and designing for request of next generations monochromator for synchrotron radiations after 2020's. This monochromator is controlled by an electronic cam algorithm on the new developed control board.

This NGM-RD1 type monochromator was set temporally on BL06 in New SUBARU in August 2019 and have been used for the demonstration examination with the above aim there since October 2019. The authors shall describe the concept of this monochromator, our electronic cam control system and the results of lase demonstration examination in this report.

Concept

This monochromator was designed that is symmetric arrangement both 1st crystal unit and 2nd crystal unit so that the center of gravity would be able to almost perfectly keep to the center of rotation of the main axis when the main axis from 5 deg to 70 deg. Since the center of gravity is kept at one point the top speed of the main axis θ can be more than 5 deg/sec with keeping fixed-exit beam position.

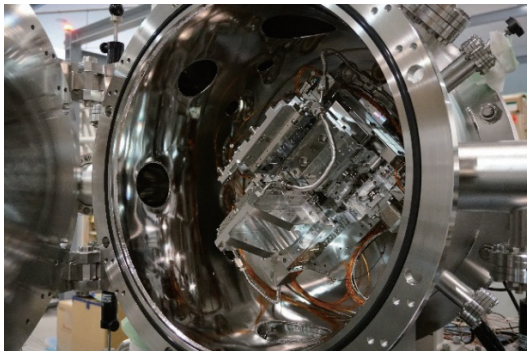

Fig. 1 Photograph of the inside vacuum chamber of NGM-RD1 type monochromator

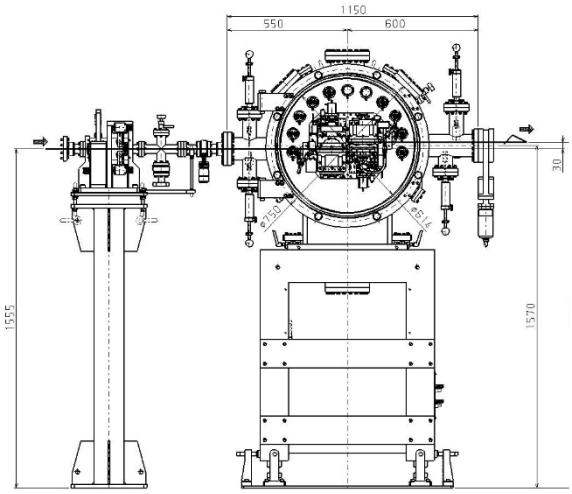

Fig. 2 Schematic design drawing of NGM-RD1 type monochromator

The above Fig. 1 shows the photograph of the inside vacuum chamber of the NGM-RD1 type double crystal monochromator and the Fig. 2 shows the schematic design drawing of the monochromator. Fig. 3 shows the optical pass drawing in this monochromator from 5 deg to 70 deg of Bragg angle, where the beam offset is 30 mm. And the specifications of each axis in this monochromator are shown in Table 1.

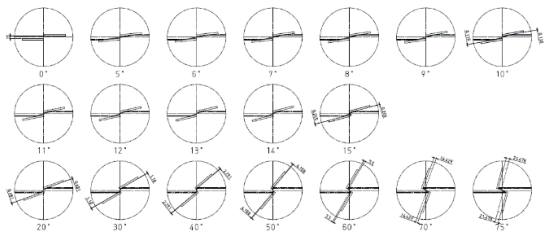

Fig. 3 Optical pass drawing of NGM-RD1 type monochromator

Table 1 Specifications of each axis in NGM-RD1 type double crystal monochromator

Axis	Range	Resolution*	Max. speed
θ	-5deg～75deg	0.072arcsec/step	5deg/sec
Z_1	-21mm～5mm	0.01μm/step	5mm/sec
$\Delta\theta_1$	-1deg～1deg	0.04arcsec/step	0.027deg/sec
Z_2	-5mm～21mm	0.01μm/step	5mm/sec
α_2	-1deg～1deg	0.405arcsec/step	0.277deg/sec

*Micro-step 200 division of motor driver is used in θ, Z_1 and Z_2.

Electronic cam

The distance between the 1st crystal plane and 2nd crystal plane had been adjusted by the physical mechanical cam etc. in the previous monochromator for example KML-9 [2], SSM-1 [3], KHL-3 [4] for keeping the fixed exit-beam position from a monochromator. But electronic cam is system that multiple axes positions is controlled successively by program on control device in real-time corresponding to a main axis angle at every time in order to keep the fixed exit beam position.

The authors already tried to an examination of electronic cam algorithm by the software on a personal computer [5] [6]. In the present study, the above monochromator was controlled by re-newel electronic cam algorithm on the new developed control board.

The top scan speed with keeping the fixed exit -beam position from the 2nd crystal would be able to be 5 deg/sec. The control system of this monochromator is processed by CPU on the electronic substrate with an electronic cam algorithm that is designed specially. The algorithm is that position of both Z_1 axis and Z_2 axis is controlled on real time in order to satisfy the following equation (1) and (2) as θ.

$$Z_1(\theta) = \frac{h}{4}\left(\frac{1}{\cos\theta} - 1\right) \quad (1)$$

$$Z_2(\theta) = -Z_2(\theta) \quad (2)$$

In equation (3) and (4), θ shows Bragg angle, h shows the offset between the height of incident -beam to the monochromator and the height of exit-beam from it and ω shows an angular velocity of Bragg angle. The speed of Z_1 or Z_2, when the angular veracity ω is constant is got by differentiation of $Z_1(\theta)$ as equation (3).

$$\frac{dZ_1(\theta)}{dt} = \frac{h\omega\sin\theta}{4\cos^2\theta} \quad (3)$$

$$\theta = \omega t \quad (4)$$

In this control system, the above electronic cam algorithm on the control board is supplied by velocity override function that change each velocity of Z_1 and Z_2 during driving motor every 1 msec frequently as satisfied equation (3).

Experimental

A demonstration examination of this NGM-RD1 type double crystal monochromator have been done at BL06 in New SUBARU since October 2019.

The synchronism of positions of Z_1 axis and Z_2 axis was gotten by measuring encoder scale value simultaneously, where Renishaw RGSZ20-T and T1601-50M is used as the scale and read head, and Cosmo Techs CFD-2660T was used as a data logger. The resolution of each encoder was 0.002 μm and the control resolution of the both axes was 0.010 μm. In this experiment, rotation of θ was controlled by the trapezoidal driving where the top speed was 2.0 deg/sec and both the acceleration and deceleration time was 0.2 sec. The main axis, θ was rotated from 5 deg to 70 deg by the above speed setting and read the both encoder value with 100 Hz as sampling frequency simultaneously.

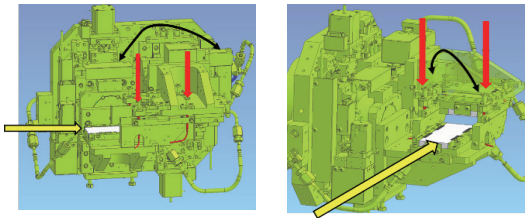

Fig. 4 The schematic drawing about positions of capacitive sensors on 2nd crystal unit of NGM-RD1 type monochromator

4 capacitive sensors were settled near the crystal holder in order to measure a vibration of parallelism of crystals for directions of pitch and roll, respectively. Each sensor position is shown as Fig. 4, where the yellow allows show an incident beam and red arrows are positions of

each capacitive sensors. Used capacitive sensor SSL SMA2604 and 4ch control amplifier is SSL SMA2400. The distance between 2 capacitive sensors was 1.03×10^2 mm, thus measured relative distance from each sensor to each reference plane on the 2nd crystal unit. The sampling frequency is 1 kHz and the measuring time is 5 sec. The vibration on the crystal unit of this monochromator would be able to be estimated from the measured distance by equation (5) where $\Delta\theta$ is angle by vibration h is the measured relative distance from the reference plane of 2nd crystal.

$$\Delta\theta = \frac{h}{103} \qquad (5)$$

The actual measurement was measured during 90 sec. Since the drifting components of actual data that the vibration would be avoided, the data during 5 sec period that would be little effected so as to reduce inclination of the selected interval. was pull out from the all measured data.

During this demonstration experiment, the exit -beam position from the monochromator was monitor by visual observation using an alumina fluorescent screen.

Results and Discussion

The time variation of Z_1 and Z_2 positions controlled by the electronic cam algorithm is shown as Fig. 5, where Z_p shows control value for motor, Ze_1 and Ze_2 show actual each encoder position of Z_1 and Z_2. At this time, θ axis was rotated from 2 deg to 70 deg with 2.0 deg/sec as the top speed.

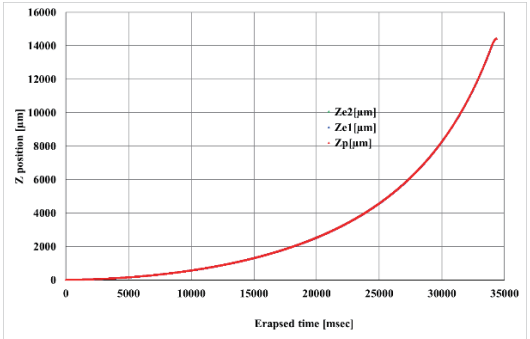

Fig. 5 Time change each control pulse and encoder value of Z axes in NGM-RD1 type monochromator

Fig. 6 shows the actual relative beam height from ideal height that is calculated on the base of each encoder value of Z_1, Z_2 and theta axis. From Fig. 6, it is suggested that the error of height position is increased with time passing. This time passed means θ angle moving to high angle.

The authors suggest it would be caused by greater error of Z_1 and/or Z_2 positioning because of moving distance of a high angle is longer than a low angle. The relative error would be notably observed in acceleration and deciliation time, however, the error of constant speed area would be small than it and the error would be increased to about 6 μm gradually with high angle.

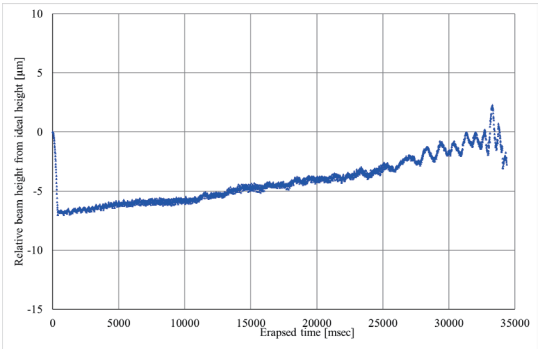

Fig. 6 The actual difference between calculated relative beam height from the ideal height

In this electronic cam algorithm, the rate of control pulse of each Z_1 position and Z_2 position is change by control according to equation (3) by every 1 msec. It would be possible that the difference between control pulse and actual position would have led to the above error of positioning Z_1 and/or Z_2. In the next step of the development, it is suggested that this problem could be able to improve by changing each value of θ, Z_1 and Z_2 using for calculation in an electronic cam algorithm to each encoder value.

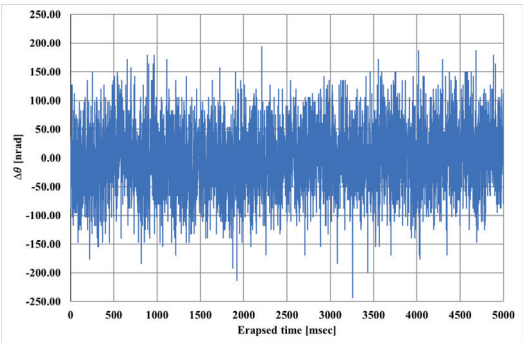

Fig. 7 The positional stability of the parallelism between 1st crystal unit and 2nd crystal unit measured by capacitive sensors

The positional stability of the parallelism between 1st crystals and 2nd crystal is shown as the above Fig. 7. This graph shows time change of the actual vibration between 2 crystals as angle. The histogram in Fig. 8 shows the frequency distribution of it.

The root mean square (RMS) of the distribution of the measured vibrated angles by this system is 5.7×10^{-8} rad. The maximum and minimum value are 29.3×10^{-8} rad and -24.3×10^{-8} rad. The RMS of background of this measuring system using capacitive sensor is estimated about 1.9×10^{-8} rad by actual measurement. In consideration of the background, the RMS of the vibration would be able to estimate as 5.4×10^{-8} rad. In the previous studies [7] [8], the value of SPring-8 is about 5.5×10^{-8} rad and one of HEPS is between from 4×10^{-8} rad to 5×10^{-8} rad, respectively.

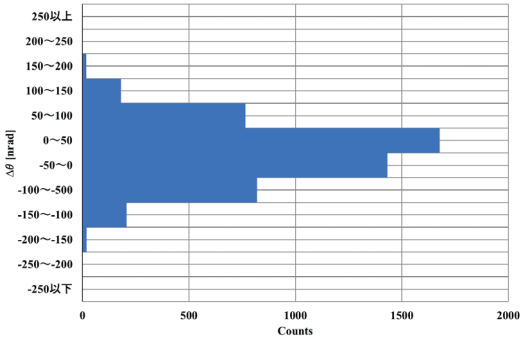

Fig. 8 The histogram of frequency distribution of the parallelism between 1st crystal unit and 2nd crystal unit

(a)

(b)

Fig. 9 The photograph of the beam exit position, respectively, when θ was (a) 2 deg and was (b) 70 deg

In the previous studies [5] [6], they used LN2 system as cooling unit, but the distribution by [6] could be approximately a quadratic curve and will be able to estimate converged about from 4×10^{-8} to 5×10^{-8} rad without LN2 vibration. The present result would be promising to be considered comparable stabilities from the above consideration. From the result of a fast Fourier translation, the 1st peak is estimated to 163 Hz, and the amplitude is estimated to 1.1×10^{-8} rad.

The actual beam positions when the main axis θ is 2 deg and 70 deg, respectively are shown in Fig. 9 (a) and (b). These photographs take the beam monitor of an alumina fluorescent. The photon energy is about 56.6 keV and about 2.1 keV, respectively. In the Fig. 9 (b) the beam image is weak than the high-energy-side since the low emission of alumina fluorescent, but the exit beam position would be able to recognize almost same position to the low energy side in Fig. 9 (a).

This comparing with the exit beam positions of the above photographs would be led to that this electronic cam system can enough control each axis practically in order to keep fixed beam exit position at energy range from 2keV to 55keV. In this case, the scan top speed is 5 deg/sec, and the scanning time is less than 14 sec from 2 deg to 70 deg.

From the above results and its discussion, it can be suggested that this symmetric layout monochromator controlled by the electronic cam algorithm on a board would be effective for quickly scanning in high through put at the wide photon energy range as like measuring extend X-ray absorption fine structure.

Acknowledgement

The authors thank deeply for support of the experiment in BL06, New SUBARU by Prof. Dr. Kazuhiro Kanda and they thank also for support by colleague in Kohzu Precision Co., Ltd.

References

[1] Kawata & Ando, Nucl. Instrum. Methods, **A246,** 368-372. (1986).

[2] Matsushita *et al*., Nucl. Instrum. Methods, **A246,** 377-379. (1986).

[3] Yabashi *et al*., Proc. SPIE, **3773,** 2-11. (1999).

[4] Kawata *et al*., AIP Conf. Proc., **705,** 663-666. (2004).

[5] Okui *et al*., LASTI Annual Report, **17**, 15-16. (2016).

[6] Okui *et al*., AIP Conf. Proc., **1741**, 030033, (2016).

[7] Liang *et al*., MEDISI2018 Proc., 430-434, (2018).

[8] Yamazaki *et al*., AIP Conf. Proc., **2054**, 060018, (2019).

Refractive-index changes in SiO_2 Films by Undurator Radiation with and without a multilayer spectrometer

K. Moriwaki[1], R. Fujiwara[1], and K. Kanda[2]
[1]Graduate School of Eng., Kobe Univ., [2]LASTI, Univ. Hyogo

Abstract

SiO_2 films are compared after refractive-index modifications using undurator radiation (UR) with and without a multilayer spectrometer in the NewSUBARU (BL7A) for optical device applications. By varying the UR peak-energy, the measured refractive indices show higher values by lower peak energy irradiation with and without spectrometer. All the modification layers in the films are found to be very shallow (less than 60nm), which might depend on the short penetration length by the irradiation X-ray. The refractive index change increases up to 1500 mA·h by increasing the UR dose, which make it possible to control the value for applications.

Introduction

Synchrotron radiation (SR) can be used for radiation-induced refractive-index modifications in SiO_2 material[1-2)] for applications to optical devices. Undurator radiation (UR) can select a useful irradiation wavelength, and has very high intensity. By using a multilayer spectrometer, UR will become more useful for the device applications, because the most suitable peak energy without higher order can be used. In this report, UR irradiation effects are investigated for comparison between with and without a spectrometer, especially by changing the irradiating peak energy. The depth profile for the samples are also investigated by etching the samples, because it is very important for optical device applications.

Experiments and Results

Thermally grown SiO_2 films (0.5μm thickness) on Si substrates and fused quartz substrates were used for the UR radiation (BL-7A) at an electron current of 300mA with and without a multilayer spectrometer. The UR with peak energy ranging from 80 to 480 eV was used with the spectrometer including the 3rd and the 5th order peaks. Irradiated samples were characterized mainly by refractive-index measurements using a reflection spectrophotometry. Optical absorption was also used for characterizing defects in the irradiated samples. The samples were etched by RIE (Reactive Ion Etching) for the depth profiles of the refractive indices.

In the previous study, very high refractive index changes of the order of 10^{-2} were found in the sample surface after the irradiation by UR without the spectrometer, which were mainly by the surface reduction layer having Si-Si bonds[1)]. For the samples irradiated by UR with spectrometer, the surface reduction layer was not found, probably because of the lower irradiation intensity and/or higher peak energy ang longer penetration depth. In this study, we have achieved higher-precision measurements of the refractive

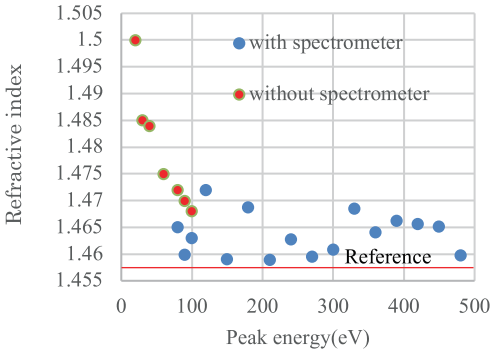

Fig.1 Refractive indices changes at λ=633nm for SiO_2 films after irradiation by UR with and without the spectrometer as a function of peak energy at a dose of 500 mA· h.

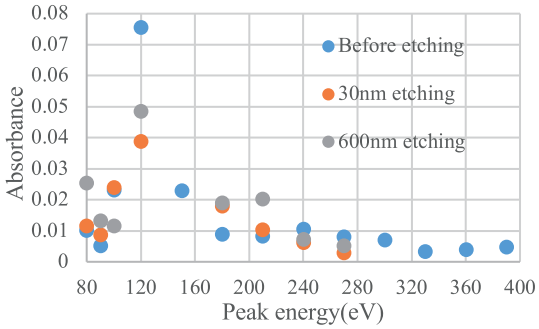

Fig.2 Absorbance at a wavelength of 245nm for an SiO_2 film after UR radiation with a dose of 500 mA· h using the spectrometer as a function of peak energy before and after etching.

indices by fixing the accurate thickness of 500nm for the thermally grown SiO_2 films. By using the measurements, highly reproducible values of the refractive index change can be obtained. The measured refractive-indices are shown in Fig.1, where higher values are obtained at lower peak energy range by the irradiation both with and without the spectrometer. It is not so clear in Fig.1, but another peak of the refractive index change might be shown at a peak energy of 120 eV in the irradiation with the spectrometer. That is confirmed by the optical absorbance measurements before and after etching the irradiated sample (Fig.2). The cause of the 120eV peak in Fig.2 is not clear at present, but the results were highly reproducible.

As we can expect it, the refractive index increased by increasing the UR dose up to 500 mA·h (Fig.3) and up to 1500 mA·h (Fig.4). When the storage-ring current for the UR is 300 mA, a necessary change for an application in the refractive index change of 2.0×10^{-4} is obtained by the irradiation time for less than ten minutes

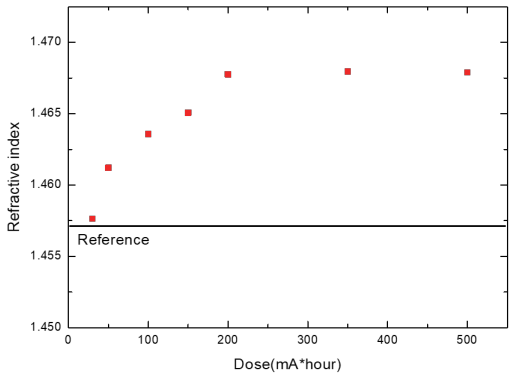

Fig.3 Dose dependence of the refractive index in SiO_2 films after UR radiation with the spectrometer at a peak energy of 180 eV.

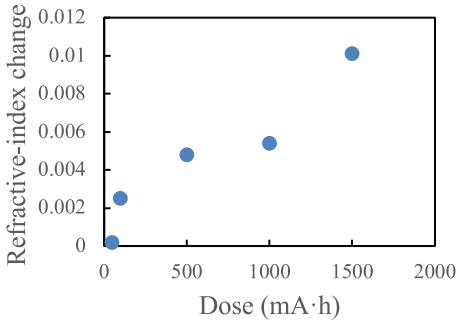

Fig.4 Dose dependence of the refractive index changes in SiO_2 films after UR radiation with the spectrometer at a peak energy of 100 eV.

with the spectrometer and around 1 minute or so without the spectrometer. Thus, it is found that the refractive index can be controlled by changing the peak energy and the dose during irradiation for applications.

The UR-irradiated samples were etched using RIE to analyze the refractive index in the depth direction. For samples irradiated at 80-120 peak energies, the refractive index changes in the shallow layer (< 60 nm) on the sample surface were extremely larger than the deeper ones. The refractive index decreased rapidly when the surface shallow layer was removed. After etching by 60 nm, almost no increase in the refractive index was observed (Fig.5). This might be correlated to the penetration depth of X-rays. The shallow modification layer might make it difficult for many optical applications such as waveguides. By comparing the samples after the irradiation, deeper refractive index change were confirmed for samples by SR irradiation, comparing to those by UR. This might be due to the effects of higher energy and longer penetration-depth X-rays contained in SR. From these results, a guideline has been obtained for the application of UR to various optical devices fabrication.

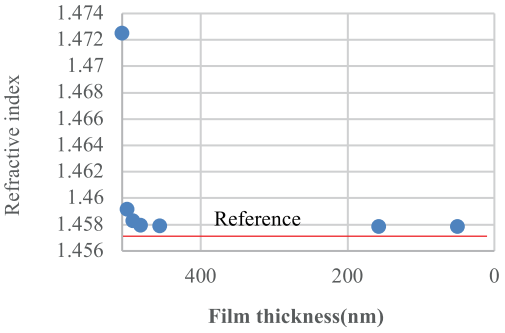

Fig.5 Depth profile during etching for an SiO_2 film after UR radiation with the spectrometer at a peak energy of 120 eV.

Conclusions

SiO_2 films were irradiated by UR with and without the spectrometer for applications to optical devices. Although higher Refractive indices of the order of 10^{-2} were obtained, the higher index layers were shallow, so that it might not be easy for usual photonic applications.

References

[1] K.Moriwaki et al., LASTI Annual Report vol.17 (2015)55.
[2] K.Moriwaki et al., LASTI Annual Report vol.20 (2018)18.

Experimental studies to produce a high energy photon beam by inverse Compton scattering of soft X-rays

Norihito Muramatsu[1], Masahiro Okabe[1], Shinsuke Suzuki[2], Schin Daté[3], Hajime Shimizu[1], Haruo Ohkuma[3], Kazuhiro Kanda[4], Shuji Miyamoto[4], Tetsuo Harada[4], Takeo Watanabe[4], Manabu Miyabe[1], Atsushi Tokiyasu[1]
[1] ELPH, Tohoku University, [2] JASRI/SPring-8, [3] RCNP, Osaka University, [4] LASTI, University of Hyogo

Abstract

A high energy photon (γ-ray) beam up to 0.6 GeV can be produced via inverse Compton scattering of 92 eV X-rays from 1 GeV electrons at NewSUBARU. The soft X-rays are obtained from the short undulator at BL07 with the backward reflection using a Mo/Si multi-layer mirror. For the new beam production method, we have developed a cylindrical mirror to focus the reflected X-rays at the straight section of the storage ring, and constructed key detector systems to monitor X-rays and a generated γ beam. The performance of them were tested at BL07A by using the undulator and a gas bremsstrahlung γ beam.

Introduction

Inverse Compton scattering at an electron storage ring is a common method to produce a high energy photon (γ-ray) beam. In our project [1], soft X-rays of 92 eV from an undulator are reflected backwardly and injected into the storage ring instead of laser light. This procedure achieves much higher energies for the produced γ beam, increasing the Compton edge significantly. Such a beam must be useful for new generation experiments of hadron physics by enabling the production of heavier particles.

We carry out a series of demonstration experiments to develop basic techniques for the inverse Compton scattering of soft X-rays at NewSUBARU, whose electron energy is 1 or 1.5 GeV. In case of the 1 GeV operation, the maximum energy of a γ beam becomes 585 MeV. For the test experiments, we use a short undulator (total length: 2.28 m, period length: 7.6 cm) at BL07 as an X-ray source. The radiated X-rays are reflected into the original straight section by using a Mo/Si multi-layer mirror, installed at BL07A.

Preparation of detectors

Two vacuum chambers were installed at BL07A. One large chamber with a size of W1120×D820×H610 mm^3 was set up 16.7 m downstream of the undulator center. A multi-layer mirror was placed on high precision auto-stages inside this chamber with cooling water circulation. The other chamber, shown in Fig. 1(a), was installed 2.6 m upstream of the large mirror chamber, in order to monitor radiated and reflected X-rays. A wire scanning detector was mounted for the measurement of their profiles and relative intensities based on an increase of micro current due to a photoelectric effect at ϕ0.2 mm tungsten wires. Two wires were directed vertically and horizontally on a moving stage attached to an air cylinder together with a potentiometer.

For the energy measurement of a γ beam, a high-resolution electromagnetic calorimeter (ΔE/E = 1.7% at 1 GeV) was made by assembling nine $PbWO_4$ (PWO) crystals, the individual size of which is 20 ×20×200 mm^3. It was set up downstream of the switching mirror for BL07A and BL07B inside the ring tunnel, as shown in Fig. 1(b). A γ beam profile monitor was also prepared by crossing 1 mm^2 scintillating fibers in the area of 50×50 mm^2. The readout of scintillating fibers was done in each two channels (namely, 2 mm digitization) by using multi-pixel photon counters (MPPC). For making a trigger signal at data taking, a veto counter, a thin lead converter, and a trigger counter were additionally placed upstream of the profile monitor and the PWO calorimeter.

Development of an X-ray mirror

A base plate for the Mo/Si multi-layer mirror was developed with a low thermal

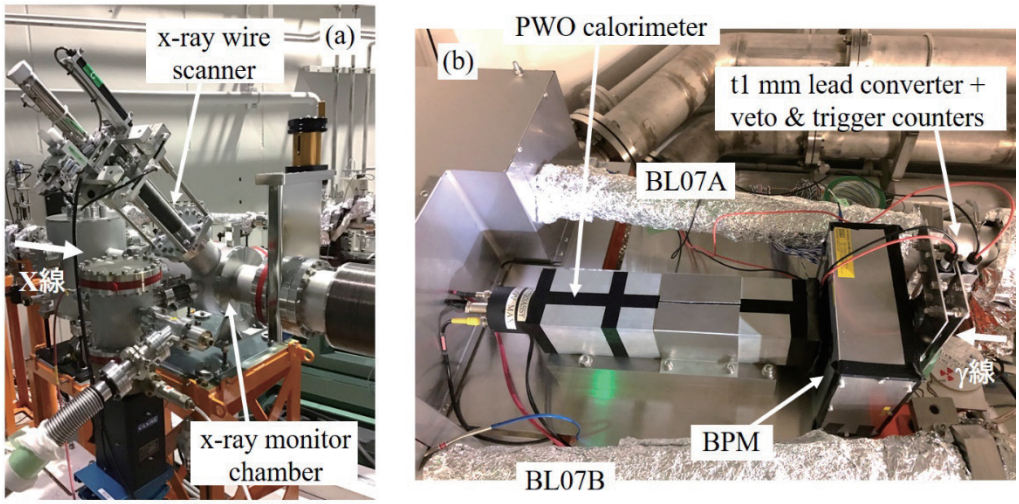

Figure 1 Pictures of (a) X-ray monitor chamber and (b) γ-beam detectors, installed at NewSUBARU BL07A.

expansion glass ceramic (Zerodur). The switching mirror of BL07 possesses a spherical surface, so the X-rays at the reflection mirror chamber are parallel in the horizontal direction but divergent for the vertical component. In order to focus the reflected X-rays at the straight section of BL07, we need a cylindrical multi-layer mirror with a curvature radius of 16.7 m, which corresponds to the distance between the mirror and the Compton scattering point. We developed a unique method to make the cylindrical mirror base, as described in the previous annual report [2]. The Zerodur plate has been finally cut in 50×50 mm^2, which is large enough compared with the X-ray beam size of about 20×20 mm^2. The produced curvature radius was confirmed by measuring the maximum depth at the mirror surface center with a micro-gauge (18.7 μm for the 50 mm width) and alternatively counting the number of Newton fringes with a flat plate under a Na lamp (128 interference fringes for the 50 mm width). The mirror base was coated by Mo/Si multi-layers, and the reflectivity was confirmed to reach 55% for the backward reflection of 92 eV X-rays [3].

Tests with a bremsstrahlung γ beam

The performance of X-ray and γ-beam detectors has been tested by using X-rays from the BL07 short undulator and a γ beam from residual gas bremsstrahlung inside the storage ring. Figure 2(a) shows the vertical profile of undulator X-rays at the wire scanning detector. A wire position during the air cylinder operation was determined based on the voltage measurement by a potentiometer. This measurement was performed with a narrow slit, so the observed X-ray beam size was about 1 mm in σ. A variation of the X-ray beam intensity is clearly seen depending on the undulator gap setting.

Figure 2(b) shows the energy spectra of γ beams from gas bremsstrahlung with NewSUBARU operation at 1 and 1.5 GeV. Both spectra were measured by using the PWO calorimeter. The linearity of energy measurement is confirmed by comparing the upper edges of two spectra. Figure 2(c) shows a result of γ-beam profile measurement by using the γ-beam profile monitor, made of scintillating fibers. The γ beam is narrow enough with a gaussian sigma of about 6 mm.

Prospect of demonstration experiments

We are going to test the production of a γ beam arising from the inverse Compton scattering of undulator X-rays by using the developed mirror and detectors. We will confirm technical issues on the heat load of an X-ray mirror, the cooling capability of a mirror holder, the reflectivity of X-rays, the focusing performance of a cylindrical X-ray mirror, and so on. Then, we will measure the energy spectrum and

intensity of an X-ray induced γ beam for comparison with prior estimations.

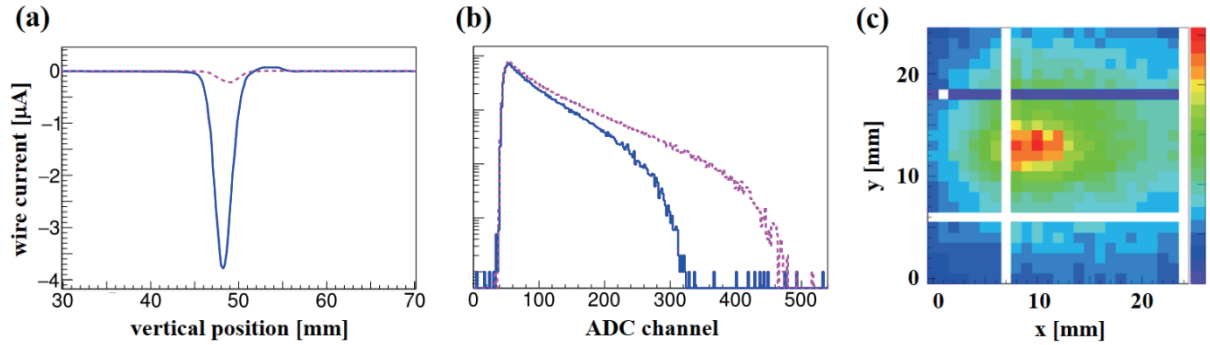

Figure 2 (a) Vertical profiles of undulator X-rays at the wire scanning detector. The solid and dashed lines were obtained when the undulator gap was set to 48 mm and fully opened, respectively. (b) Energy spectra of a bremsstrahlung γ beam at the PWO calorimeter. The solid and dashed lines correspond to the storage-ring operation energies of 1 and 1.5 GeV, respectively. (c) A Two-dimensional profile of a bremsstrahlung beam at the γ-beam profile monitor.

Acknowledgments

This research was supported in part by Grant-in-Aid for Challenging Research (Pioneering) No. 18H05325/20K20344.

References

[1]. http://www.rcnp.osaka-u.ac.jp/~mura/kaitaku/
[2]. "Production of a high energy beam via backward Compton scattering of soft X-rays from a short undulator", N. Muramatsu et al., LASTI Annual Report Vol.20 (2018) 22.
[3]. A test experiment at BL10 by T. Harada.

Graphene synthesis from pentacene-based molecules on Ni film by soft X-ray irradiation

Akira Heya[1], Tomohiro Oonuki[1], Ryuichi Utimi[1], Kazuhiro Kanda[2], Ryo Yamasaki[3], and Koji Sumitomo[1]

[1]Graduate School of Engineering, University of Hyogo, [2] LASTI, University of Hyogo, [3] Tocalo Co., Ltd.

Abstract

We investigated the use of soft X-rays to form nanographenes. A mixture film consisting of pentacene, 6,13-dihydropentacene, and pentacene oligomers, prepared by hot mesh deposition, were irradiated using soft X-rays generated in the NewSUBARU synchrotron radiation facility. The hydrogen desorption and catalytic effect of the Ni film on the quartz substrate during soft X-ray irradiation enhanced the polymerization of pentacene. It is considered that the pentacene oligomer acts as a nucleus of nanographene.

Introduction

The nanographene molecules are attractive two-dimensional materials consisting of carbon atoms arranged in a hexagonal lattice. The graphene nanoribbons (GNRs) have band gaps that depend on the ribbon width. Therefore, GNRs are expected to be used in next-generation semiconductor devices as part of logical elements, transistors, spin transistors, and gas sensors.

We have investigated the fabrication method of GNRs using pentacene (Pn), H_2 gas, and W mesh. This method is named hot mesh deposition (HMD) [1]. 6,13-dihydropentacene (DHP) was generated from Pn as a precursor by HMD. In addition, we discovered that the threshold temperature for crystallization of inorganic semiconductor materials was reduced by irradiation of soft X-ray [2]. Therefore, the combination of HMD and soft X-ray irradiation is expected as a novel method for GNR fabrication method.

In this study, we examined whether GNRs can be fabricated by high-intensity soft X-ray irradiation on a nanocarbon film containing Pn, DHP, and pentacene oligomer (PO) molecules prepared by HMD.

Experimental

A W mesh (10×55 mm^2) with a wire diameter of 0.1 mm and 30 holes/inch was used. Ni particles were supported on the W mesh surface with an atmospheric plasma spray. A mixture of Ar and H_2 was used as the plasma generation gas. The plasma power was 38.5 kW. The Ni was supported on both faces. The W mesh with supported Ni area ratios of 3% ($W_{Ni(3\%)}$) was prepared.

The HMD apparatus is already shown in elsewhere [1]. The deposition of nanocarbon film was performed using a Pn source. A $W_{Ni(3\%)}$ mesh was set between the pentacene source in a Mo boat and a substrate 20×20 mm^2 in size. The flow rate of H_2 and gas pressure were 400 sccm and 30 Pa, respectively. The distance between the mesh and the substrate was fixed at 30 mm. A pentacene source (30 mg) in a Mo boat was placed in a 26-mm diameter quartz tube. To vaporize the pentacene molecules, the Mo boat was heated up to 315°C using a coil heater. The $W_{Ni(3\%)}$ mesh temperature (T_{mesh}) was 1480 °C.

The irradiation of soft X-rays was carried out at BL07A of NewSUBARU. The light source of BL07A was a 2.28 m undulator. The storage-ring energy was 1 GeV. The beam size measured with a fluorescent plate on the sample surface was 7.5 × 7.5 mm^2. The photon energy was 300 eV. The storage-ring current and dose were 300 mA and 100 mA h, respectively.

The changes in molecular structure by soft X-ray irradiation were evaluated by Raman scattering and X-ray diffraction measurements.

Results and discussion

The Raman spectra of the nanocarbon film prepared by HMD before and after soft X-ray irradiation are shown in Fig. 1. The broad peaks of D and G bands at 1369 and 1587 cm^{-1} were observed before soft X-ray irradiation. It indicates that the pentacene-based precursors were polymerized to graphite-like nanocarbon by the catalytic aid of Ni film. The sharp peaks of the D, G, and 2D bands attributed to graphene at 1342, 1578, and 2691 cm^{-1}, respectively, were observed after soft X-ray irradiation. Peak positions of armchair GNRs fabricated by the bottom-up process starting with low-weight molecules were around 1340 and 1600 cm^{-1} [3]. It was, therefore, concluded that the nanocarbon film fabricated by HMD and soft X-ray irradiation was not a GNR.

The XRD patterns of the nanocarbon films consisting of Pn, DHP, and PO before and after soft X-ray irradiation are shown in Fig. 2. A diffraction peak due to a nanocarbon film was not observed before soft X-ray irradiation. It is hypothesized that the ordering of pentacene disappeared due to the influence of DHP and PO. The graphite (002) at 26.46° was observed after soft X-ray irradiation. It was found that graphene was formed using a Ni film and a nanocarbon film consisting of Pn, DHP, and PO by soft X-ray irradiation.

From the Raman spectra and XRD patterns, graphene synthesis from Pn using soft X-ray irradiation was confirmed. However, our aim is GNR synthesis. It is thought that the suppression of unexpected polymerization of pentacene-based precursors is necessary to obtain GNRs.

To control polymerization, the effects of soft X-ray irradiation on polymerization are discussed. A schematic diagram of the effects of soft X-rays on polymerization reaction of the nanocarbon film consisting of Pn, DHP, and PO on the Ni film is shown in Fig. 3. The soft X-ray is directly absorbed in the nanocarbon film. On the other hand, as a Ni atom absorbs soft X-rays, the electrons in the Ni 3s and 3p orbital levels (111 and 67 eV) are excited, and the electrons at the interface between the nanocarbon and Ni films move into the nanocarbon film. It is thought that some chemical reactions such C-H bond-breaking and C=C bond-formation are enhanced by photoelectron transfer reaction due to soft X-ray excitation and supply of excited electrons from the Ni film.

Conclusions

By using a nanocarbon film including PO prepared on a Ni film using a $W_{Ni(3\%)}$ mesh prepared by HMD, nanographene was produced by soft X-ray irradiation. It was considered that the hydrogen desorption and catalytic effect of a Ni film excited by soft X-rays during soft X-ray irradiation assisted pentacene polymerization. However, to obtain the GNRs, the issue of optimization the conditions of PO formation and soft X-ray irradiation still remained.

References

[1] A. Heya, R. Yamasaki, and N. Matsuo, Thin Solid Films **675** (2019) 143.

[2] A. Heya, K. Kanda, K. Toko, T. Sadoh, S. Amano, N. Matsuo, S. Miyamoto, M. Miyao, T. Mochizuki, Thin Solid Films **534** (2013) 334.

[3] A. Shiotari, T. Kumagai, M. Wolf, J. Phys. Chem. C **118** (2014) 11806.

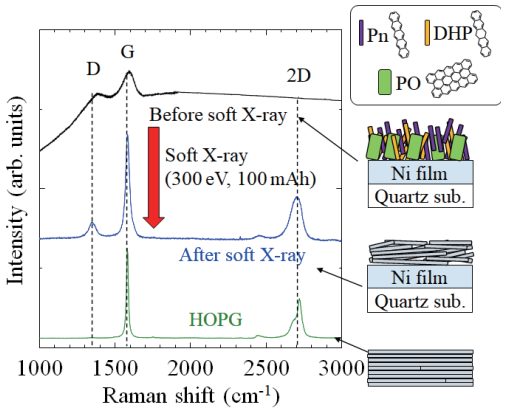

Fig. 1. Raman spectra of nanocarbon films consisting of Pn, DHP, and PO before and after soft X-ray irradiation. The Raman spectrum of HOPG is shown as a reference.

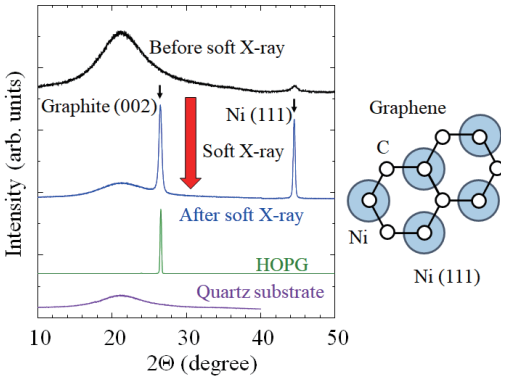

Fig. 2. XRD patterns of nanocarbon films consisting of Pn, DHP, and PO before and after soft X-ray irradiation. XRD patterns of HOPG and quartz substrate are shown for reference. Atomic configuration of C in graphene on Ni (111) is shown in the right part.

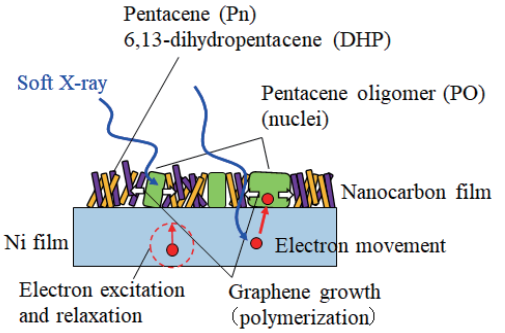

Fig. 3 Schematic diagram of the effects of soft X-rays on the polymerization reaction of the nanocarbon films consisting of Pn, DHP, and PO on the Ni film.

Soft X-ray NEXAFS Analysis of Thin Pt and RuO_x Catalyst for Water Electrolysis

Ryuki Tsuji[1], Yuuki Koshino[1], Hideaki Masutani[1], Yuichi Haruyama[2], Masahito Niibe[2] Satoru Suzuki[2], Seiji Nakashima[1], Hironori Fujisawa[1], and Seigo Ito[1]
[1]Graduate School of Engineering, University of Hyogo, [2]LASTI, University of Hyogo

Abstract

Near-edge X-ray absorption fine structure (NEXAFS) in NewSUBARU BL-09A was used to analyze structure of Pt and RuO_x catalysts which were fabricated by soaking inexpensive graphite electrodes (pencil-lead graphite-rod: PGR) into the precursor solutions of Pt and RuO_x catalysts and by a simple flame-annealing to be the small amount of Pt and RuO_x catalyst layers. It was found that platinum and ruthenium was deposited as zero-valence metal (Pt) and oxide (RuO_x), respectively, analyzed by NEXAFS and XPS analysis. Such an inexpensive and rapid catalyst electrode preparation method on PGR used flame-annealing is very significant for the evaluation of initial catalyst activity.

Introduction

Hydrogen (H_2) is attracting worldwide attention as a new energy storage source. Water electrolysis (WE) is the most promising candidate for H_2 production from the viewpoint of using renewable energy sources such as sunlight and wind power without CO_2 emission. In order to reach a practical energy conversion efficiency, it is necessary to lower the overpotential of the hydrogen evolution reaction (HER) at the cathode and the oxygen evolution reaction (OER) at the anode. Although noble metals such as platinum, iridium and ruthenium can exhibit high catalytic activity, these elements are low natural abundance and quite expensive. Hence, it is important to reduce the amount of noble-metal catalyst on electrodes.

In this work, we have prepared Pt and RuO_x catalysts deposited on a pencil-lead graphite-rod (PGR) by coating the precursor solution and using flame-annealing,[1, 2] which is a very easy method to fabricate electrocatalysts in a short time (Fig.1). In addition, because the required amount of catalyst is quite low in this method, it is possible to produce the high-active catalysts at a very low cost. In this work, the performance of water-electrolysis catalyst (Pt and RuO_x) deposited on a PGR by flame-annealing was analyzed and evaluated by material analysis including near-edge X-ray absorption fine structure (NEXAFS), and electrochemical measurements.

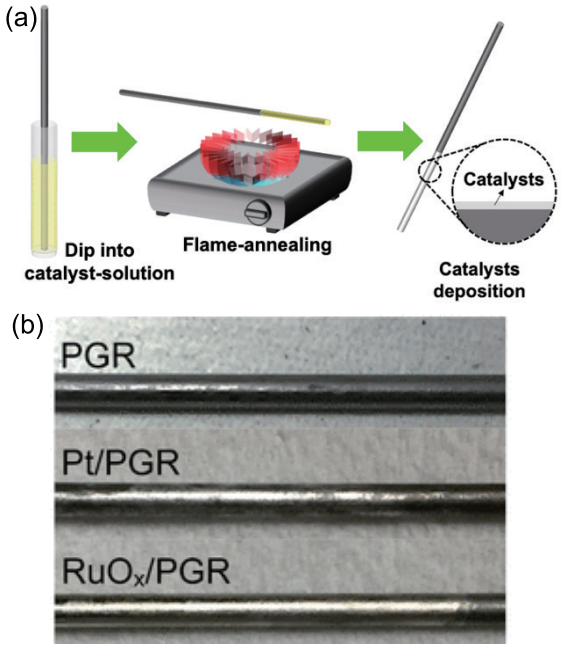

Fig. 1. (a) Schematic illustration of the preparation process of catalyst/PGR electrodes. (b) photographs of the PGR surface with/without catalysts (Pt and RuO_x) [1].

Experiments and Results

The atomic-bonding conditions between Pt, Ru, carbon, and oxygen on the PGR were analyzed using TEY and TFY-NEXAFS by soft X-ray irradiation (NewSUBARU, BL-09A). The results of Pt/PGR and RuO_x/PGR are shown in Fig. 2 and 3. The TEY method is sensitive to the outermost surface; on the other hand, the TFY method is a bulk-sensitive measurement. In the PGR, π^* (=C) and σ^* (−C) peaks were observed at about 285.5 and 293 eV, respectively, indicating sp^2 of graphite. In TEY C*K*-edge of Pt/PGR and RuO_x/PGR, π^* and σ^* peaks of graphite were hardly confirmed (Fig. 2a and 3a). However, at TFY C*K*-edge, peaks of π^* and σ^* were noticeable, confirming that Pt and RuO_x covered the PGR surface (Fig. 2b and 3b), uniformly. The O*K*-edge of Pt/PGR and RuO_x/PGR is shown in Fig. 2c and 3c. In the PGR, peaks were observed at 532 and 538 eV, which are attributed to π^* (=O) and σ^* (−O), respectively. In addition, because oxygen peaks were not observed in the TEY spectrum of Pt/PGR, it was considered that Pt does not combine with oxygen and exists as Pt of 0 valence. In RuO_x/PGR and RuO_2, two peaks in π^* were observed, both of which had the same peak shape. This NEXAFS result indicating the presence of RuO_2. From the results of material analysis, it was considered that Pt covered uniformly the PGR as the metallic condition, and it had not bonded with carbon or oxygen. In RuO_x/PGR, on the other hand, ruthenium and oxygen were combined during flame-annealing, and it was thought that they were deposited on the PGR surface as RuO_2, mainly. Also, the relationship between the deposited catalysts and the carbon of the PGR was not suggested. From these considerations, it was found that flame-annealing can coat Pt and RuO_x on the PGR surface. In addition, it was found that Pt was deposited as 0 valence metal and that Ru became RuO_2 on the PGR surface.

In this report, the flame-annealing deposition methods was introduced for thin Pt and RuO_x catalyst layers on very cheap PGR electrodes for the water electrolysis. It was found that H_2PtCl_6 became a zero-valent metal Pt and that $Ru(NO)(NO_3)_3$ reacts with oxygen in the air by NEXAFS analysis.

References

[1] R. Tsuji, *et al.*, *ACS Omega*, **5**, 11, pp.6090-6099 (2020).

[2] R. Tsuji, *et al.*, *ACS Sustainable Chem. Eng.*, **7**, 6, pp.5681-5689 (2019).

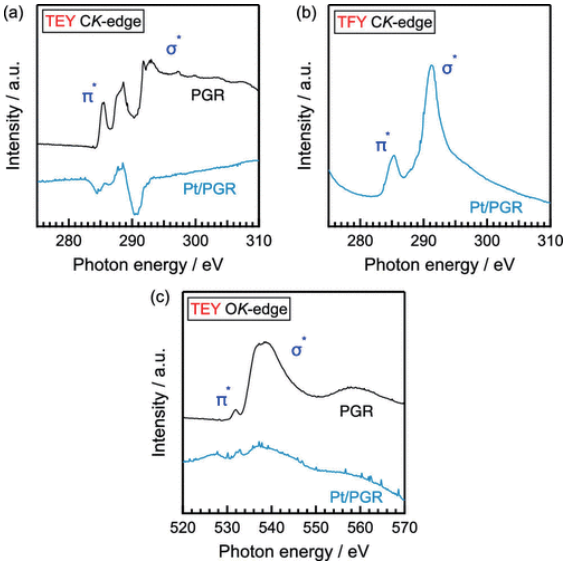

Fig. 2. TEY and TFY-XAFS analysis of Pt/PGR: (a) TEY, C*K*-edge; (b) TFY, C*K*-edge; and (c) TEY, O*K*-edge [1].

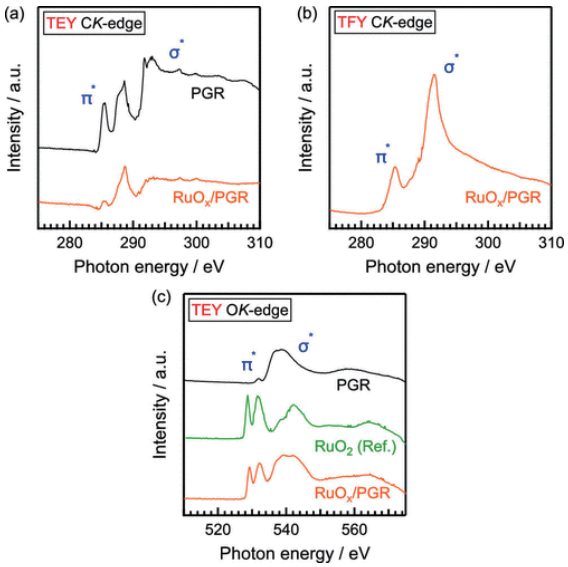

Fig. 3. TEY and TFY-XAFS analysis of RuO_x/PGR: (a) TEY, C*K*-edge; (b) TFY, C*K*-edge; and (c) TEY, O*K*-edge [1].

Development of a new surface treatment method using atomic hydrogen in material analysis beamline BL-07

Y. Haruyama[1], A. Heya[2], K. Sumitomo[2], and S. Ito[2]
[1]LASTI, University of Hyogo, [2]Graduate School of Engineering, University of Hyogo

Abstract

A new surface treatment apparatus using atomic hydrogen generated on heated tungsten was constructed at the end station of a material analysis beamline BL-07B. Since this apparatus is directly connected to a vacuum chamber through a gate valve, it is possible to evaluate samples treated by atomic hydrogen without air exposure. It is confirmed that the surface contamination is drastically reduced in X-ray photoelectron spectroscopy after the treatment using atomic hydrogen. Presently, we are planning to investigate the surface reaction between atomic hydrogen and the solid surface at various materials using synchrotron radiation.

Introduction

Since the atomic hydrogen, which is generated on heated tungsten under ambient hydrogen gas, is very reactive, it has been used for a wide range of applications such as the low-temperature crystallization of a-Si [1], the dry etching of crystalline silicon [2], vacuum chamber cleaning and photoresist removal [3]. One of the authors has developed as the atomic hydrogen annealing (AHA) treatment [1, 4]. Although many studies using the AHA treatment were reported, there still remain many problems to be solved on the surface reaction between atomic hydrogen and the solid surface. Therefore, it is important to investigate the effect of the AHA treatment on the solid surface.

In this study, the atomic hydrogen treatment apparatus was constructed at the end station of a synchrotron radiation (SR) beamline to evaluate samples after AHA treatment without air exposure. As a first trial analysis, the Si and Cu samples were evaluated by the X-ray photoelectron spectroscopy.

Experiments

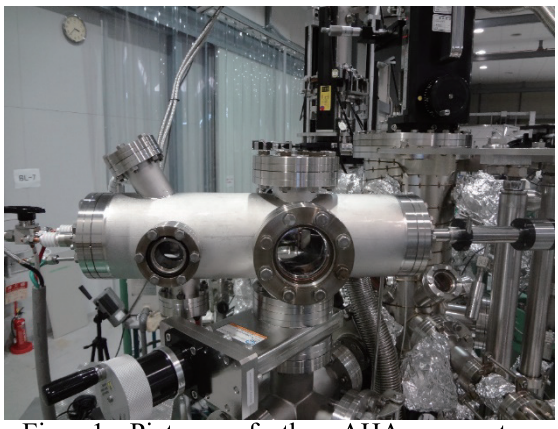

Fig. 1 Picture of the AHA apparatus constructed at BL-07B end station.

The AHA apparatus was constructed at the BL-07B end station of the NewSUBARU synchrotron radiation facility, the University of Hyogo. This apparatus is directly connected to a vacuum chamber through a gate valve. In Figs. 1 and 2, a picture and a schematic diagram of the AHA apparatus are shown. As a filament, tungsten mesh composed of 0.03 mm ϕ wire at the density of 30 wires per inch was used and heated at the temperature of about 1700 °C. Then, the Ar(95%) and H_2(5%) mixture gas was filled at the pressure of 10 Pa and at the flow rate of 100 sccm during the AHA treatment. AHA treatments on the Si and Cu samples was kept below 200 °C during the AHA treatment.

XPS experiments were performed by using the conventional photoelectron spectroscopy apparatus, which was mounted with a R3000 (VG scienta) hemispherical electron energy analyzer. The Mg Kα line (hν = 1253.6 eV) was used as an X-ray source and was incident at 45° with respect to the surface normal. XPS spectra were measured at the emission angle of 45° to the surface normal. The total energy resolution was ~0.7 eV. The base pressure in the photoelectron analysis chamber was 4×10^{-8} Pa. The typical size of the Si and Cu samples for the XPS measurements was $10\times10\times1$ mm^3.

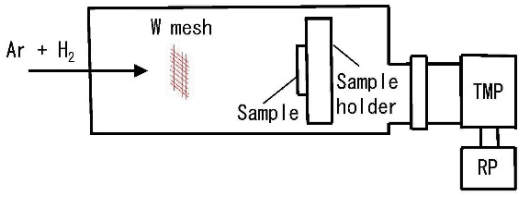

Fig. 2 Schematic diagram of the AHA apparatus.

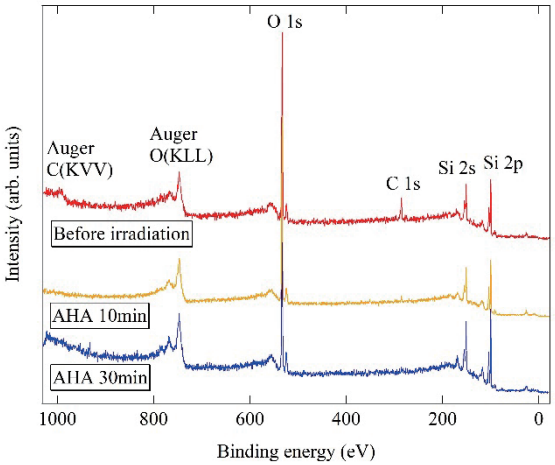

Fig. 3 The wide range of XPS spectra of a Si sample as a function of the AHA treatment time.

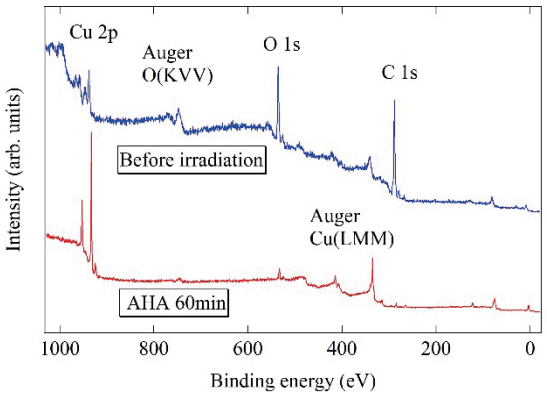

Fig. 4 The wide range of XPS spectra of a Cu sample before the AHA treatment and after the AHA treatment for 60 minutes.

Results and discussion

Figure 3 shows the wide range of XPS spectra of a Si sample as a function of the AHA treatment time. Before AHA treatment, several peaks originating from the C, O, and Si atoms were observed in the photoelectron spectrum. The peaks at ~1000, ~750, ~530, ~290, ~150 and ~100 eV were assigned to Auger levels by C KVV and O KLL decay process, the O 1s level, C 1s, Si 2s and Si 2p levels, respectively [5]. These peak assignments are denoted beside the top spectrum. It is clear that there are C and O atoms on the surface of the Si sample before AHA treatment. After AHA treatment for 10 minutes, the peak intensity of the C 1s level was decreased considerably. Farther, the C 1s level was not observed after AHA treatment for 30 minutes. This indicates that the C atoms on the Si surface were removed by the AHA treatment.

Figure 4 shows the wide range of XPS spectra of a Cu sample before the AHA treatment and after the AHA treatment for 60 minutes. Before AHA treatment, several peaks originating from the C, Cu and O atoms were observed in the photoelectron spectrum. The peaks at ~1000, ~930, ~530, ~400, ~340, and ~290 eV are assigned to Auger levels by C KVV decay process, Cu 2p level, Auger levels by O KLL decay process, the O 1s level, Auger levels by Cu LMM decay process, C 1s levels, respectively. The intensity of the Cu 2p level was smaller than that of the O 1s and C 1s levels. After the AHA treatment for 60 minutes, the intensity of the O 1s and C 1s levels was decreased drastically and the intensity of the Cu 2p level and Auger levels by Cu LMM decay process were clearly observed. Thus, in the case of the Cu sample, there is a possibility that both the C and O atoms are removed by the AHA treatment.

Since the AHA treatment apparatus was installed at the beamline BL-07B at NewSUBARU SR facility, the photoelectron spectroscopy experiments using SR were also possible. The useful range of emitted photons from 50 to 800 eV is covered. Using photons with this photon energy region, the surface sensitive photoelectron spectroscopy spectra can be obtained by choosing the appropriate photon energy. Therefore, it is possible to investigate the surface reaction between atomic hydrogen and the solid surface at various materials at photoelectron spectroscopy using SR.

References

[1] A. Heya, A. Masuda, and H. Matsumura: Appl. Phys. Lett. **74**, 2143, (1999).
[2] K. Uchida, S. Hashioka, A. Izumi, and H. Matsumura: 2000 Dry Process Symp., 2000, p. 231.
[3] A. Izumi and H. Matsumura: Jpn. J. Appl. Phys. **41**, 4639, (2002).
[4] A. Heya and N. Matsuo: Jpn. J. Appl. Phys. **46**, 3545, (2007).
[5] C. D. Wagner, W. M. Riggs, L. E. Davis, J. F. Moulder and G. E. Muilenberg: Handbook of X-ray photoelectron spectroscopy, ed. G. E. Muilenberg (Perkin-Elmer, Eden Prairie, Minnesota, 1978).

XAS, PES and PEEM of bulk insulating materials using graphene

Satoru Suzuki[1], Yuichi Haruyama[1], Akinobu Yamaguchi[1], Tomoki Yamamoto[2], Takuya Yoshizumi[2], Ayaka Fujii[2], Seiji Nakashima[3], Yakumo Fuchiwaki[3], Hironori Fujisawa[3], Takuo Ohkochi[4], Mari Ishihara[5], Hirosuke Sumida[6]
[1]LASTI, Univ. of Hyogo, [2]Graduate School of Science, Univ. of Hyogo, [3]Graduate School of Engineering, Univ. of Hyogo, [4]JASRI, [5]Hyogo Prefectural Institute of Technology, [6]Mazda Motor Corp.

Abstract

PES and XAS of an insulating material are often disturbed by the charging effect. Here, monolayer graphene was used as a conductive layer to prevent the charging effect of insulating substrates. Charging-free spectra were obtained with various photon energies ranging from VUV light to hard X-rays. This method could also be applied to PEEM of an insulating film. Photoelectron transmissivities for the transferred graphene film were evaluated over a wide kinetic energy range from ~30 to 8000 eV. A minimum transmissivity of ~0.1 was found at a kinetic energy of ~60 eV, which rose to 0.86 at 7910 eV. In terms of the kinetic energy dependence of the transmissivity, this method is especially suitable for conventional XPS and HAXPES.

Introduction

One major disadvantage of PES is that it is often difficult to properly obtain a spectrum from a bulk insulating material because of the charging effect. Similarly, XAS of a bulk insulating material is also difficult, when the absorption intensity is measured using the total electron yield (TEY) or partial electron yield method.

In this report, XAS and PES were obtained from bulk insulating materials coated with monolayer graphene.[1] We also evaluated the photoelectron transmissivity for the transferred graphene at electron kinetic energies of 29 to 7910 eV.[1] The photoelectron transmissivity is sufficiently large at kinetic energies used in conventional XPS and HAXPES.

Experiments

A glass slide (thickness: 1 mm) and a $LiNbO_3$ wafer (0.5 mm) were used as typical insulating samples; a $BiFeO_3$ film (300 nm), grown by radio frequency magnetron sputtering on a $SrRuO_3$-buffered (30 nm) $SrTiO_3$ (0.5 mm) substrate;[2] and a 1-mm-thick commercial two-part (epoxy resin and polyamide amine) epoxy adhesive. A graphene film was transferred onto the glass, $LiNbO_3$, and $BiFeO_3$ samples, using graphene grown on Cu foil by the CVD method and the commonly used wet transfer process.[3] For the epoxy adhesive sample, the graphene face of graphene/Cu was adhered to the epoxy adhesive. After the epoxy adhesive cured, the Cu foil was etched in $FeCl_3$ solution followed by rinsing in pure water.

Conventional XPS and synchrotron radiation soft X-ray PES and XAS measurements were

Fig 1. (a) Si-*L* absorption spectra of a glass slide with and without graphene. (b) O-*K* absorption spectra of a glass slide with and without graphene.

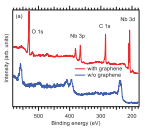

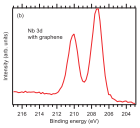

Fig 2. (a) Wide-range and (b) Nb 3*d* XPS (Al *K*α source) of a $LiNbO_3$ wafer with and without graphene.

conducted at the BL-7B beamline in NewSUBARU, The TEY mode was used for XAS measurements. For conventional XPS, an Al *K*α source ($h\nu$=1486.6 eV) was used. HAXPES was performed at the BL24XU undulator beamline in SPring-8. The excitation photon energy was set to 8 keV. PEEM measurements were conducted in a PEEM apparatus (LEEM III, ELMITEC GmbH) at the BL17SU beamline in SPring-8. All the XAS, PES, and PEEM measurements were performed by illuminating the center of the insulating samples.

Results and Discussion

Si-*L* absorption spectra of the glass substrates with and without graphene are shown in Fig. 1(a). From the glass plate without graphene, the TEY intensity is very weak and the spectral shape is very different from those observed from SiO_2 powder or thin film. [4] These changes are considered to be due to the charging effect. However, the spectrum from the glass with graphene is characteristic of SiO_2. The absorption peaks at 106.2 and 106.8 eV are assigned to a transition to a Si 3*s*-like state from $2p_{3/2}$ and $2p_{1/2}$, respectively. The graphene film coating also produced significant improvement of the spectral intensity in the O-*K* spectrum, as shown in Fig. 1(b). The spectrum from the glass with graphene is similar to those previously reported.[5]

Figure 2(a) shows the XPS of $LiNbO_3$ with and without graphene obtained using an Al *K*α source. Even without graphene, we could detect some photoelectron signals from $LiNbO_3$. This is probably because secondary electrons emitted from the Al

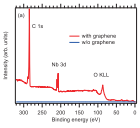

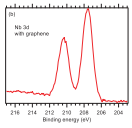

Fig 3. (a) Wide-range and (b) Nb 3*d* photoemission spectra of a $LiNbO_3$ wafer with and without graphene obtained at $h\nu$ = 600 eV.

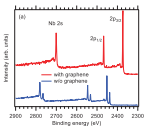

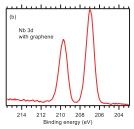

Fig 4. (a) Wide-range and (b) Nb 3*d* photoemission spectra of a $LiNbO_3$ wafer with and without graphene obtained at $h\nu$ = 8000 eV.

window of the X-ray tube irradiate the sample surface and partly neutralize the charging.[6] However, the peaks are upshifted by about 30 eV by the charging effect. The peaks are also relatively broadened without graphene, which suggests that the sample surface is inhomogeneously charged. Conversely, this binding energy shift is not observed for $LiNbO_3$ with graphene. The spectral shape of Nb 3*d* orbitals is also very close to those previously reported,[7] as shown in Fig. 2(b). We thus conclude that no apparent charging effect is observed.

In this study, the charging effect was most strongly observed for soft X-ray PES, as shown in Fig. 3(a). $LiNbO_3$ without graphene exhibited almost no spectral intensity, whereas the charging problem was clearly resolved for $LiNbO_3$ with graphene. Again, the spectrum of Nb 3*d*, shown with higher resolution in Fig. 3(b), is almost identical to those previously reported. One important issue here is the significant attenuation of photoelectron intensity from the $LiNbO_3$ substrate. Although the spectral intensity from the topmost graphene is large, the intensity from the $LiNbO_3$ substrate is relatively weak. Because soft X-ray PES is highly surface sensitive, the scattering of photoelectrons by monolayer graphene film is quite serious, which we will later discuss in greater detail.

In contrast to soft X-ray PES, attenuation of photoelectron intensity was no longer serious in HAXPES. The photoemission spectra of $LiNbO_3$ with and without graphene obtained at $h\nu$ = 8 keV are shown in Fig. 4(a). The spectrum from $LiNbO_3$ without graphene is upshifted by approximately 40 eV, with each peak split into two because of inhomogeneous charging. However, a charging-free spectrum was obtained from the graphene-covered $LiNbO_3$, including for the Nb 3*d* spectrum shown in Fig. 4(b). Additionally, the intensity of the C 1s peak from graphene is no longer prominent as it was for soft X-ray PES.

This approach can also be used to analyze soft materials like adhesives. Fig. 5(a) shows HAXPES spectra obtained from epoxy adhesive samples with and without graphene. Although we measured

Fig 5. (a) Wide-range and (b) C 1*s* photoemission spectra of an epoxy adhesive with and without graphene obtained at $h\nu = 8000$ eV. In (b), the curve fitting results are also shown.

practically no spectral intensity without graphene, the charging effect was counteracted by the graphene layer. The C and O (~533 eV) peaks are from both the epoxy resin and curing agent polyamide amine and the N peak (~400 eV) is from the polyamide amine. The C 1s spectrum of the epoxy adhesive was curve-fitted using three components (at approximately 284.8, 286.0 and 287.7 eV), as shown in Fig. 5 (b). These can be attributed to C-C, C-O, and C=O components, respectively.[8] The spectrum from the topmost graphene is considered to contribute to the C-C component. However, considering that the probing depth is 10 nm or larger in this measurement, the contribution from graphene should be small.

Finally, in Fig. 6, we show X-ray linear dichroism (XLD) images of the graphene-covered $BiFeO_3$ film grown on a vicinal $SrTiO_3$ (001) substrate obtained by PEEM measurements. In the Fe-L_2 absorption spectrum of $BiFeO_3$, we observed double-peak structures at about 720.8 and 722.3 eV. The images were obtained by dividing the PEEM image obtained at 722.3 eV by the image at 720.8 eV. Stripes are observed in Fig. 6(a) when the direction of the X-ray polarization ***E*** is parallel to the <010> direction of the $SrTiO_3$ substrate, but were not observed in Fig. 6 (b) where the sample is rotated by 45°. The characteristic XLD contrast observed at ***E***//<010> is caused by both antiferromagnetic and ferroelectric ordering.[9] Yellow-dashed lines in Fig. 8(a) show boundaries between domains showing different XLD image contrasts, corresponding to 71° domain walls (DWs) at which spontaneous polarization vectors rotate by

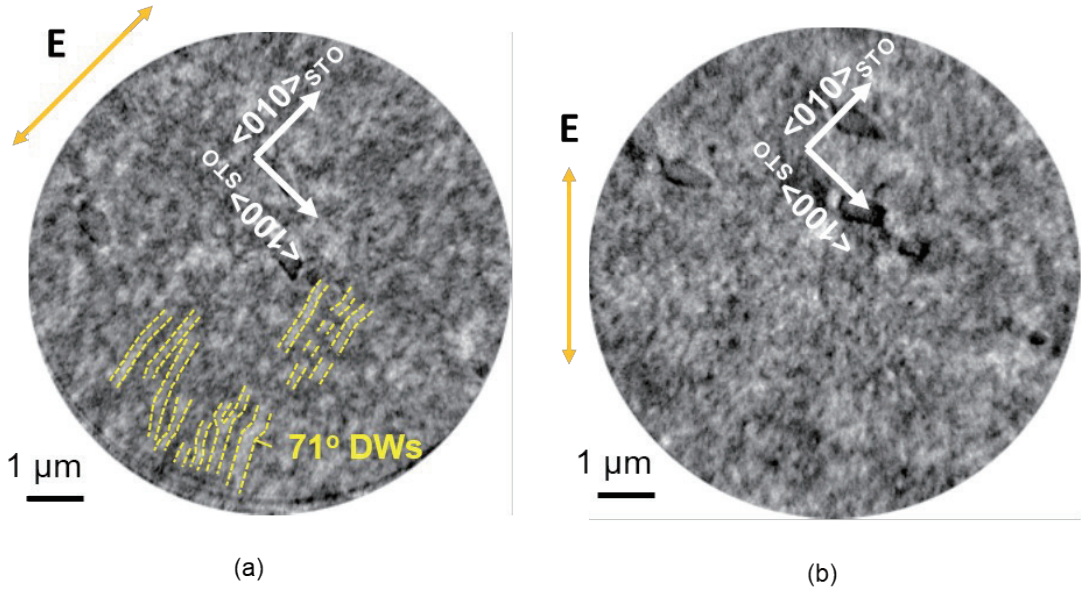

Fig 6. Fe-L_2 XLD images of a $BiFeO_3$ film obtained at two X-ray polarization directions, ***E***: (a) ***E***//<010> and (b) ***E***//<110>. In (a), some 71° DWs caused by striped antiferromagnetic/ferroelectric domain structure are denoted by yellow-dashed lines.

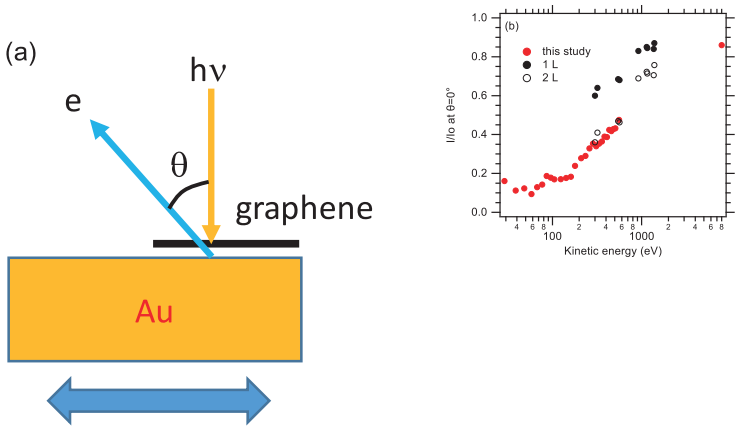

Fig 7. (a) Schematic of transmissivity measurements of photoelectrons for the graphene film. (b) Photoelectron transmissivity at $\theta = 0°$ at various kinetic energies. The data of as-grown graphene reported by Kraus et al. also shown (1L). The data for 2L was obtained by squaring the values of 1L.

approximately 71°. This observation is only possible thanks to the fully compensated surface potential with the graphene top layer.

We evaluated the attenuation of photoelectron intensity caused by graphene films and its kinetic energy dependence by measuring Au $4f_{7/2}$ photoelectron intensities from a graphene-covered and uncovered part of a Au plate, as shown in Fig. 7(a). We measured I/Io, where, Io and I stand for photoelectron intensities from the Au plate without and with graphene, respectively, at $\theta = 45°$ ($\theta = 2°$ for kinetic energy of 7910 eV). We obtained putative I/Io values expected at $\theta = 0°$, assuming $I/Io = \exp(-d/\lambda\cos\theta)$, where d is the effective thickness of graphene, λ is the inelastic mean free path (IMFP), and θ is the photoelectron emission angle from the sample normal. Fig. 7(b) shows I/Io at $\theta = 0°$ at various kinetic energies. As expected from the universal curve of IMFP,[10] I/Io reaches its minimum of ~0.1 at a kinetic energy of ~60 eV. With increasing kinetic energy, I/Io increases and reaches 0.5 at ~500 eV and at 7910 eV, I/Io is about 0.86. From this result, this method can be considered especially suitable for conventional XPS and HAXPES.

We also estimated the effective thickness of the graphene film. In Fig. 7(b), the data denoted by solid black circles (1L) were obtained from a previous μ-probe PES by Kraus et al.,[11] in which CVD-grown monolayer graphene on Cu was used as a sample. The open circles (2L) were obtained by squaring the data of the solid black circles, and they correspond to I/Io for double-layer graphene. The I/Io data obtained in this study is smaller than that of 1L, but, is close to 2L. This means that the effective thickness of our transferred monolayer graphene is closer to 2L rather than 1L. We think that the increase of the effective thickness is due to contamination above and below the graphene film, which is very hard to fully eliminate.[8]

Acknowledgments

PEEM measurements were performed at the beamline BL17SU at SPring-8 (proposal no. 2019A1311). HAXPES measurements were performed at the beamline BL24XU at SPring-8 (proposal no. 2019A3231 and 2019B3231).

References

1. S. Suzuki, et al., J. Appl. Phys. **128** (1), 015304 (2020).
2. S. Nakashima, et al., Appl. Phys. Lett. **111** (8), 082907 (2017).
3. J. W. Suk, et al., ACS Nano **5** (9), 6916 (2011).
4. D. Li, et al., American Mineralogist **79**, 622 (1994).
5. Y. Muramatsu, et al., Adv. X-Ray Chem. Anal. **48**, 317 (2017).
6. L. Edwards, et al., Surface and Interface Analysis **51** (9), 925 (2019).
7. R. J. Iwanowski, et al., Journal of Alloys and Compounds **286** (1), 162 (1999).
8. S. Suzuki, et al., The Journal of Physical Chemistry C **117** (42), 22123 (2013).
9. T. Zhao, et al., Nature Materials **5** (10), 823 (2006).
10. M. P. Seah, et al., Surface and Interface Analysis **1** (1), 2 (1979).
11. J. Kraus, et al., Nanoscale **6** (23), 14394 (2014).

Hard X-ray photoelectron spectroscopy of insulating catalyst samples using graphene

Ayaka Fujii[1], Hirosuke Sumida[2], Satoru Suzuki[3]
[1]School of Science, University of Hyogo, [2]Mazda Motor Corp., [3]LASTI, University of Hyogo

Abstract

Graphene is a one-atom-thick layered material consisting of carbon atoms having high conductivity. It is thought that its high conductivity may prevent the charging effect in photoelectron spectroscopy. In this study, we attempted the photoelectron spectroscopy of an insulating sample which graphene was transferred to. In the experiment, we examined the transfer method of graphene to the substrate surface of CeO_2, which is an insulating catalyst sample, and performed photoelectron spectroscopy of the sample by a Near Ambient Pressure HArd X-ray PhotoEmission Spectroscopy (NAP-HAXPES). As a result, the sample treated with oxygen plasma on the substrate surface showed less damage to graphene, and the photoelectron spectrum of the insulating sample supporting graphene was obtained. Therefore, by performing surface treatment on the substrate surface before the transfer of graphene, the transfer accuracy of graphene can be improved, and by supporting graphene, it was possible to perform photoelectron spectroscopic measurement of insulating samples that cannot be usually measured.

Introduction

At present, in the automobile industry, in order to reduce the environmental load and health risks, further improvement of the performance of exhaust gas purification catalysts is an extremely important issue.[1] We have installed a semi-atmospheric pressure hard X-ray photoelectron spectrometer at BL24XU, the ID beamline of Hyogo Prefecture at SPring-8, and are aiming to realize reaction analysis under conditions close to the actual environment of exhaust gas purification catalyst. Generally, an exhaust gas purification catalyst has a structure in which catalytic metal fine particles are supported on an insulating cocatalyst such as CeO_2.[2] However, due to the charging effect of the insulating promoter, it has been difficult to analyze exhaust gas purification catalysts by photoelectron spectroscopy. In this study, therefore, we attempted to transfer graphene to an insulating sample and measure its photoelectron spectroscopy. Graphene is a sheet of carbon atoms with a thickness of 1 atom,[3] and it is possible to minimize the attenuation of photoelectron intensity. It also has sufficiently high electrical conductivity to prevent the charging effect.[4]

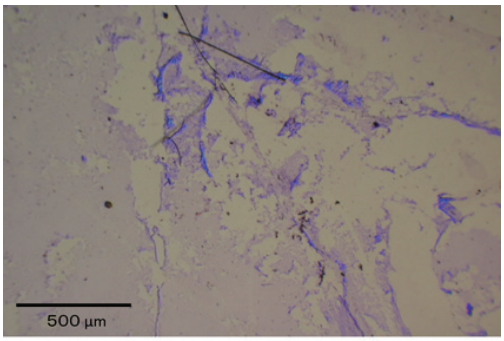

Fig. 1. Optical microscope image of graphene transferred to insulating catalyst CeO_2 without oxygen plasma treatment.

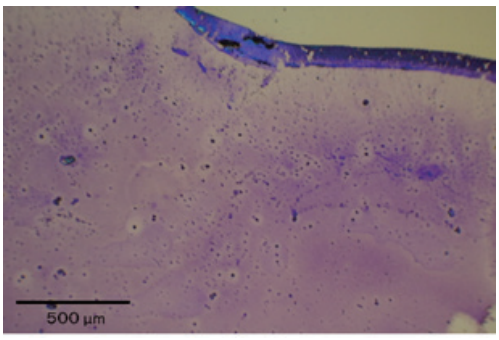

Fig. 2. Optical microscope image of graphene transferred to insulating catalyst CeO_2 with oxygen plasma treatment.

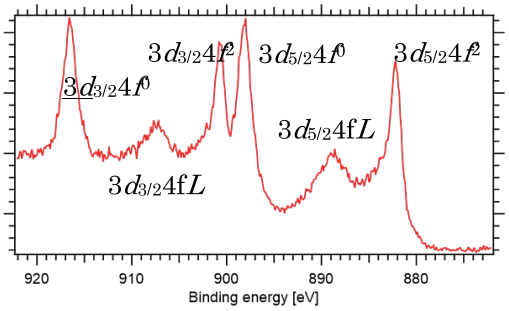

Fig. 3. Ce 3*d* photoelectron spectrum of CeO_2

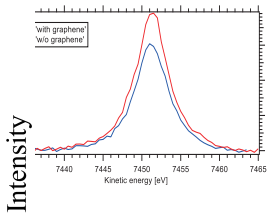

Kinetic energy [eV]

Fig.4. Au $4p_{3/2}$ spectra for photoelectron intensity measurement using Au sample.

Experiments

In this study, we investigated the effect of substrate surface treatment when transferring graphene onto CeO_2 powder, an insulating catalyst material. In addition, we performed photoelectron spectroscopic measurement of CeO_2 which graphene was transferred to. For the transfer of graphene, we used the underwater transfer method that is generally used to fabricate graphene devices.[5]

Hard X-ray photoemission spectroscopy was performed at BL24XU beamline in SPring-8. The excitation photon energy was set to 8 keV.

Results and Discussion

When graphene was transferred to the catalyst material without surface treatment, the graphene peeled off and fractured as shown in Fig. 1. Then, we performed oxygen plasma treatment on the substrate surface before transfer. As a result, it was found that exfoliation and breakage of graphene were significiently suppressed as shown in Fig. 2. Fig. 3 shows a Ce 3*d* spectrum obtained by a hard X-ray photoelectron spectroscopy measurement. In Fig. 3, the $\underline{3d_{3/2}}4f^0$, $\underline{3d_{3/2}}4f^2\underline{L}^2$, and $\underline{3d_{5/2}}4f^0$ peak are observed at near 917 eV, 901 eV, and 898 eV, respectively. These values are almost the same as those in previous report ,[6] . Therefore, we conclude that the Ce3*d* spectrum of this sample had no charging effect. From these results, it was found that the photoelectron spectroscopy of the insulating cocatalyst sample can be measured by transferring graphene.

Next, we examined the transmittance of photoelectrons. As shown in Fig. 4, the transmittance was measured by measuring the Au photoelectron intensity of the Au sample partly supporting graphene and partly unsupporting graphene. Fig. 5 shows the photoelectron transmittance at various kinetic energy. The black dots in Fig. 5 are the transmittances obtained by our research group so far,[7] and the red dots are the transmittances obtained in this experiment. From Fig. 5, it can be seen that the transmittance around tens of eV is only 10 %, but the transmittance observed this HAXPES measurement reaches about 70 % or larger. Therefore, we can conclude that X-ray photoelectron spectroscopy using graphene is effective on the high kinetic energy side obtained in HAXPES measurements.

We now discuss the cause of the reduced transfer damage caused by oxygen plasma treatment. When we measured the contact angle after the oxygen plasma treatment, it was confirmed that the substrate surface became very hydrophilic. Therefore, it is considered that the water molecules existing at the interface between CeO_2 and graphene act as an adhesive agent, and the adhesion of graphene is greatly improved.

Acknowledgments

HAXPES measurements were performed at the beamline BL24XU at SPring-8 (proposal no. 2019A3231 and 2019B3231).

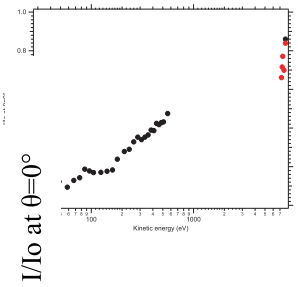

Kinetic energy [eV]

Fig. 5. Photoelectron transmittance derived from Au photoelectron intensity measurements.

References

[1] A. Takami, J. Combust. Soc. Jpn **52**, 198 (2010).
[2] CATALER Corporation, HP. https://www.cataler.co.jp/product/car.php
[3] K. S. Novoselov, A. K. Geim, S. V. Morozov, D. Jiang, Y. Zhang, S. V. Dubonos, I. V. Grigorieva, and A. A. Firsov, Science, **306**, 666 (2004).
[4] S. Bae, H. Kim, Y. Lee, X. Xu, J. S. Park, Y. Zheng, J. Balakrishnan, T. Lei, H. R. Kim, Y. I. Song, Y. J. Kim, K. S. Kim, B. Ozyilmaz, J. H. Ahn, B. H. Hong and S. Iijima, Nat Nanotechnol **5**, 574-578 (2010).
[5] W. Regan, N. Alem, B. Alemán, B. Geng, Ç. Girit, L. Maserati, F. Wang, M. Crommie and A. Zettl, Appl. Phys. Lett. **96**, 113102 (2010).
[6] A. Kotani, Synchrotron radiation, **8**, No.5(1995).
[7] S. Suzuki, Y. Haruyama, A. Yamaguchi, T. Yamamoto, T. Yoshizumi, A. Fujii, S. Nakashima, Y. Fuchiwaki, H. Fujisawa, T. Ohkochi, M. Ishihara, H. Sumida, J. Appl. Phys. 128, 015304 (2020).

Development of soft X-ray absorption spectrometer at atmospheric pressure using He-path with a free-standing membrane as a partition wall

Masahito Niibe[1], Yuka Horikawa[2], and Takashi Tokushima[3]
[1]LASTI, Univ. Hyogo, [2]Yamaguchi Univ., [3]Lund Univ.

Abstract

We have developed a new soft X-ray absorption spectroscopic equipment that can easily and inexpensively measure volatile substances and liquids under atmospheric pressure. This apparatus uses a thin SiN free-standing membrane with a thickness of 100 nm as a pressure partition wall, and puts the sample in a container filled with He gas. Using this apparatus, it is possible to measure soft X-ray absorption spectra of free surface of samples by total electron yield (TEY) and total fluorescence yield (TFY) methods. We measured soft X-ray absorption spectra at the O-K, C-K, and Ti-L-edge under atmospheric pressure for standard solid samples.

Introduction

With the development of fuel cells and next-generation semiconductor devices, the effectiveness of operando spectroscopic measurement under atmospheric pressure has been recognized, but soft X-ray spectroscopic analysis of light elements such as oxygen, nitrogen, and carbon in atmospheric pressure has been difficult until now. There is an increasing demand for a device that can operate under atmospheric pressure. The He path using a multi-stage differential pumping system has been used for soft X-ray absorption spectroscopy under atmospheric pressure with a photon energy of 1 keV or less [1]. However, the multi-stage differential evacuation system has problems that it is expensive to install and consumes a large amount of He. We have newly developed a He path equipment using a 100-nm-thick SiN membrane as a pressure partition wall to measure soft X-ray absorption of liquids and volatile substances at atmospheric pressure more inexpensively and easily. We have also succeeded in measuring soft X-ray absorption spectra at the K-edge of oxygen at atmospheric pressure using this equipment at the NewSUBARU synchrotron radiation (SR) facility [2].

Development of He-path equipment

Figure 1 shows a schematic diagram of the developed He-path equipment. A soft X-ray introduction pipe and a He inlet/outlet pipe are passed through an aluminum die-cast airtight container, and a sample holder and a photodiode for soft X-ray detection are fixed inside. A SiN membrane window having a window size of 0.5×0.5 mm and a thickness of 100 nm was bonded to the end surface of the soft X-ray introduction pipe to form a pressure partition wall for high vacuum. An oxygen concentration monitor was attached to the outlet side of the He channel to confirm that the inside of the closed container was replaced with He. The oxygen concentration in the atmosphere inside the container could be reduced to about 0.01% by performing He substitution for about 30 min at a flow rate of 200 cc/min. The soft X-ray absorption can be detected by the total fluorescence yield (TFY) method using a photodiode and the total electron yield (TEY) method using a drain current measurement. In the TEY method, a bias voltage using a dry battery may be applied in order to facilitate electron emission.

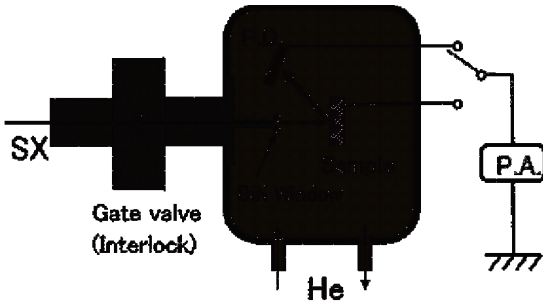

Fig. 1 Schematic diagram of the He-path equipment installed in BL-09A at the NewSUBARU SR facility.

This equipment was attached to the end station of the monochromator beamline BL-09A at the NewSUBARU SR Facility for soft X-ray absorption spectroscopy. An interlock device consisting of an ionization vacuum gauge and an ICF-70 gate-valve was created to maintain the vacuum of the beamline when the SiN window was damaged by some reason. Actually, while doing the sample setting work, there was an accident in which the hair of the fingers touched the window and the SiN window was broken. At this time, the interlock device worked fine and had almost no effect on the upstream of the

beamline.

Measurement of soft X-ray absorption spectra

In order to confirm the reliability of the spectrum measured by this equipment, we first analyzed the soft X-ray absorption spectrum of titanium oxide (rutile and anatase), which is a solid sample often measured in vacuum, using the He-path equipment. Figure 2 shows the absorption spectra of the Ti-L and O-K absorption edges measured by the TEY method in comparison with those measured in vacuum. Here, in the TEY method, a negative bias of about -5 V was applied to the sample side for measurement. From these graphs, it was found that the soft X-ray absorption spectra under the atmospheric pressure He were almost the same as those measured in vacuum in both the TEY method and the TFY method.

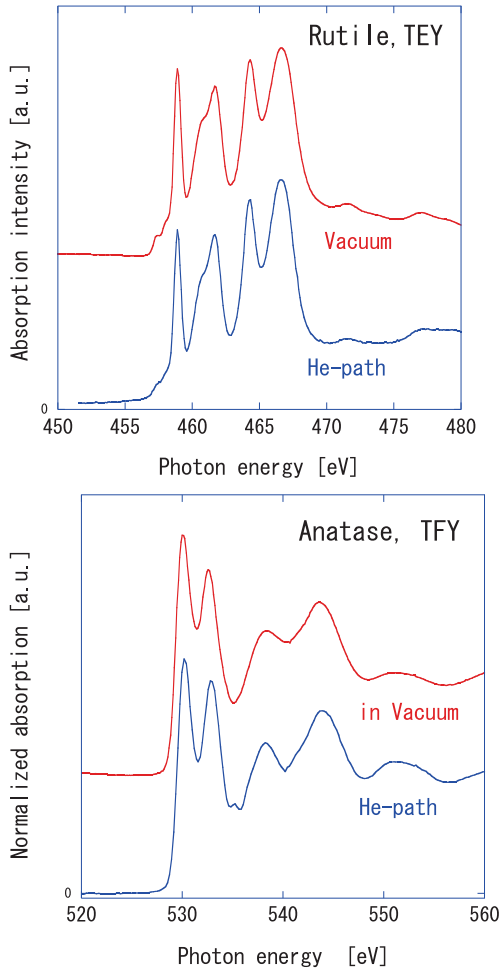

Fig. 2 Ti L-edge and O K-edge absorption spectra of TiO_2 powder standard samples.

Figure 3 shows a soft X-ray absorption spectra at the O-K edge of benzoic acid. Since benzoic acid has a vapor pressure of about 0.1 Pa at 25°C, it is usually impossible to measure the soft X-ray absorption by placing the sample in a high vacuum chamber. With regard to such a sample, it has become possible to measure absorption by using an atmospheric pressure He-path equipment.

When measuring the O-K absorption spectrum of water, it was found that water vaporized severely in an atmosphere in which the atmosphere was replaced with only He, and water was lost during the measurement. In order to deal with this, it was found that the evaporation of water can be suppressed by replacing the atmosphere with "wet" He gas that has been bubbled in water beforehand. In the future, we plan to try soft X-ray absorption measurement of aqueous solutions, ionic liquids, organic solvents, various oils, solar cell materials containing organic substances with high vapor pressure, and fuel cells. In addition, we plan to deal with nitrogen absorption measurement by replacing the SiN window material with SiC.

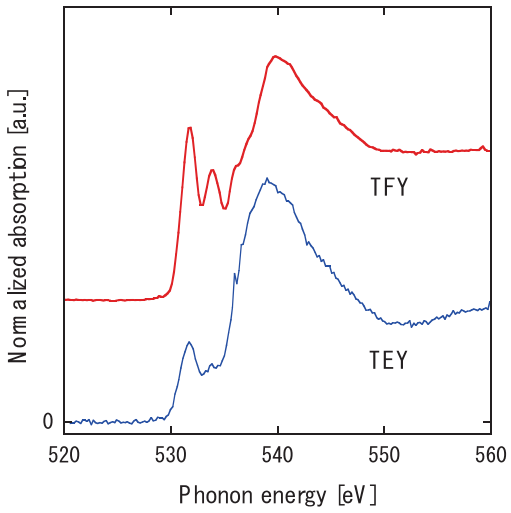

Fig. 3 O K-edge absorption spectra of benzoic acid powder measured by TEY and TFY methods.

References

[1] Y. Tamenori, J. Synchrotron Rad. **17**, 243-249 (2010).
[2] M. Niibe, Y. Horikawa and T. Tokushima, Adv. X-Ray. Chem. Anal., Japan **51**, pp.41-48 (2020).

Soft X-ray absorption spectra of sugar

Kyoka Maee and Yasuji Muramatsu
Graduate School of Engineering, University of Hyogo

Abstract

X-ray absorption near-edge structure (XANES) spectra of various kinds of sugar were measured in BL10/NewSUBARU to clarify the unstable melting point of sugar. Characteristic XANES profiles, which were dependent on the kind of sugar, can be observed in both C *K* and O *K* regions. XANES profile changes before and after grinding of sugar particles were also observed in C *K*- and O *K*-XANES. Such differences in XANES profiles may be caused by intermolecular effects such as hydrogen bonding.

1. Introduction

Sugar consisting of sucrose ($C_{12}H_{22}O_{11}$) crystals is highly pure material. In general, pure materials have steady melting point (m.p.). However, m.p. of sugar often differs from the sugar manufacturing process, purification process, and its particle shape/size. Such unstable m.p. affects food and/or cooking using sugar.

The unstable m.p. of sugar may result from crystal structure differences or chemical bonding states including hydrogen bond. However, crystal structure analysis by the X-ray diffraction (XRD) method has not clarified the unstable m.p. For chemical state analysis, X-ray absorption near-edge structure (XANES) using synchrotron radiation (SR) has been a powerful tool. Hence, in the present study, we have measured XANES of various sugar samples to clarify their unstable m.p.

2. Experiments

Sugar samples (hard sugar, granulated sugar, and powder sugar) were commercially prepared. Table 1 shows the specifications of sugar samples. The samples were labelled as GAl (m.p. 180 °C~), GB1~GB5 (170~180°C), GC1 (160~170°C), GD1~GD3 (150~160°C), and GE1~GE2 (140~150°C), depending on m.p. Samples of GB1, GB4, GD1, and GD3 were also ground to fine powders, which are labelled as GB1-P, GB4-P, GD1-P, and GD3-P, respectively.

Table 1 Specifications of sugar samples.

Label	m.p. range / °C	m.p. / °C	Weight per 50 grains / mg	Specific rotation [α]20D / degree	Sugar content / °Z
GA1	180~	180.9	5.3	66.09	99.25
GB1	170~180	179.7	6.5	65.84	98.87
GB2		176.7	5.5	66.26	99.50
GB3		174.7	8.0	66.27	99.53
GB4		174.5	6.3	66.51	99.88
GB5		173.6	4.2	66.28	99.53
GC1	160~170	167.8	3.6	66.11	99.29
GD1	150~160	158.6	6.6	66.86	100.4
GD2		156.9	2.9	65.68	98.64
GD3		154.6	4.3	65.93	99.01
GE1	140~150	143.8	6.4	65.25	97.99
GE2		141.8	9.9	65.61	98.53

Figure 1 shows a sample plate for XANES measurements. Granulated sugar and powder sugar samples were pressed and held on 0.3-mm thick indium (In) substrates which were stuck on a copper (Cu) plate using double-sticky conductive carbon (C) tapes. XANES measurements in the C *K* and O *K* regions of the sugar samples were performed in BL10/NewSUBARU and BL-6.3.2/ALS using a total-electron-yield (TEY) method. Sample current of the sugar samples were measured through the C-tape/Cu-plate during SR beam irradiation.

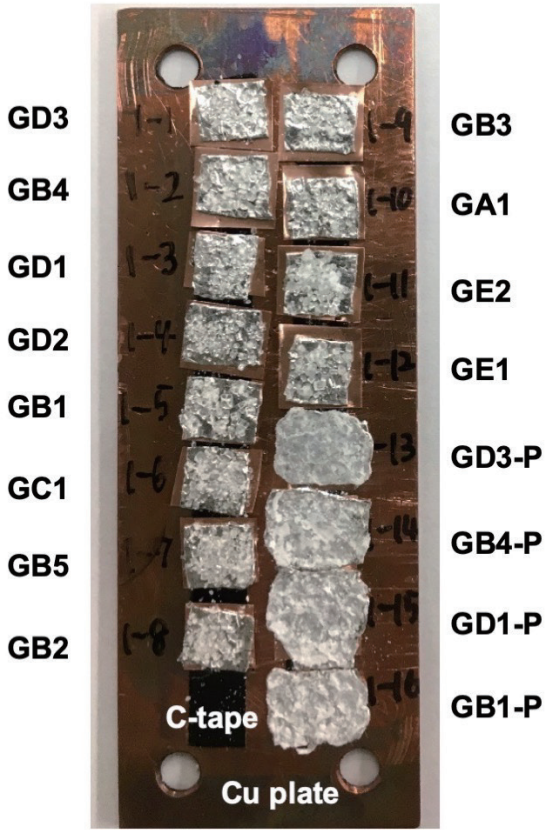

Fig. 1 Photo of the sugar samples put on a basal Cu plate.

3. Results and Discussion

(1) XANES profiles

Figure 2 shows C *K*-XANES and differential spectra of granular sugar samples, which were measured in BL10/NewSUBARU. Each sample exhibits the characteristic broad peaks at 288 eV (denoted as *a*) and 289.5 eV (*b*). To quantitatively evaluate the peak intensity of *a* and *b*, differential spectra (denoted as Diff. in the Figure) were drawn on XANES. The differential spectra clearly shows the peaks *a′* and *b′* which correspond to peaks *a* and *b* in XANES. Hence, peak heights of *a′* and *b′* reflect peak intensities of *a* and *b*, respectively. The peak height ratio of *a*'/*b*' seems to be dependent on the samples.

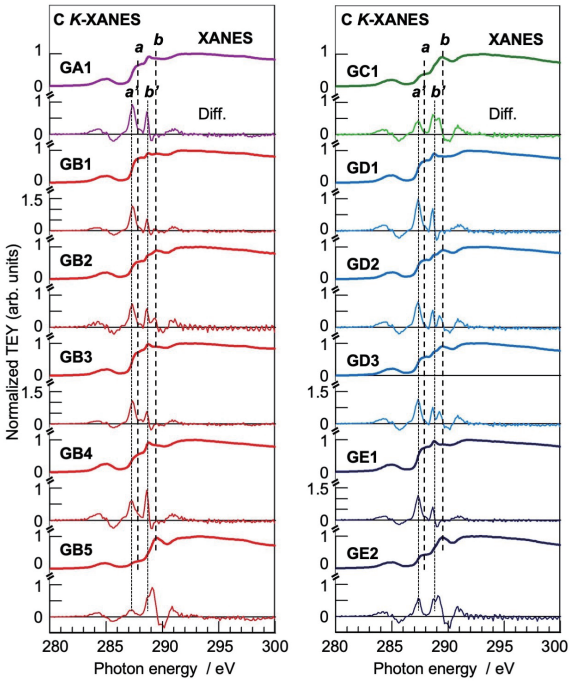

Fig. 2 C *K*-XANES (bold lines) and differential spectra (fine lines) of granulated sugar samples.

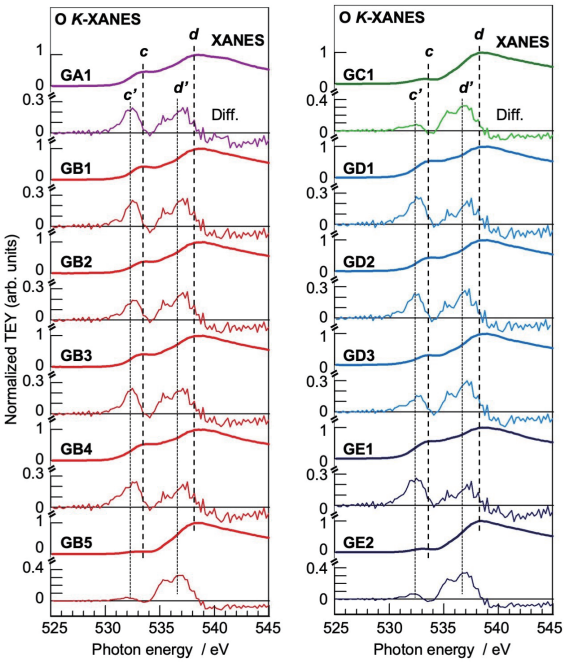

Fig. 3 O *K*-XANES (bold lines) and differential spectra (fine lines) of granulated sugar samples.

Figure 3 shows O *K*-XANES and differential spectra of granular sugar samples. Each sample exhibits the characteristic broad peaks at 534 eV (denoted as *c*) and 538.5 eV (*d*). The differential spectra clearly shows the peaks *c′* and *d′* which correspond to peaks *c* and *d* in XANES. Hence, peak heights of *c′* and *d′* reflect peak intensities of *c* and *d*, respectively. The peak height ratio of *c*'/*d*' seems to be dependent on the samples.

Figure 4 shows the relationship between the peak height ratios *a*'/*b*' and *c*'/*d*'. The approximated line of (*c′*/*d′*) = 0.426 x (*a′*/*b′*) + 0.194 shows that chemical states of carbon atoms reflecting peaks *a* and *b* correlate with those of oxygen atoms reflecting peaks *c* and *d*. Such the finding of the correlation between carbon and oxygen suggests the chemical state difference due to hydrogen bond in sucrose molecules.

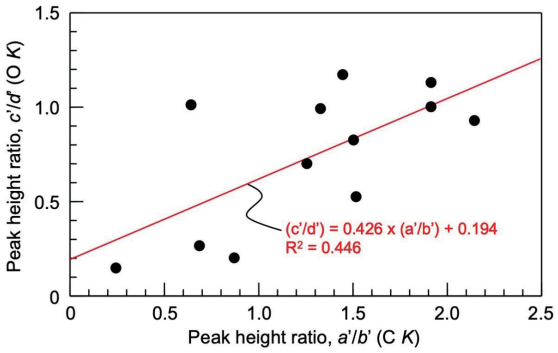

Fig. 4 Correlation between the differential peak height ratios of a'/b' in C *K* region and c'/d' in O *K* region.

(2) Effect of grinding

XANES and differential spectra in the C *K* and O *K* regions of granulated sugar before (a: GB1, GB4, GD1, and GD3) and after (b: GB1-P, GB4-P, GD1-P, and GD3-P) grinding are shown in Figure 5. In C *K* region, peaks *a*' and *b*' in Diff were clearly observed before grinding. However in after grinding, only peak *a*' disappeared. In O *K* region, peaks *c*' and *d*' in Diff were clearly observed before grinding. However, in after grinding, only peak *c*' disappeared. Such the findings mean that chemical states of both carbon and oxygen atoms depend on macroscopic structure of sucrose molecules, and peaks *a* and *c* are strongly correlated in some specific chemical states. It is considered that formation of hydrogen bond is also

dependent on the macroscopic structure. Hence, C *K*- and O *K*-XANES may observe the hydrogen bond in sugars, and the hydrogen bond states may affect the unstable m.p. of sugar.

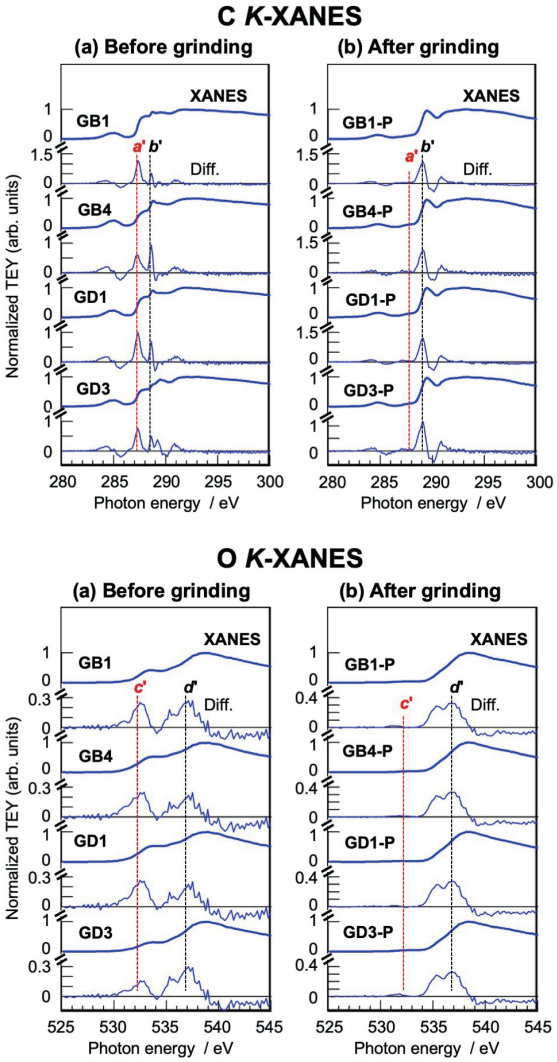

Fig. 5 XANES (bold lines) and differential spectra (fine lines) in the C *K* (upper panels) and O *K* (lower) regions of granulated sugar before (a) and after (b) grindings.

4. Conclusion

To clarify the unstable m.p. of sugar, XANES in the C *K* and O *K* regions of various sugar samples were measured in BL10/NewSUBARU. Characteristic peaks *a* and *b* in C *K*-XANES, and peaks *c* and *d* in O *K*-XANES correlated each other. The peaks *a* and *c* observed before grinding disappeared after grinding. These findings suggests that carbon and oxygen atoms are strongly correlated depending on macroscopic structure of sucrose molecules. Possible reason for the XANES profile changes is hydrogen bond formed among sucrose molecules.

To clarify the structure of sucrose molecules forming hydrogen bond, theoretical XANES analysis by using the first-principles calculations has been in progress.

Acknowledgements

We would like to express thanks to Professor Kaoru Sakamoto of University of Hyogo for her preparation of the sugar samples.

Reference

[1] K. Sakamoto, *et al.*, Food Sci. Technol. Res., 24, 111-118 (2018).

Total-electron-yield soft X-ray absorption measurements of non-volatile components in commercially-available drinks adsorbed on insulating wiping clothes

Runa Maruyama and Yasuji Muramatsu
Graduate School of Engineering, University of Hyogo

Abstract

To non-destructively detect contents of drinks, X-ray absorption spectra (XAS) of the contents adsorbed on insulating wiping clothes have been measured using a total-electron-yield (TEY) method. TEY-XAS measurements were performed in BL10 at the NewSUBARU. Protein and lipid contents in the drinks can be detected in C *K*- and O *K*-XANES. However, low-concentration contents or hydrocarbons cannot be easily detected in XANES. It is therefore concluded that such the contents in drinks adsorbed on wiping clothes can be non-destructively detected by using the TEY method.

1. Introduction

Monitoring the sample current during X-ray energy scanning is easy using X-ray absorption spectroscopy (XAS), which is a total electron yield (TEY) method. Although numerous XAS studies have used the TEY method to examine electrically conductive materials, it is difficult to apply to insulating bulk materials because sample charge-ups distort the TEY. To avoid or suppress charge-up effects of insulating bulk samples during X-ray irradiation, bulk samples are often powdered, and the powdered samples are placed on conductive substrates. This system effectively monitors the surface sample current of insulating particles, but it requires destructive preparations of bulk samples.

We recently found another method to easily observe the TEY of insulating samples. In our method, insulating organic film samples are placed on conductive substrates, and the sample current generated by soft X-ray irradiation can be efficiently detected through the backside of the substrate [1,2]. In further measurements for thicker samples such as papers, wiping clothes, and organic tapes, we have confirmed that the proposed TEY method would be a powerful tool to non-destructively measure XAS of bulk samples [3,4].

To apply the present TEY method for a novel analytical tool, we have measured TEY-XAS of non-volatile components in various drinks adsorbed on insulating wiping clothes [5].

2. Experiments

Table 1 shows specifications of the commercially available samples used in the present study. Wiping cloth of Kimwipe® (S-200, NIPPON PAPER CRECIA Co., Ltd.) was used for insulating adsorbent matrix (labelled as KW). The reason why we chose KW is that KW exhibit sufficiently high sample current during soft X-ray irradiation [4]. Drinks are mineral water (MW), green tea (GT), Hoji tea (HT), Coka-cola (CC), non-sugar Coka-cola (CC0), apple juice (AJ), orange juice (OJ), milk (ML), low-fat milk (ML0), sugar-free coffee (CF0), slightly-sugar-containing coffee (CF1), and sugar-containing sweet coffee (CF2). Such the drinks contain carbohydrates, proteins, and lipids.

Table 1 Specifications of the samples.

Label	Sample	Component
KW	Kimwipe®	Cellulose
MW	Mineral water	Na1.1mg, Ca0.71mg, K0.46mg, Mg0.55mg
GT	Green tea	Salt equivalent 0.02g, Catechin 80mg
HT	Hoji tea	Salt equivalent 0.03g
CC	Coca-cola	Carbohydrate 11.3g
CC0	Coca-cola0	Salt equivalent 0.01g
AJ	Apple juice	Protein 0.2g, Carbohydrate 21.7g, Salt equivalent 0-0.1g
OJ	Orange juice	Protein 1.3g, Lipid 0.2g, Carbohydrate 20.9g, Salt equivalent 0-0.1g
ML	Milk	Protein 6.8g, Lipid 7.8g, Carbohydrate 9.9g, Salt equivalent 0.22g, Ca 227mg
ML0	Low-fat milk	Protein 7.2g, Lipid 3.0g, Carbohydrate 9.9g, Ca 228mg, Na 85mg
CF0	sugar-free coffee	Carbohydrate 0.7g, Na 23mg
CF1	slightly-sugar-containing coffee	Protein 0.6g, Lipid 0.6g, Carbohydrate 3.2g, Na 49mg, Sugar 2.3g
CF2	sugar-containing sweet coffee	Protein 0.6g, Lipid 0.5g, Carbohydrate 6.9g, Na 53mg

Figure 1 shows the photo of sample plate. KW was cut into small pieces with the size of 5 mm x 5mm. The KW pieces were put on Cu plate with a conductive C-tapes. Each drink was dropped on the KW and dried in room temperature, which is denoted as (Drink-label)/KW. TEY-XAS measurements in the C *K* and O *K* regions were performed in BL10/NewSUBARU. Sample current of the samples was measured a picoammeter through the C-tape and Cu plate during the soft X-ray irradiation. Vacuum of the measurement

chamber during the measurements was 10^{-5} Pa. Hence, the samples were completely dried in the measurements.

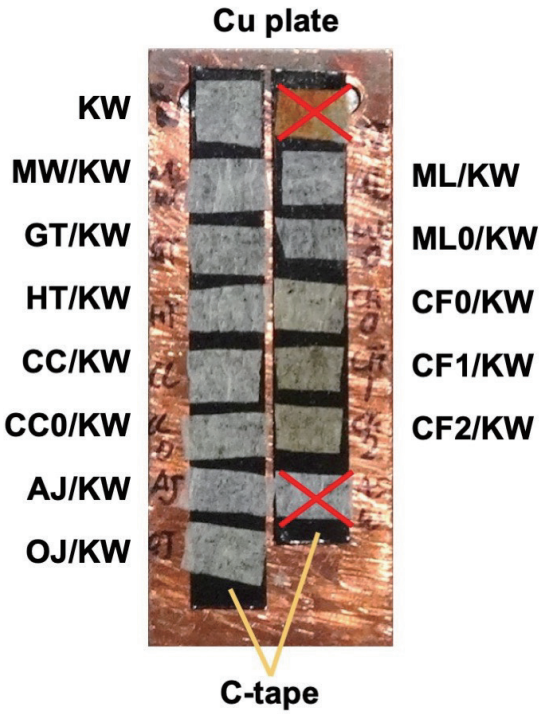

Fig. 1 Photo of the sample plate.

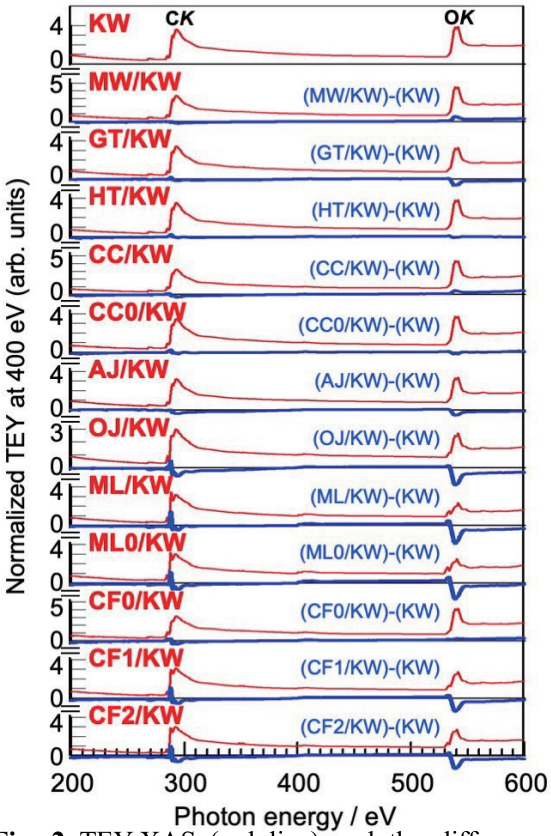

Fig. 2 TEY-XAS (red line) and the difference between Drink/KW and KW (blue) in the 200 ~ 600 eV region.

3. Results and Discssion

Figure 2 shows TEY-XAS and the difference between Drink/KW and KW in the 200 ~ 600 eV region. KW and Drink/KW clearly show C *K* and O *K* absorption peaks, which means sample current can be sufficiently observed in the insulating samples by soft X-ray irradiation. The difference spectra between Drink/KW and KW mean the non-volatile components of drinks adsorbed on KW. Thus, the larger spectral difference suggests the much amount components can be detected. From the square of the spectral difference in the region, which can be regarded as the index for the amount of adsorbed components, drinks of OJ, ML, ML0, CF1, and CF2 exhibit large spectral differences. These drinks have much proteins or lipids, which are not involved in cellulose. It is therefore confirmed that proteins and lipids of drinks on KW can be easily observed by the TEY method. On the other hand, drinks of CC, AJ, and CF0 whose main component is carbohydrate exhibit little spectral difference. This is reasonable because cellulose of KW is basically identified as carbohydrate. Drinks of MW, GT, HT, and CC0 have little proteins, lipids, and carbohydrates. Hence, these drinks also exhibit the quite little spectral differences.

Figure 3 shows the TEY C *K*-XANES and the spectral difference between Drink/KW and KW.

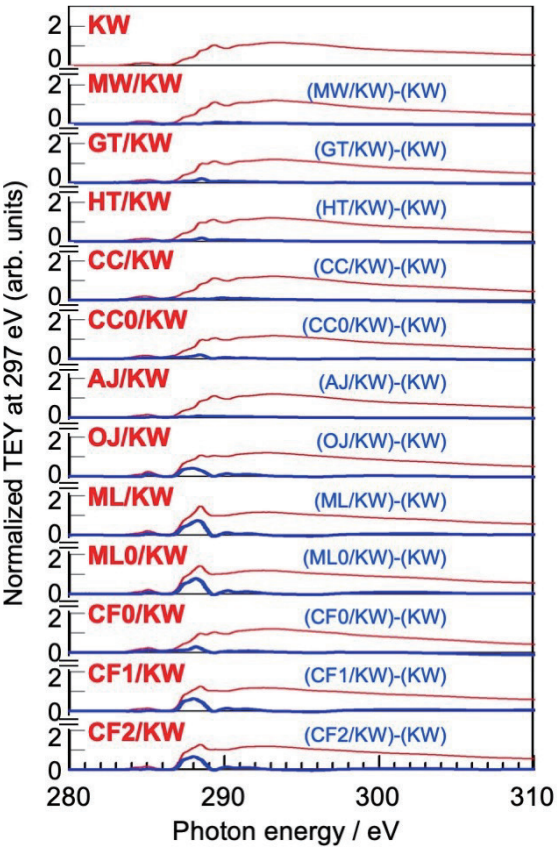

Fig. 3 TEY C *K*-XANES (red line) and the difference between Drink/KW and KW (blue).

Spectral differences can be clearly observed in 287~290 eV region and slightly observed around 285 eV of ML, ML0, CF1, and CF2. This means that amide structure (-CO-NH-) of proteins, ester structure (R-COO-R`) and long alkyl chains (-CH_2-) of lipids in these drinks can be identified in C *K*-XANES.

Figure 4 shows the TEY O *K*-XANES and the spectral difference between Drink/KW and KW. Spectral differences can be clearly observed around 534 eV of ML, ML0, CF1, and CF2. This means that carbonyl structure (>C=O) of proteins and lipids in these drinks can be identified in O *K*-XANES.

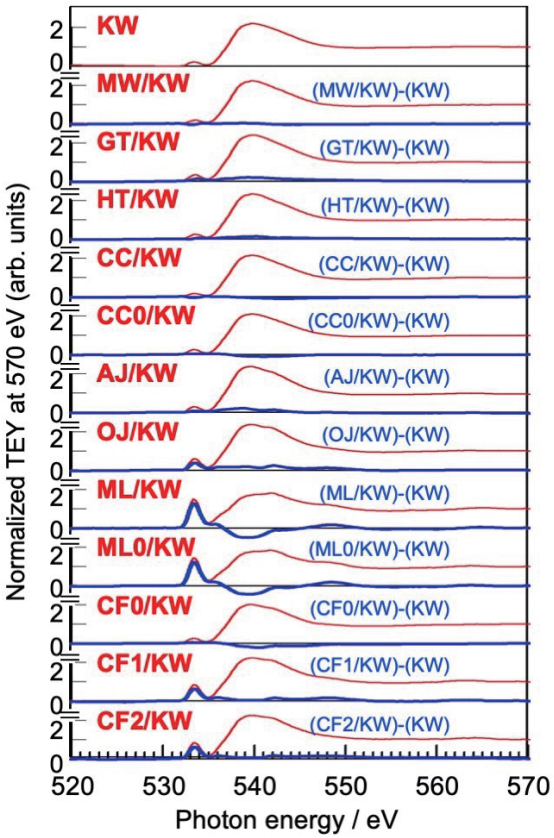

Fig. 4 TEY O *K*-XANES (red line) and the difference between Drink/KW and KW (blue line).

4. Conclusion

XAS of non-volatile components in drinks adsorbed on insulating wiping cloth (Kimwipe®) can be easily measured by the present TEY method. Especially, components of proteins and lipids can be clearly identified in C *K* and O *K*-XANES. However, the component of carbohydrate cannot be identified because Kimwipe® is made from carbohydrate as cellulose**.** It is therefore concluded that the present TEY method is useful to directly identify proteins or lipids in drinks adsorbed on insulating wiping clothes.

References

[1] Y. Muramatsu, The76th Annual Meeting of Analytical Chemistry, Japan, F1010 (2016).
[2] Y. Muramatsu and E. M. Gullikson, Anal. Sci., *accepted*.
[3] Y. Muramatsu and Y. Tani, LASTI Report, 19, 57-59 (2017).
[4] Y. Muramatsu, Y. Tani, Y. Tobita, S. Hamanaka and E. M. Gullikson, Adv. X-ray Chem. Anal., Japan, 49, 219-230 (2018).
[5] Y. Muramatsu, R. Maruyama, and E. M. Gullikson, Adv. X-ray Chem. Anal., Japan, 51, 179-190 (2020).

C *K*- and O *K*-XANES of alkyl-grafted graphite

Kota Masutani[1], Yasuji Muramatsu[1], and Hiroshi Yoshitani[2]
[1]Graduate School of Engineering, University of Hyogo
[2]SEKISUI CHEMICAL CO., LTD.

Abstract

To clarify the local structure of alkyl-grafted graphite, XANES spectra in the C *K* and O *K* regions of the graphite grafted with aldehyde solvents were measured in BL10/NewSUBARU. The grafted compounds exhibited specific peaks assigned to carbonyl structures in both C *K*- and O *K*-XANES. It is therefore confirmed that grafted compounds have much carbonyl bonds in grafted local structure of graphite with aldehyde.

1. Introduction

Graphene has excellent physical and mechanical properties. Since graphene has a high visible light transmittance of 97.7% and high transparency, its application to transparent conductive films is being investigated. Owing to its mechanical properties such as high elastic modulus (~1 TPa), it is expected to be used as a composite material in many applications.

Local structure analysis of grafted graphitic structures is important to develop and/or improve graphene. Especially for carbon materials, X-ray absorption near edge-structure (XANES) is a powerful tool for local structure analysis. Hence, in this study, we aim to clarify the local structure of alkyl-grafted graphite by using the XANES method.

2. Experimental

Alkyl-grafted graphite samples were provided by Oita University. Ternary graphite intercalation compounds (K-THF-GIC), which can be easily prepared by the solution method, were reacted with aldehyde compounds such as decanal, $CH_3(CH_2)_8CH{=}O$ and heptanal, $CH_3(CH_2)_5CH{=}O$ to yield alkyl-grafted graphites [1, 2].

For XANES measurements, samples of graphite, grafted compounds, mixtures of graphite/aldehyde-solvents, and aldehyde solvents are prepared. Powder samples of the graphite, grafted compounds, and mixtures of graphite/solvents were held on the indium substrate. Solvent samples were put on clean gold (Au) substrate. XANES measurements in the C *K* and O *K* regions were performed in BL10 at NewSUBARU using a total electron yield (TEY) method. Incident angle of soft X-ray beams to sample plane was set to the magic angle.

3. Results and Discussion

Figure 1 shows the C *K*-XANES of the graphite, solvent (decanal), graphited compound, and mixture (graphite/decanal). Graphite exhibits the typical graphite XANES profile with the π* peak at 285.5 eV and σ* peak at 293 eV. Hence the graphite sample can be surely confirmed as pure graphite. Solvent (decanal) exhibits a small π* peak due to the carbonyl carbon and a peak at 288 eV assigned to C-C bonds in alkyl chain. Grafted compound exhibits the π* peak at 285.5 and σ* peak at 293 eV, which come mainly from the matrix graphite. Additionally, two peaks can be clearly observed at 288 eV and 289 eV. The 288-eV peak corresponds to the same peak of decanal. The sharp 289-eV peak can be assigned to carbonyl C=O bonds. On the other hand, the mixture

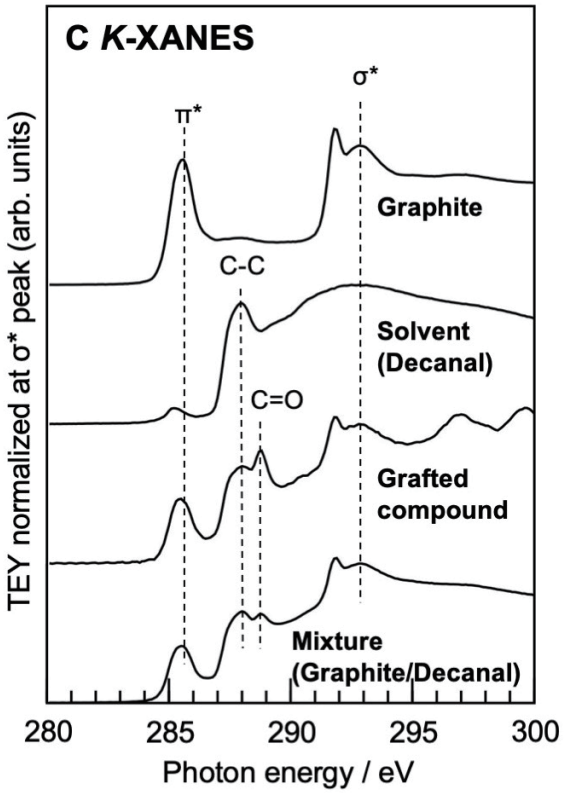

Fig. 1 C *K*-XANES of graphite, solvent (decanal), grafted compound, and the mixture of graphite and decanal.

(graphite/decanal) shows the π* peak, σ* peak, 288-eV peak, and 289-eV peak. This suggests that solvent (decanal) may be slightly oxidized in the mixture. However, the 289-eV peak in grafted compounds is much higher than that of mixture. It is therefore suggested that the grafted compound has much carbonyl bonds in grafted local structure of graphite with decanal.

Figure 2 shows the O *K*-XANES of the graphite, solvent (decanal), grafted compound, and mixture (graphite/decanal). Graphite exhibits no peak in O *K* region. It is therefore confirmed that the graphite has not been oxidized. Solvent (decanal) exhibits the π* peak near 531 eV and σ* peak near 538 eV, due to the carbonyl oxygen. Grafted compound exhibits an intense π* peak and sifted σ* peak near 543 eV. Mixture (graphite/decanal) exhibits the π* peak and σ* peak near 538 eV. This suggests that decanal may be slightly oxidized in the mixture. However, the π* peak in grafted compounds is much higher than that of mixture. This shows that the grafted compound has much carbonyl bonds in grafted local structure of graphite with decanal. Such the finding in O *K*-XANES is consistent with the C *K*-XANES.

Similar result was also obtained in the grafted compound with heptanal.

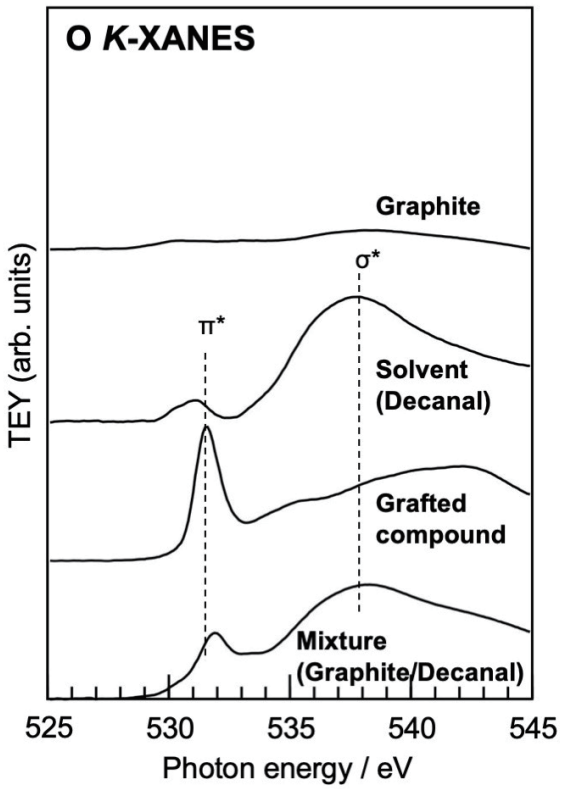

Fig. 2 O *K*-XANES of graphite, solvent (decanal), grafted compound, and the mixture of graphite and decanal.

4. Conclusion

To clarify the local structure of alkyl-grafted graphite prepared from graphite and aldehyde solvents, C *K*- and O *K*-XANES spectra of grafted compounds were measured in BL10/NewSUBARU. Grafted compounds clearly exhibit the specific peaks assigned to carbonyl carbon and oxygen (>C=O) in both C *K*- and O *K*-XANES. It is therefore suggested that grafted compounds form carbonyl bonding in graphite/aldehyde-solvents.

Acknowledgement

The authors are grateful to Professor Masahiro Toyoda (Oita University) for providing the alkyl-grafted graphite samples.

References

[1] International Application No. PCT/JP2020/007576.

[2] Y. Nanri, H. Yoshitani, H. Fukui, A. Nakasuga, T. Tsumura, and M. Toyoda, The 46th Carbon Material Society Annual Meeting, 1C01(2019).

Surface structural analysis of nanodiamond by soft X-ray absorption spectroscopy and first principles calculation (2); Nitrogen-incorporated local structure

Tatsuki Maeda and Yasuji Muramatsu
Graduate School of Engineering, University of Hyogo

Abstract

To clarify the surface structure of nanodiamonds, XANES spectra of detonation nanodiamond (DND) samples were measured in BL10 at the NewSUBARU, and they were theoretically analyzed using the first-principles calculations. As the second report on the nanodiamond, XANES analysis was performed by calculating the nanodiamond cluster $C_{144}H_{28}N_3O_2$ in which nitrogen atoms are incorporated in the core cluster. From these measurements and calculations, it is has been suggested that DND is covered by a fused hexagonal and pentagonal ring structure consisting of sp^2 carbons, and that there are NV defects with nitrogen atoms incorporated in the core cluster.

1. Introduction

Nanodiamonds have attracted much attention as functional materials because of their excellent mechanical and electrical properties. To develop the functional nanodiamonds, surface structural analysis is important, because surface effect should become significant in the nano-scale particles. Soft X-ray absorption spectroscopy (XAS) is a powerful tool for characterization of low-*Z* materials. Especially, X-ray absorption near-edge structure (XANES) with a total-electron-yield (TEY) method easily provides element-selective electronic structure information on quasi-surface of materials. Hence, local structure can be clarified from the XANES measurements and theoretical analysis using the first principle calculations. In our previous report [1], we have measured C *K*-XANES of various detonation nanodiamond (DND), and confirmed that surface of DND particles can be covered with sp^2 carbon atoms forming polycyclic hexagonal and/or pentagonal rings. However, the specific fine structure around π* peak in C *K*-XANES has not been assigned by the proposed surface structure model.

In N *K*-XANES of DND, it was observed that nitrogen can be slightly incorporated in DND. Considering the synthesis process of DND, it will be possible that nitrogen may be incorporated in DND. Hence, in the present study, C *K*- and N *K*-XANES of DND have been theoretically analyzed by using the nanodiamond cluster $C_{144}H_{28}N_3O_2$ in which nitrogen atoms are incorporated in the core cluster.

2. XANES measurements and calculations

DND samples were provided by Daicel Corporation. XANES in the C *K*- and N *K*-regions of them were measured in BL-10/NewSUBARU with a total-electron-yield (TEY) method. Details of the XANES measurements are described in the previous report [1].

XANES were theoretically simulated by using the first principles calculation package of CASTEP [2]. Appropriate nanodiamond cluster model incorporating N atoms was put in the center of a supercell. In order to suppress intermolecular interaction, the distance between the supercell boundaries and the model was set to longer than 5 Å. After the structure optimization by the Material Studio package, ground-state calculations were performed. Then, excited-state calculations were carried out by providing core hole in the 1s orbital of the target atom. Transition energy was corrected by the Mizoguchi method [3].

3. Results and Discussion

Figure 1 shows the N-incorporated nanodiamond cluster model ($C_{144}H_{28}N_3O_2$) and its calculated C *K*-XANES, compared to the measured XANES of DND. The N-incorporated model is based on the bucky nanodiamond model ($C_{144}H_{28}N_3O_2$) [4], in which the sp^3-carbon diamond core cluster is covered by the sp^2-carbon fused hexagonal and pentagonal rings (bucky). The N-incorporated nanodiamond cluster model of $C_{144}H_{28}N_3O_2$ has one nitro group on the surface, one nitrogen substituted for the sp^2 carbon, and one nitrogen substituted for the carbon in the core cluster. Thus, one NV defect is formed in the core cluster. Calculated XANES of carbon atoms (labelled as C1 ~ C3) in core cluster and of carbon atoms (C4 ~ C8) in surface bucky are compared to the measured XANES. Fine

structure of π* peak (labelled as *a* ~ *c*) was observed in DND. The peaks *b* and *c* can be almost reproduced by the C1~C8. However, peak *a* cannot be still reproduced by such the model. Hence, other bucky structures and/or chemical bonds should be taken into the models.

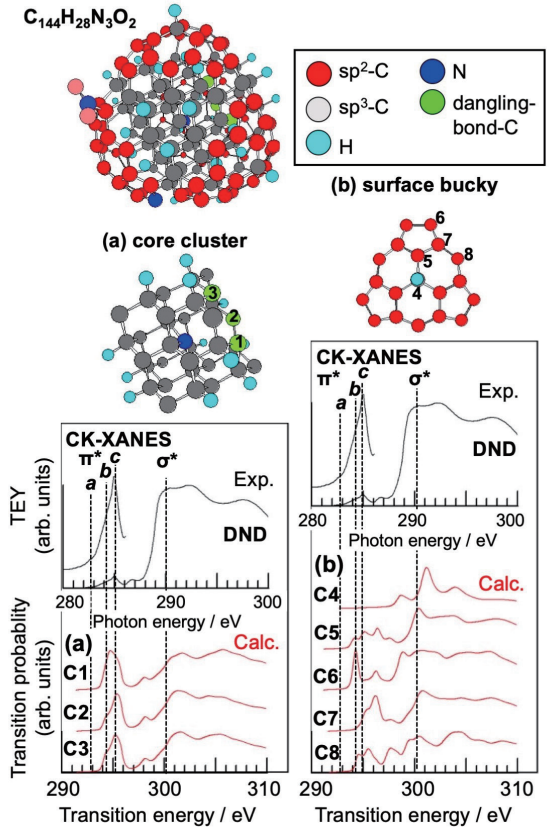

Fig. 1 Calculated C *K*-XANES of Nanodiamond cluster ($C_{144}H_{28}N_3O_2$), compared to the measured XANES of DND. Left panel shows the calculated XANES of C1~C3 in the core cluster (a), and right shows the calculated XANES of C4~C8 in the surface bucky.

Figure 2 shows the calculated N *K*-XANES of the N-incorporated nanodiamond cluster model ($C_{144}H_{28}N_3O_2$), compared to the measured XANES of DND. Measured XANES exhibits fine structure denoted as *d* ~ *g* in the Figure. Broad peak profile composed of *f* and *g* is almost reproduced by N1 ~ N3. Small peak *e* can be reproduced by N2. However peak *d* cannot be reproduced by N1 ~ N3. Other local structure of nitrogen in diamond with vacancies should be further considered.

4. Conclusion

Calculated C *K*- and N *K*-XANES of N-incorporated nanodiamond cluster model ($C_{144}H_{28}N_3O_2$) were obtained by the first principles calculation package of CASTEP. Compared to the measured XANES, fine structures at the lowest energy side both in C *K* and N *K* threshold cannot be reproduced by the model. Hence other N-incorporated models in diamond with vacancies should be further calculated.

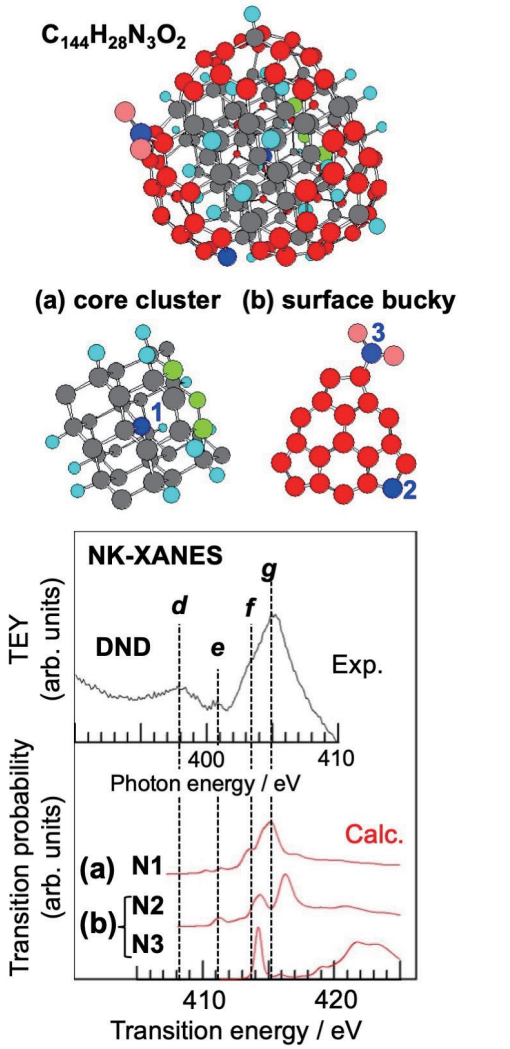

Fig. 2 Calculated N *K*-XANES of N1 in core cluster (a) and N2~N3 in surface bucky (b) in the nanodiamond cluster ($C_{144}H_{28}N_3O_2$), compared to the measured XANES of DND.

References

[1] T. Maeda and Y. Muramatsu, LASTI Annual Report, 20, 55-56 (2018).

[2] J. Clark, M. D. Segall, C.J. Pickard, P. J. Hasnip, M. J. Probert, K. Refson, and, M. C. Z. Payne, Krystallogr, 220, 567-570 (2005).

[3] T. Mizoguchi, I. Tanaka, S.-P. Gao, and C. J. Pickard, J. Phys. Condens. Matter, 21,104204 (2009).

[4] J.-Y. Raty, G. Galli, C. Bostedt, T. W. van Buuren, and L. J. Terminello, Phys. Rev. Lett. 90, 037401 (2003).

Soft X-ray absorption measurements of self-standing polyethylene (PE) thin films using a transmission method (2); 200 nm-thick PE film

Yuya Matsumoto and Yasuji Muramatsu
Graduate School of Engineering, University of Hyogo

Abstract

To experimentally determine the mass absorption coefficient (μ) in soft X-ray region of the sp^3 carbon atom, we have measured X-ray absorption spectra of self-standing polyethylene (PE) thin films using a transmission method in BL-6.3.2/ALS and BL10/NewSUBARU. The 200-nm thick PE film was prepared with a spin coating method. The measured μ spectrum in the 200~800 eV was in good agreement with calculated μ. In C *K* region, the measured μ was higher than the calculated μ, because of the photoelectric scattering due to the σ* resonance. The μ of the sp^3 carbon atom can be experimentally determined to be 60000 cm^2/g at the σ* peak in C *K* region.

1. Introduction

To determine the mass absorption coefficient (μ) in X-ray absorption spectroscopy (XAS), a transmission method should be basically used according to the Lambert-Beer's law. However, in soft X-ray region, the value of μ is generally so large that sufficiently thin samples should be prepared and it is experimentally hard to perform the transmission method. Therefore, a total-electron-yield (TEY) method is often used in soft X-ray absorption measurements.

Recently we have tried to determine the μ of sp^2-carbon atoms by using ultra-thin graphite films [1]. In the next step, we are trying to determine the μ of sp^3-carbon atoms. The most typical material consisting of sp^3-carbon is diamond. Transmission length in C*K* region of diamond (density, ρ=3.5 g cm^{-3}) is estimated to be less than 50 nm. However, it is difficult to get such the self-standing ultra-thin diamond films. Hence, we have focused on polyethylene (PE) films, because its low density (ρ < 1 g cm^{-3}) and longer transmission length in C *K* region. Figure 1 shows the calculated transmission length of PE in soft X-ray region. The calculations were performed with the on-line system of the Center for X-Ray Optics (CXRO) [2,3]. The 200 nm-thick PE sufficiently transmits X-rays in C *K* region, and 1 μm-thick PE transmits ~500 eV X-rays. This means that μ in soft X-ray region can be experimentally determined by using 200 nm~1 μm-thick PE films with a transmission method.

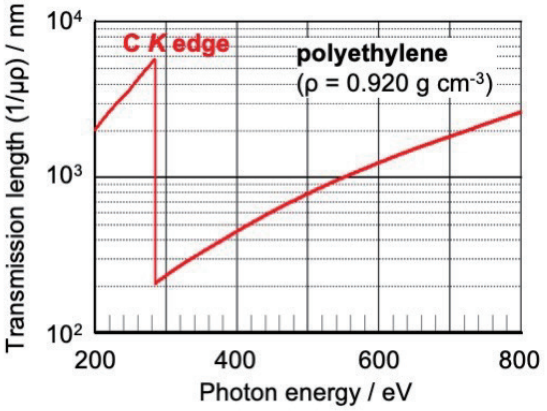

Fig. 1 Calculated transmission length in the 200 ~ 800 eV region of PE film.

In the previous study, we have measured XAS spectra of commercially available 1.4~2.8-μm thick PE films with a transmission method [4]. It was confirmed that the PE films were too thick to measure μ in C *K* region. Hence, in the present study, we have prepared sufficiently thin (200-nm thick) PE films, and measured XAS in the 200~800 eV region including C *K* edge of them using a transmission method.

2. Experiments

Commercially available PE powder was dissolved in decahydronaphthalene, and a PE thin film was formed on a silicon wafer substrate by a spin coating method. The PE thin film was peeled off from the silicon wafer substrate using Scotch® tape. The film thickness was measured to be 200 nm by using a stylus profiler (KLA-Tenchore, P-6). Density (ρ) of the film was measured to be 0.92 g/cm^3 by using a float-sink method using ethanol and water. The measured ρ is in good agreement with the standard value (0.91~0.96 g/cm^3) of conventional PE films. The PE film was placed on an Al substrate which opened a 3 x 3 mm^2 window, and was held at both edges of the window frame using conductive carbon (C) tapes, as shown in Figure 2. Soft X-ray absorption spectra of the self-standing PE thin film sample was measured in BL-6.3.2/ALS and BL10/NewSUBARU. Measurement region was set to 200~800 eV, and filters (C, Ti, Cr, and Co) were appropriately inserted to suppress higher-order light over the entire region (BL-6.3.2/ALS). No filter was used in BL10/NewSUBARU. Intensity of transmitted X-rays through the PE film was measured with a photodiode detector. TEY spectra of the PE film were measured by monitoring sample current through

the C-tape/Al-substrate during soft X-ray irradiation onto the PE film adhered to the C-tape.

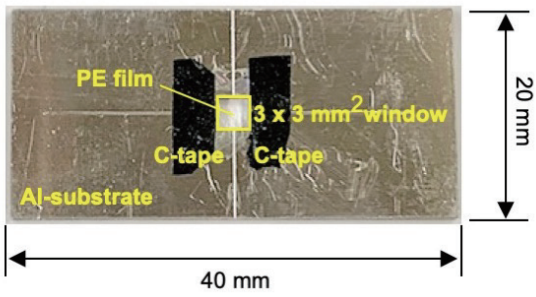

Fig. 2 Photo of PE film covering the 3x3 mm^2-window of an Al substrate.

3. Results and Discussion

The μ spectra converted from the measured absorbance are shown in Figure 3 in comparison with the calculated μ spectra. Spectral shape of the measured μ spectrum in the 200-800 eV region except for C *K* region is in good agreement with that of calculated spectrum. This shows that the measurements of μ using the 200-nm thick PE film have been correctly performed. In C *K*-XANES, the measured μ in the 287 ~ 305 eV is higher than that of calculated μ. At the absorption edge, X-ray absorption consists of X-ray scattering absorption and photoelectric absorption. The calculated μ mainly reflects the X-ray scattering absorption, while the measured μ reflects the X-ray scattering and photoelectric absorption. Hence, the higher portion of measured μ can be assigned to the photoelectric scattering due to the σ* resonance absorption. It is therefore confirmed that the measurements of μ using the 200-nm thick PE film have been correctly performed in the C *K* region. The measure μ at the σ* peak in C *K* region of sp^3 carbon atom can be determined as approximately 60000 cm^2/g.

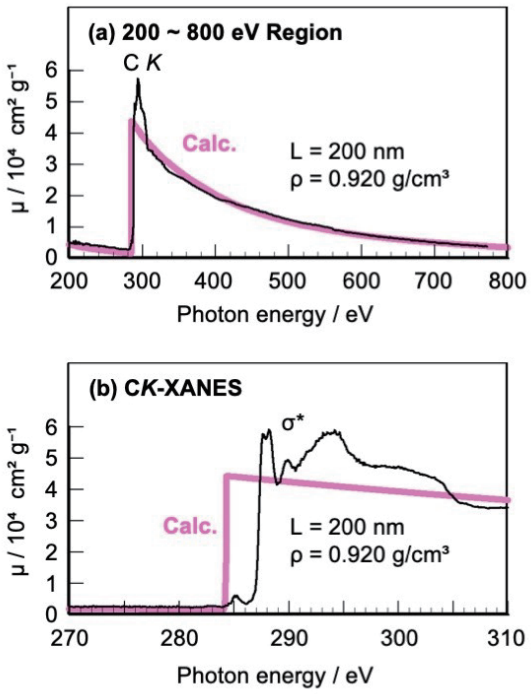

Fig. 3 Comparisons of the μ spectra measured in the 200~800 eV region (a) and C *K* region (b) of PE film with the calculated μ spectra.

4. Conclusion

To experimentally determine μ in the soft X-ray region of sp^3 carbon atom, XAS of the self-standing 200-nm thick PE film was measured with a transmission method. The measured μ spectral profile in the 200 ~ 800 eV region was in good agreement with the calculated μ. In C *K* region, measured μ was higher than that of calculated μ, because of the photoelectric scattering due to the σ* resonance. The measure μ at the σ* peak in C *K* region of sp^3 carbon atom can be determined as approximately 60000 cm^2/g.

References

[1] Y. Muramatsu, Y. Soneda, and E. M. Gullikson, The 40th International Conference on Vacuum Ultraviolet and X-ray Physics, VUVX19, Poster 28 (2019).

[2] http://henke.lbl.grov/optical_constants/

[3] B.L. Henke, E.M. Gullikson, and J.C. Davis, Atomic Data and Nuclear Data Tables Vol. **54**, 181-342 (1993).

[4] Y. Matsumoto and Y. Muramatsu, LASTI Annual Report, 20, 53-54 (2018).

Direct detection of PM2.5 collected on insulating membrane filters using a total-electron-yield soft X-ray absorption spectroscopy (2); Quantitative analysis

Takuya Motokawa and Yasuji Muramatsu
Graduate School of Engineering, University of Hyogo

Abstract

To apply the total electron yield (TEY) method for quantitative analysis of atmospheric environmental carbon particles, TEY-C *K*-XANES of reference graphitic carbon samples put on insulating membrane filters were measured. Calibration curve can be successfully obtained from the relationship between the π* peak height and carbon concentration. By using the calibration curve, concentration of graphitic carbons in the PM2.5 samples collected in Kobe can be estimated as 4.5 μg/cm^2.

1. Introduction

We have developed a new method for total-electron-yield (TEY) measurements of insulating bulk samples [1-3]. In this method, insulating film samples, whose thickness is ~100 μm, are put on conductive substrates. Sample current of the film samples can be sufficiently detected through the substrate, during soft X-ray irradiation onto the samples. Such the TEY method enables to easily measure X-ray absorption near-edge structure (XANES) of insulating materials.

To utilize this method for chemical analysis of insulating materials, we have focused on the atmospheric environmental analysis. Hence, we have measured XANES of particulate matter (PM) 2.5 collected on insulating membrane filters. In our previous measurements, we have successfully detected the PM2.5 carbons collected on filters by the proposed TEY method [4]. From the TEY-C *K*-XANES, chemical states of PM2.5 can be analyzed as the mixture of graphitic sp^2-carbon and alkyl sp^3-carbons. Further application of this method is the quantitative analysis of PM2.5. In the present study, we have tried to quantitatively measure the PM2.5 by using the TEY method.

2. Experiments

Figure 1 shows the sample plate for TEY-XANES measurements. The PM2.5 sample (denoted as HPM) was prepared by the Hyogo Prefectural Environmental Research Center in Kobe. The PM2.5 was collected on the commercially available air monitoring PTFE membrane filter (Whatman) in Kobe city on June, 2017. The blank filter is denoted as FTB, and newly prepared same filter is denoted as FT. We have prepared reference carbon samples collected on PTFE filters to obtain a calibration curve for quantitative analysis of PM2.5. Carbon black (CB) powder dispersed in organic solvent was prepared by Mikuni Color Ltd. The CB solution was diluted with alcohol, and 1-fold, (denoted as C1), 5-fold (C5), 10-fold (C10), 20-fold (C20), 50-fold (C50), and 100-fold dilute solutions were prepared. These dilute solutions were dropped on the PTFE filters and dried. Amounts of CB (μg/cm^2) on C1 ~ C100 are measured as described in Figure 1. These samples were cut into 5x5 mm^2 pieces and put on an aluminum (Al) plate by using carbon (C) tapes.

TEY X-ray absorption measurements in the C *K*, O *K*, and 200 ~ 600 eV regions of the samples were performed in the analysis chamber at the BL10/NewSUBARU [5]. Incident soft X-ray intensity (I_0) was monitored with sample current of a clean gold (Au) plate. Then, TEY can be obtained as the sample current (I) divided by I_0.

3. Results and Discussion

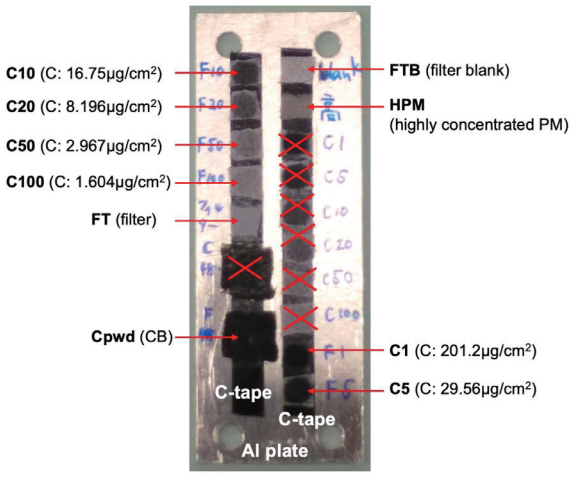

Fig. 1 Photo of filter and reference carbon samples.

Figure 2 shows the C *K*-XANES of HPM and FTB, in which background was deleted and normalized at 296 eV on the σ* peak. Compared to the FTB, HPM exhibits the higher π* peak at 285.5

eV and a peak near 288 eV assigned to C-H bonds. This means that PM2.5 consists of sp^2 and sp^3 carbons. Hence, the peak heights at 285.5 eV and 288 eV will be quantitative indices for sp^2 and sp^3 carbons, respectively.

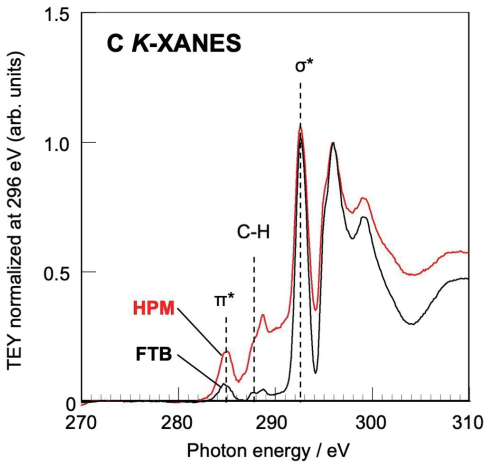

Fig. 2 C *K*-XANES normalized at 296 eV of the HPM and FTB.

Figure 3 show the C *K*-XANES of the reference carbon samples (C1~C100) and filter (FT). Background of the measured XANES was deleted and TEY intensity was normalized at 296 eV on the σ* peak. As shown in the figure, π* peak height decreases in C1 to C100. This suggests that the π* peak height will be a calibration index for sp^2 carbons.

Figure 4 shows the relationship between the π* peak height of C1~C100 as the function of weight of carbon per unit area on the linear-log scale. The relationship can be well approximated by the function of f(x) = 0.34 log (x) - 0.086 with the high correlation coefficient of R^2 = 0.99. Hence, the approximated line can be applicable to a calibration curve for sp^2 carbons. In Figure 2, the π* peak height difference between HPM and FTB was 0.135. Applying this π* peak height of HPM to the calibration curve, amount of sp^2 carbons in HPM can be obtained as 4.5 μg/cm^2.

4. Conclusion

To apply the TEY method for quantitative analysis of atmospheric environmental carbon particles collected on insulating membrane filters, calibration curve for quantitative analysis for sp^2 carbons was successfully obtained from the π* peak height in C *K*-XANES of reference carbon samples. From the calibration curve, amount of sp^2 carbons in the collected PM2.5 was measured to be 4.5μg/cm^2. As previously reported [4], the TEY method enable the direct detection and chemical-state analysis of PM2.5. Hence, the TEY method would be a powerful tool for the chemical-state and quantitative analyses of atmospheric environmental particles.

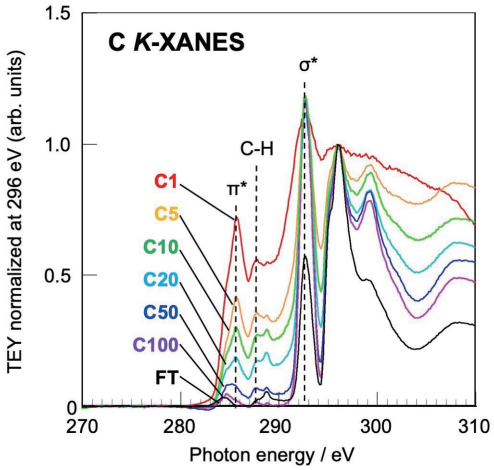

Fig. 3 C *K*-XANES normalized at 296 eV of the reference carbon samples on filters.

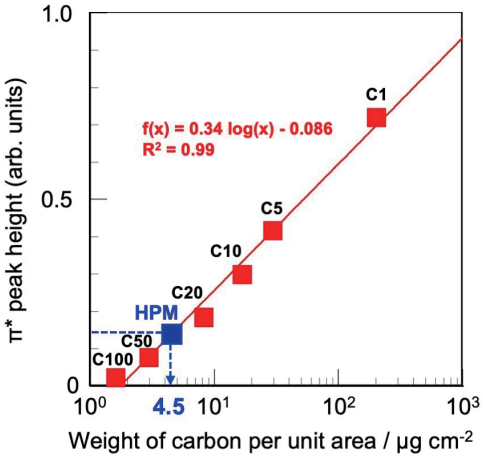

Fig. 4 π* peak height of HPM on the calibration curve obtained from C1 ~ C100.

References

[1] Y. Muramatsu, The 76th Annual Meeting of Analytical Chemistry, Japan, F1010 (2016).

[2] Y. Muramatsu and E. M. Gullikson, Anal. Sci., *accepted*.

[3] Y. Muramatsu, Y. Tani, Y. Tobita, S. Hamanaka, and E. M. Gullikson, Adv. X-Ray Chem. Anal. Japan, 49, 219-230 (2018).

[4] T. Motokawa and Y. Muramatsu, LASTI Annual Report, 20, 57-58 (2018).

[5] Y. Muramatsu, A. Tsueda, T. Uemura, K. Nambu, T. Ouchi, T. Harada, T. Watanabe, and H. Kinoshita, LASTI Annual Report, 17, 29-30 (2015).

X-ray Radiolysis-based Three Dimensional Additive Manufacturing Process

S.Saegusa, Y.Utsumi, S.Suzuki, A.Yamaguchi
LASTI, University of Hyogo

Abstract

To achieve the three dimensional additive manufacturing process, we investigated X-ray radiolysis –induced photochemical reaction of $Cu(CH_3COO)_2$ solution. Here we demonstrated synthesis and immobilization of copper and copper oxide particles onto an aluminium substrate directly from the liquid solution. Our study will shed light on understanding and providing a novel photochemical reaction route induced under the X-ray irradiation. The development of X-ray radiolysis-induced photochemical reaction process enables us to achieve the rapid and easy formation of higher-order nano/micro-scale structures consisting of composite materials.

Introduction

Three dimensional (3D) printing and additive manufacturing process have attracted much attention because of their easy and intriguing applicability and engineering applications. [1] Until now, there are few systems which can fabricate a structure consisting of composite materials such as metallic, plastic, and oxidized materials etc. One of the candidates which can achieve the formation of composite 3D structure is considered to be a system using photochemical reaction due to laser [2] or X-ray radiolysis [3 - 5].

In this study, we demonstrated the synthesis of nano/micro-scale metallic particles and clusters onto an aluminium substrate including Mg as an impurity by the X-ray radiolysis-induced photochemical reaction combined with a fluidic channel at a synchrotron radiation (SR) facility because the advantage of performing X-ray radiolysis-induced photochemical reaction using SR is its atomic level of processing accuracy.

Experiments and Results

A. X-ray irradiation of aqueous solution with a liquid flow system

We prepared copper (II) acetate $[Cu(CH_3COO)_2]$ solution with an additive methanol in SR X-ray radiolysis experiments with a fluidic channel as schematically shown in Fig. 1. First, a liquid solution of 0.1 mol/L (M) $[Cu(CH_3COO)_2]$ was prepared. Next, we added methanol into the $[Cu(CH_3COO)_2]$ at a ratio of methanol : $[Cu(CH_3COO)_2] = 1 : 20$ and prepared this mixed solution as the stock solution because no particles were synthesized and immobilized onto a substrate immersed in the aqueous $[Cu(CH_3COO)_2]$ solution including of no additive [4]. We can control the flow rate ranging from 1 to 75 mL/min in the fluidic channel. Specimen such as aluminium-based substrates were dipped in the X-ray irradiation cell, and irradiated by 5 minute X-ray as shown in Fig. 1. After the X-ray exposure, the specimen were washed with deionized water to remove residual materials which leaving the particles behind.

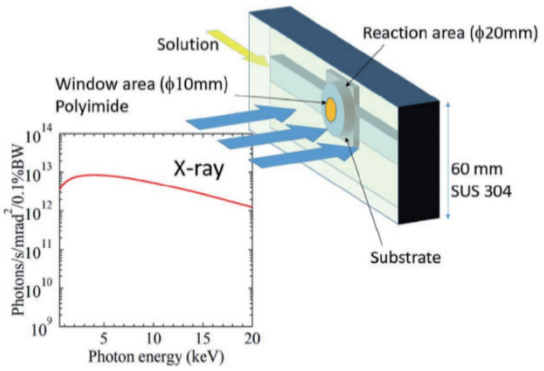

Fig.1 Schematic of X-ray irradiation experiment. The irradiation cell is connected to a liquid flow system. The liquid flow system can control the flow rate ranging from 1.0 to 75.0 mL/min.

B. Results

To obtain the understanding the composition of the particles synthesized by the X-ray radiolysis-induced photochemical reaction, the micro-Raman spectroscopy was performed. Figures 2(a) and 2(b) display the spectra of three particles synthesized when the flow rate of 60.0 and 7.5 mL/min, respectively. The optical photographs show the measurement points. Comparing the corresponding spectra, we found that the spectra

are diverse. For example, the spectrum (3) in Fig. 2(a) is independent on Raman shift. The corresponding particle (3) is attributed to a metallic copper particle.The particle (1) in Fig. 2(a) is expected to be almost Cu_2O while the particle (2) is considered to be a mixture of Cu_2O and CuO. On the other hand, the main component of the particle (3) in Fig.2 (b) is expected to be CuO. The particles (1) and (2) in Fig. 2(b) are almost similar with those in Fig. 2(a). The results indicate that various particles are synthesized and immobilized by the X-ray radiolysis-induced photochemical reaction in the fluidic solution.

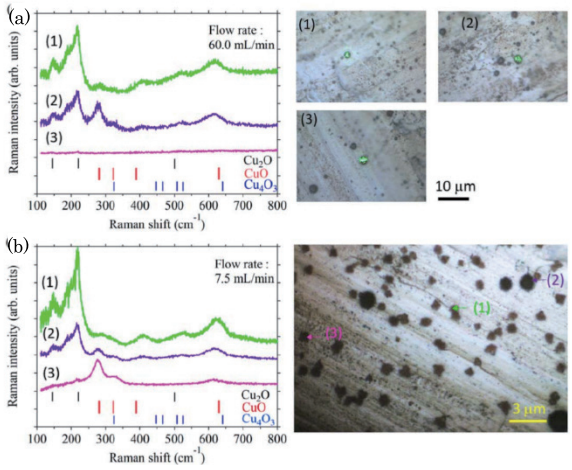

Fig.2 Raman spectra of particles synthesized by the X-ray radiolysis with the flow rates of (a) 60.0 and (b) 7.5 mL/min, respectively. Numbered spectra are respectively measured from the corresponding particles shown in optical photographs.

Figures 3(a) – 3(c) display the SEM images of particles synthesized by the X-ray irradiation with the liquid flow rates of 60.0, 30.0, and 7.5 mL/min, respectively. As shown in these SEM images, the particle sizes trend to increase with decreasing the flow rate. Figure 3(d) shows the summary of the liquid flow rate dependence of the synthesized particle size. It is found that the particle size clearly increases with decreasing the flow rate. The area ratio also increases with decreasing the flow rate. These results can provide a clue to understand the mechanism of these phenomena and to control and develop a novel process to three dimensional printing and additive manufacturing combined with electroplating. [4, 5]

Conclusions

The study demonstrates the flow rate dependence of copper-based particles synthesized by the X-ray-radiolysis-induced

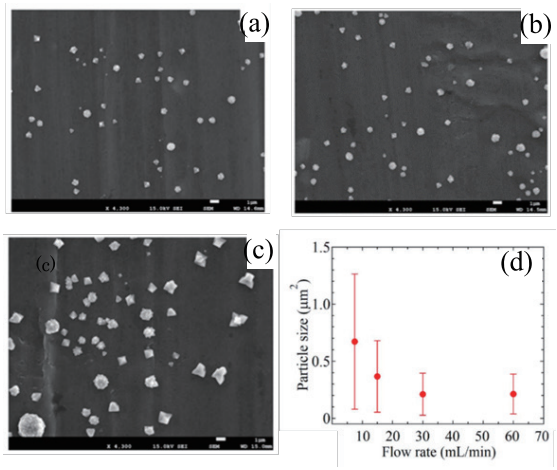

Fig. 3 SEM images of particles synthesized by the 5 min X-ray irradiation with the liquid flow rates of (a) 60.0, (b) 30.0, and (c) 7.5 mL/min, respectively. The scale bars in the SEM images are 1μm. (d) Flow rate dependence of synthesized particle average size.

photochemical reaction. This study enables us to provide the possibility to fabricate nano/micro higher-order nano/micro-scale structures consisting of composite materials.

References

[1] E. Sachs, M. Cima, P. Williams, D. Brancazio, J. Cornie, "Three Dimensional Printing: Rapid Tooling and Prototypes Directly from a CAD Model," J. Eng. Ind. vol. 114, pp. 481 – 488 (1992); E. Sachs, M. Cima, J. Cornie, "Three-Dimensional Printing: Rapid Tooling and Prototypes Directly from CAD Model," CIRP Annals, vol. 39, pp. 201 – 204 (1990).

[2] C. H. Bae, S. H. Nam, S. M. Park, "Formation of silver nanoparticles by lase ablation of a silver target in NaCl solution," Appl. Surf. Science vol. 197-198, pp. 628 – 634 (2002).

[3] Q. Ma, N. Moldovan, D. C. Mancini, R. A. Rosenberg, "Synchrotron-radiation-induced, selective-area deposition of gold on polyimide from solution," Applied Physics Letters, vol. 76, no. 15, pp. 2014 – 2016 (2000).

[4] A. Yamaguchi, T. Fukuoka, I. Okada, M. Ishihara, I. Sakurai, Y. Utsumi, "Caltrop particles synthesized by photochemical reaction induced by X-ray radiolysis," J. Synchrotron Rad. vol .24, pp. 653 – 660 (2017).

[5] S. Saegusa, I. Sakurai, I. Okada, T. Fukuoka, S. Suzuki, Y. Utsumi, A. Yamaguchi, "X-ray Radiolysis-based Three Dimensional Additive Manufacturing Process," The Japan Institute of Electronics Packaging, vol . 12 E19-003-1-7 (2019)

For active surface-enhanced Raman scattering molecular detection, aggregation and dispersion of Au-nanoparticle-decorate polystyrene beads

Akinobu Yamaguchi, Takao Fukuoka, Yuichi Utsumi
LASTI, University of Hyogo

Abstract

Aggregation and dispersion of Au-nanoparticle-decorated polystyrene (AuNPs-decorated PS) beads are investigated for the formation of novel higher-order nanostructure with surface-enhanced Raman scattering (SERS) activity. In a lab-on-a-Chip scenario to serve a wide range of applications in life science, the AC-electric-field-induced active aggregate of AuNPs-decorated PS beads shed light on rapid detection or imaging for molecular for point-of-care testing.

Introduction

Surface-enhanced Raman scattering (SERS) based molecular analysis techniques demonstrate highly attractive characteristics in terms of sensitivity, cost, speed, portability, controllability, and multiplexing.[1] In medical diagnosis and environmental analysis, the use of SERS is a favorable analytical technique due to its rapid analysis with label free detection. The SERS detections require a noble metal nanostructure. Gold or silver nanoparticles are usually used during analysis because of their strong localized surface plasmon resonance excitation. Until now, the active control of aggregation and dispersion in microfluidic channels is generally difficult.

The external controllability, due to dielectrophoresis and alternative (AC) electro-osmostic effect, allows for the nano/micro-machining of the SERS-active particles. The AC-electric-controllable-SERS systems provide intrinsic advantages for both colloidal and nanofabricated systems with high-throughput analysis and label-free spectroscopy. [2 - 4]

Such efforts have attracted the attention of academic researchers as well as engineers focusing on the development of biosensors and nano/micro medical systems.

Experiments and Results

Figure 1(a) displays a schematic illustration of our integrated optofluidic system in order to achieve dynamic aggregation and dispersion of gold nanoparticles decorated polystyrene beads (AuNPs-decorated PS beads) with SERS activity using dielectrophoresis or AC electro-osmotic (ACEO) effect induced by AC electric field application. We prepared the AuNPs-decorated PS beads with various coverage of AuNPs. We

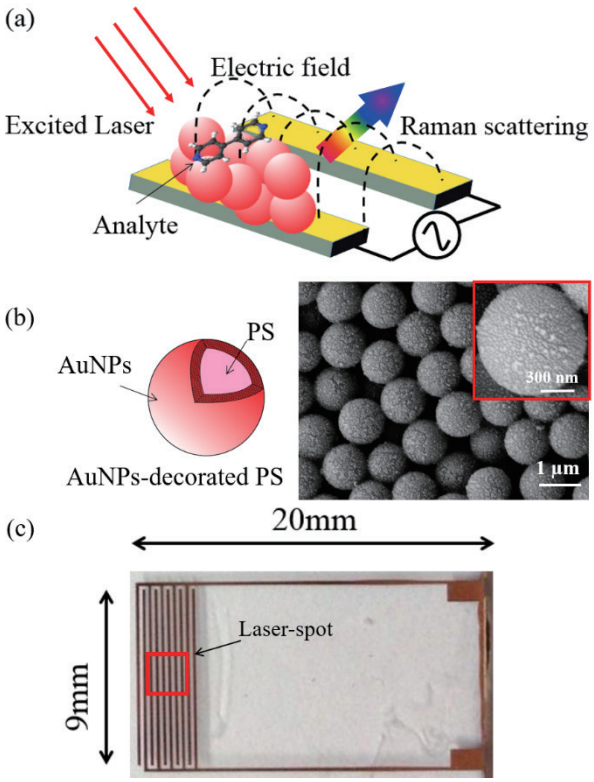

Fig. 1 (a) Schematic illustration of AC-electric-field-induced gold nanoparticles decorated polystyrene beads (AuNPs-decorated PS beads) with SERS activity. (b) Schematic illustration and typical scanning microscope (SEM) image of the AuNPs-decorated PS beads. (c) Optical micrograph of fabricated interdigital electrodes.

applied an AC electric field of 10 Vpp (voltage from peak to peak). We changed frequency of AC electric field ranging from 200 kHz to 1 kHz. During the AC electric field application, the real-space observation of AC-electric-field-induced aggregation and SERS measurements were

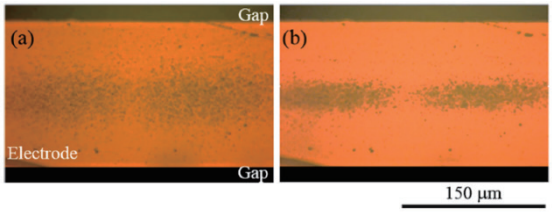

Fig. 2(a) Optical micrographs of the sample well containing a solution of 1 mM 4, 4'-bipyridine (4bpy) and AuNPs-decorated PS beads (a) before and (b) after the application of AC-electric-field at 1 kHz and 10 Vpp (voltage of peak to peak).

performed. Here, we use a fiber-type, simple Raman spectrometer RAM-100S. All experiments were performed at room temperature.

We demonstrated the AC-electric-field-induced aggregation of AuNPs-decorated PS beads in the device containing a solution of 1 mM 4, 4'-bipyridine (4bpy). As shown in Fig. 2(a), the AuNPs-decorated PS beads seemed to be almost randomly dispersed before the application of AC-electric field. When the AC electric field with frequency of 1 kHz was applied, the AuNPs-decorated PS beads were displaced to the middle of the electrode and gathered as shown in Fig. 2(b). When the frequency was changed from 1 kHz to 200 kHz, the AuNPs-decorated PS beads were moving in a little bit opposite direction, but after that, dispersing randomly. Then, we measured the SERS spectra during the application of AC-electric field of 1 kHz every 1 minute as shown in Fig. 3(a). We also evaluated the peak intensity at about 1580 cm^{-1} and plotted the time dependence of the peal intensity in Fig. 3(b). The increase of the Raman intensity are revealed in both 1st and 2nd experiments when the AC-electric-filed-enabled aggregation of the particles is induced by the application of 1 kHz AC field. When the AC electric field was turned off, the trend of decrease of Raman intensity on time was found. This result was attributable to the dispersion of dimer which induced the SERS hot spot.[4]

To understand the AC electric field duration and time dependence of SERS intensity, we consider a phenomenological model, which provides a possible explanation for its dependence. As a result, as shown in Fig. 3(b), the model presented qualitatively explains the duration time dependence for the SERS signal.

Conclusions

The study demonstrates the feasibility of developing integrated medical nano/micromachines that are multifunctional and controllable by the application of an external input. Further design, integration, and improvem

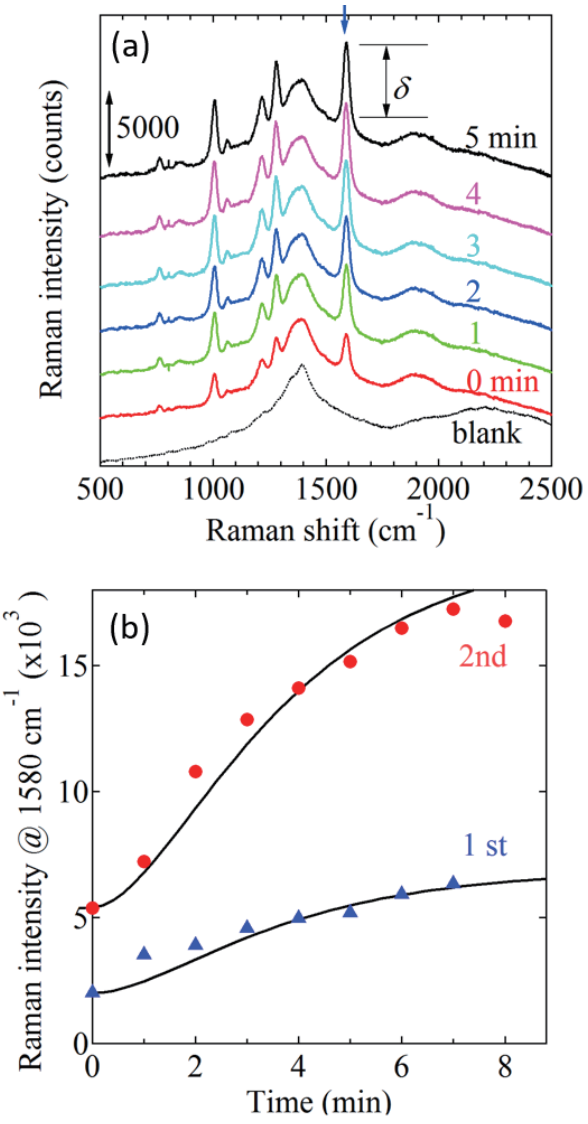

Fig. 3(a) Time dependence of SERS spectra during AC-electric-field-induced-aggregation of AuNPs-decorated PS beads and 4bpy molecules. (b) Duration time dependence of the SERS intensity at about 1580cm-1 with respect to AC-electric-field-induced aggregation process. The solid lines are analytical theoretical model fitting curves.

ent of AuNPs-decorated PS beads are the subjects of future studies.

References

[1] E. C. Le Ru and P. G. Etchegoin, "Principles of Surface-Enhanced Raman Spectroscopy and related plasmonic effects", Elsevier, 2009.

[2] A. Yamaguchi *et al.*, Sens. Actuat. B; Chem. 230, pp. 94 – 100 (2016).

[3] A. Yamaguchi *et al.*, Colloids Surf. A 507, pp. 118 – 123 (2016).

[4] A. Yamaguchi *et al.,* Appli. Surf. Sci. 465, pp. 405 – 412 (2019).

Part 3. List of Publications

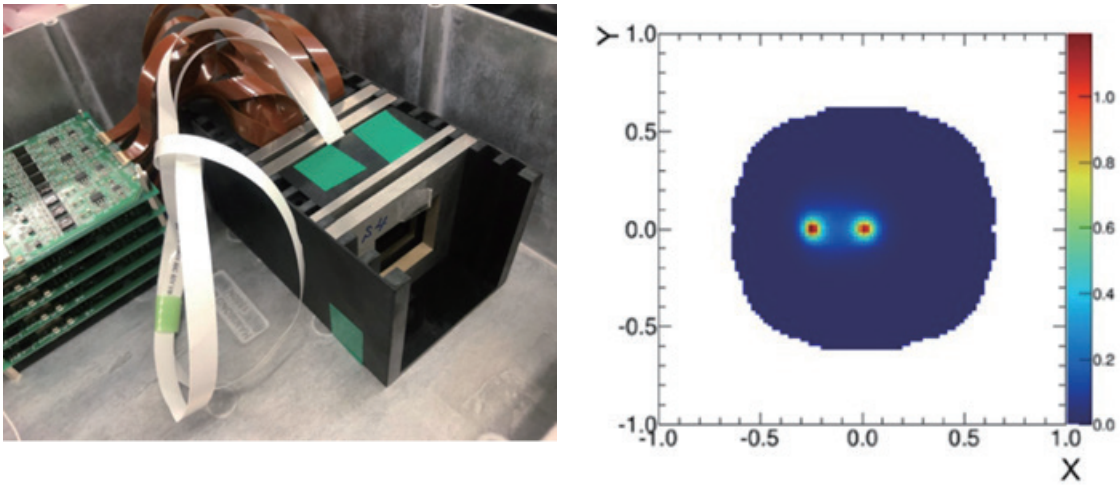

Newly developed compact Compton camera
and measured gamma ray image.
(Press release on January 30, 2020)

Papers

1. **"Development and performance verification of a 3-D position sensitive Compton camera for imaging MeV gamma rays"**
   H. Hosokoshi, J. Kataoka, S. Mochizuki, M. Yoneyama, S. Ito, H. Kiji, F. Nishi, S. Miyamoto, and Tatsushi Shima
   Nature Scientific Reports (2019) Vol. 9, 18551,
   DOI: 10.1038/s41598-019-54862-z

2. **"γ-ray strength function for barium isotopes"**
   H. Utsunomiya, T. Renstrøm, G. M. Tveten, S. Goriely, T. Ari-izumi, V. W. Ingeberg, B. V. Kheswa, Y.-W. Lui, S. Miyamoto, S. Hilaire, S. Péru, and A. J. Koning
   Physical Review C 100, 034605 (2019).

3. **"Erratum: Photoneutron cross-section measurements in the 209Bi(γ, xn) reaction with a new method of direct neutron-multiplicity sorting [Phys. Rev. C 96, 044604 (2017)] "**
   Gheorghe, H. Utsunomiya, S. Katayama, D. Filipescu, S. Belyshev, K. Stopani, V. Orlin, V. Varlamov, T. Shima, S. Amano, S. Miyamoto, Y.-W. Lui, T. Kawano, and S. Goriely
   Physical Review C 99, 059901 (2019).

4. **"Neutron emission spectrum from gold excited with 16.6 MeV linearly polarized monoenergetic photons"**
   Y. Kirihara, H. Nakashima, T. Sanami, Y. Namito, T. Itoga, S. Miyamoto, A. Takemoto, M. Yamaguchi, Y. Asano
   Journal of Nucl. Sci. Technol., vol. 57, no. 4, pp. 444–456 (2020).

5. **"FCI の正解率劣化に伴う心理プロセス"**
   庄司善彦
   大学の物理教育, Vo.25, No.3, pp.121-124.

6. **"FCI 項目への回答応答に存在する日米差の正解率劣化に伴う心理プロセス"**
   庄司善彦
   大学の物理教育, Vo. 26, No.1, pp.8-11.

7. **"Sparse modeling of chemical bonding in binary compounds"**
   Y. Kanda, H. Fujii, and T. Oguchi
   Science and Technology of Advanced Materials (STAM), 20, 1178 (2019).

8. **"Half-metallicity of the ferrimagnet Mn2VAl revealed by resonant inelastic soft x-ray scattering in a magnetic field"**
   R. Y. Umetsu, H. Fujiwara, K. Nagai, Y. Nakatani, M. Kawada, A. Sekiyama, F. Kuroda, H. Fujii, T. Oguchi, Y. Harada, J. Miyawaki, and S. Suga
   Phys. Rev. B 99, 134414 (2019).

9. **"Local Structure Analysis on Si-Containing DLC Films Based on the Measurement of C K-Edge and Si K-edge X-Ray Absorption Spectra"**
   Kazuhiro Kanda, Shuto Suzuki, Masahito Niibe, Takayuki Hasegawa, Tsuneo Suzuki, Hedetoshi Saitoh
   Coatings, 10, 00330 (2020).
   doi:10.3390/coatings10040440

10. **"Effect of nonequilibrium atmospheric pressure O_2 plasma-assiated annealing on anatase TiO_2 nanoparticls"**

Retsuo Kawakami, Yuki Yoshitani, Akihiro Shirai, Shin-ichiro Tanagiya, Hirofumi Koide, Yuki Mimoto, Kosuke Kajikawa, Masahito Niibe, Yoshitaka Nakano, Chisato Azuma, Takashi Mukai
Appl. Surf. Sci. 526, 146684 (2020).
doi: 10.1016/j.apsusc.2020.146684

11. **"Removal of Surface Contamination by Atomic Hydrogen Annealing"**
Akira Heya, Tetsuo Harada, Masahito Niibe, Koji Sumitomo, and Takeo Watanabe
J. Photopolymer Sci. Technol., 33, 419-426 (2020).

12. **"Electronic structure of a 3x3-ordered silicon layer on Al(111)"**
Yusuke Sato, Yuki Fukaya, Mathis Cameau, Asish K. Kundu, Daisuke Shiga, Ryu Yukawa, Koji Horiba, Chin-Hsuan Chen, Angus Huang, Horng-Tay Jeng, Taisuke Ozaki, Hiroshi Kumigashira, Masahito Niibe, and Iwao Matsuda
Phys. Rev. Mater., 4, 064005 (2020).
DOI: 10.1103/PhysRevMaterials.4.06405.

13. **"Topological Dirac nodal loops in nonsymmorphic hydrogenated monolayer boron"**
N. T. Cuong, I. Tateishi, M. Cameau, M. Niibe, N. Umezawa, B. Slater, K. Yubuta, T. Kondo, M. Ogata, S. Okada, and I. Matsuda
Phys. Rev. B 101, 195412 (2020).
DOI: 10.1103/PhysRevB.101.195412

14. **"Charge redistribution within platinum-nitrogen coordination structure to boost hydrogen evolution"**
Xing Cheng, Yue Lu, Lirong Zheng, Yitao Cui, Masahito Niibe, Takashi Tokushima, Hongyi Li, Yuefei Zhang, Ge Chen, Shaorui Sun, and Jiujun Zhang
Nano Energy 73, 104739 (2020).
DOI: 10.1016/j.nanoen.2020.104739

15. **"Water Electrolysis Using Thin Pt and RuOx Catalysts Deposited by a Flame-Annealed Method on Pencil-Lead Graphite-Rod Electrodes"**
Ryuki Tsuji, Yuuki Koshino, Hideaki Masutani, Yuich Haruyama, Masahito Niibe, Satoru Suzuki, Seiji Nakashima, Hironori Fujisawa, and Seigo Ito
ACS Omega, 5, 6090-6099 (2020) .
DOI: 10.1021/acsomega.Oc00074.

16. **"Development of Soft X-rayAbsoeption Spectroscopic Equipment at Atmospheric Pressure Using He-path with a Free-Standing Membrane as a Partition Wall"**
Masahito Niibe, Yuka Horikawa, Takashi Tokushima
Adv. X-ray Chem. Anal. Japan, 51, 41-48 (2020).

17. **"Effect of air-based nonequilibrium atmospheric pressure plasma jet treatment on characteristics of polypropylene film surfaces"**
Retsuo Kawakami, Yuki Yoshitani, Kimiaki Mitani, Masahito Niibe, Yoshitaka Nakano, Chisato Azuma, Takashi Mukai
Appl. Surf. Sci. 509, 144910 (2020).

18. **"Dopamine detection on activated reaction fieldconsisting of graphene-integrated siliconphotonic cavity"**
R. Kou, Y. Kobayashi, S. Inoue, T. Tsuchizawa, Y. Ueno, S. Suzuki, H. Hibino, T. Yamamoto, H. Nakajima, K. Yamada
Optics Express 27, 32058-32068 (2019).

19. **"Growth process of hexagonal boron nitride in the diffusion and precipitation method studied by X-ray photoelectron spectroscopy"**
Satoru Suzuki and Yuichi Haruyama
Jpn. J. Appl. Phys. 58, SIIB15-1-4 (2019).

20. **"Water Electrolysis using Flame-Annealed Pencil-Graphite Rods"**
R. Tsuji, H. Masutani, Y. Haruyama, M. Niibe, S. Suzuki, S. Honda, Y. Matsuo, A. Heya, N. Matsuo, S. Ito
ACS Sustainable Chem. Eng. 7, 5681 (2019).

21. **"Quasi-free-standing monolayer hexagonal boron nitride on Ni"**
Satoru Suzuki, Yuichi Haruyama, Masahito Niibe, Takashi Tokushima, Akinobu Yamaguchi, Yuichi Utsumi, Atsushi Ito, Ryo Kadowaki, Akane Maruta and Tadashi Abukawa
Mater. Res. Express 6, 016304-1-8 (2019).

22. **"At wavelength coherent scatterometry microscope using high-order harmonics for EUV mask inspection"**
Yutaka Nagata, Tetsuo Harada, Takeo Watanabe, Hiroo Kinoshita, and Katsumi Midorikawa
Int. J. Extrem. Manuf. 1 (2019) 032001.

23. **"Development of an EUV and OoB Reflectometer at NewSUBARU Synchrotron Light Facility"**
Keisuke Tsuda, Tetsuo Harada, Takeo Watanabe
Proc. SPIE 11148 (2019) 111481N.

24. **"Resonant Soft X-ray Scattering for the Stochastic Origin Analysis in EUV Resist"**
Jun Tanaka, Takuma Ishiguro, Tetsuo Harada, and Takeo Watanabe
J. Photopolym. Sci. Technol. 32 (2019) pp. 327-331.

25. **"Resonant Soft X-ray Reflectivity for the Chemical Analysis in Thickness Direction of EUV Resist"**
Takuma Ishiguro, Jun Tanaka, Tetsuo Harada, and Takeo Watanabe
J. Photopolym. Sci. Technol. 32 (2019) pp. 333-337.

26. **"Energy- and spatial-resolved detection using a backside-illuminated CMOS sensor in the soft X-ray region"**
Tetsuo Harada, Nobukazu Teranishi, Takeo Watanabe, QUan Zhou, Xiao Yang, Jan Bogaerts, and Xinyang Wang
Appl. Phys. Exp. 12 (2019) 082012.

27. **"Fabrication of hig-aspect-ratio transmission grating using DDR process for 10 nm EUV resist evaluation by EUV interference lithography"**
Mana Yoshifuji, Shota Niihara, Tetsuo Harada, and Takeo Watanabe
Jpn. J. Appl. Phys. 58 (2019) SDDA02.

28. **"High-exposure-durability, high-quantum-efficiency (>90%) backside-illuminated soft-X-ray CMOS sensor"**
T. Harada, N. Teranishi, T. Watanabe, Q. Zhou, J. Bogaerts, X. Wang
Appl. Phys. Exp. 13 (2020) 103009.（Peer reviewed）

29. **"Synthesis and Property of Tellurium-Containing Molecular Resist Materials for Extreme Ultraviolet Lithography System"**
Hiroto Kudo, Mari Fukunaga, Teppei Yamada, Shinji Yamakawa, Takeo Watanabe, Hiroki Yamamoto, Kazumasa Okamoto, Takahiro Kozawa
J. Photopolym. Sci. Technol., 32 (2020) 805-810.

30. **"EUV Lithographic Technology for the Innovative IoT and AI (in Japanese) "**
Takeo Watanabe
Clean Technology, 2 (2020) pp.1-5.

31. **"Magnetic scattering in Ni wires fabricated on ferroelectric LiNbO3 substrate for magnetic sensor application"**
R. Nakamura, S. Saegusa, S. Suzuki, A. Nakao, Y. Utsumi, T. Ohkochi, M. Oura, Y. Takizawa, T. Saiki, T. Lee, K. Kim, K. Yamada, T. Ogasawara, A. Yamaguchi
Sensors and Materials 31, 3007-3022 (2019).

32. **"Controllability of cupric particle synthesis by linear alcohol chain number as additive and pH control in cupric acetate solution using X-ray radiolysis"**
A. Yamaguchi, I. Okada, I. Sakurai, H. Izumi, M. Ishihara, T. Fukuoka, S. Suzuki, K. Elphick, E. Jackson, A. Hirohata, Y. Utsumi
J. Synchrotron Rad. 26(6), 1986-1995 (2019).

33. **"Deep X-ray lithography system with a uniform and high-accuracy fabrication area establish in beamline BL11 at NewSUBARU"**
Masaya Takeuchi, Akinobu Yamaguchi, and Yuichi Utsumi
Journal of Synchrotron Radiation, Vol.26, pp.528-534, 2019

34. **"Deposition of Polytetrafluoroethylene Film Assisted by Synchrotron Radiation Irradiation"**
Masaya Takeuchi, Hirokazu Izumi, Mari Ishihara, Toshiro Kobayashi, Akinobu Yamaguchi, and Yuichi Utsumi
Journal of Photopolymer Science and Technology, Vol. 32, pp. 249-252 (2019). (IF : 0.934)

35. **"Modification of the Transmittance of Bulk Polytetrafluoroethylene via Synchrotron Radiation Irradiation"**
Masaya Takeuchi, Toshiro Kobayashi, Akinobu Yamaguchi, and Yuichi Utsumi
Journal of Photopolymer Science and Technology, Vol. 32, pp. 253-256 (2019). (IF : 0.934)

36. **"Improving the mixing performance of a 3D lab-on-a-chip device by using fluid dynamics simulation"**
Toshiro Kobayashi, Yuhei Yoshimasa, Masaya Takeuchi, Yuichi Utsumi, and Akinobu Yamaguchi
Advanced Experimental Mechanics, 4, 55- 60 (2019).

37. **"Measuring Elastic and Plastic Properties of PVK and CBP Thin Films using Triangular Pyramid Indenter"**
Toshiro Kobayashi, Hideaki Furumoto, Akinobu Yamaguchi, Hideyuki Kanemitsu, and Ion Cosmin Gruescu
Advanced Experimental Mechanics, 4, 96-102 (2019).

38. **"Present status of photoemission electron microscope newly installed in SPring-8 for time-resolved nanospectroscopy"**
Takuo Ohkochi, Hitoshi Osawa, Akinobu Yamaguchi, Hidenori Fujiwara, Masaki Oura
Jpn. J. Appl. Phys. 58, 118001-1-3 (2019). (IF : 1.471)

39. **"Cracking of Aluminum and Silver Alloy Thin Films on Polymer Thin Films"**
Toshiro Kobayashi, Hideaki Furumoto, Shigeru Nagasawa, Hideyuki Kanematsu, Ion Cosmin Gruescu, Yuichi Utsumi
Advanced Experimental Mechanics, Vol.4, 115-120 (2019).

Proceedings

1. **"Analysis of Students' University Selection Reports"**
   Y. Shoji
   Proc. of DSIR, IEEE Explore

2. **"Cognitive Acceleration Program in UndergraduateSchool"**
   Y. Shoji, T. Yumoto
   Proc. of DSIR, IEEE Explore

3. **"Analysis of LWR Origin in EUV Resist"**
   Takeo Watanabe, Jun Tanaka1 and Tetsuo Harada
   Proceedings of ALC'19, 2019.

4. **"Removal of carbon contamination on oxidation-prne metal coated mirrors using atomic hydrogen"**
   Masato Niibe, Tetsuo Harada, Akira Heya, Takeo Watanabe, and Naoto Matsuo
   AIP Conf. Proc. 2054, 060010 (2019).

5. **"EUV Lithography Research and Development Activities in Japan (Plenary Talk) "**
   Takeo Watanabe
   Proceedings of EUVL International Workshop, Jun. 2019, Berkeley, CA, USA, Jun. 13, 2019.

6. **"Photopolymer Science and Technology Related to EUV Lithography at University of Hyogo"**
   Takeo Watanabe
   Proceedings pf APSMR Annual Meeting 2019, Sapporo, July 26-29, 2019

7. **"EUVL fundamental works at University of Hyogo (Invited) "**
   Takeo Watanabe
   Proceedings of International Symposium on EUV Lithography 2019, Monterey, USA, Sep. 17, 2019.

8. **"Technical Issues in EUV Lithography (in Japanese) (Invited) "**
   Takeo Watanabe
   231st Photopolymer Conference, Tokyo University of Science, Apr. 25, 2019.

9. **"Advanced Research and Prospect at NewSUBARU Synchrotron Light Facility (in Japanese) "**
   Takeo Watanabe
   Proceedings of 135th Issui-Kai Conference, Jul. 26, 2019.

10. **"Resist Technology for Advanced Lithography (in Japanese) (Invited) "**
    Takeo Watanabe
    Proceedings of 29th Photopolymer Conference, Tokyo University of Science, Aug. 28-29, 2019.

11. **"Technology R&D for EUV Lithography (in Japanese) (Invited) "**
    Takeo Watanabe
    Proceedings of EUVL Seminar, Technical Information Institute, Co., Ltd., Dec. 5, 2019.

12. **"Fundamental Technology for EUV Lithography ～Advanced Technology Information, and Solution for the Technical Issues, and Prospect for the Future Technology～ (in Japanese) "**
    Takeo Watanabe
    Proceedings of Science and Technology Seminar, Science & Technology, Co., Ltd., pp.1-300, Jan. 30m 2019.

13. **"Anisotropic pyrochemical etching of PTFE by Synchrotron radiation"**

M. Takeuchi, A. Yamaguchi, and Y. Utsumi
Proceedings of the 14th Annual IEEE International Conference on Nano/Micro Engineered and Molecular Systems (IEEE-NEMS) April 11-14, 2019, Bangkok, Thailand, pp. 418-422

14. **"Study on three dimensional additive manufacturing process using X-ray radiolysis"**
Akinobu Yamaguchi, Ikuya Sakurai, Ikuo Okada, Atsushi Yamaguchi, Mari Ishihara, Takao Fukuoka, Satoru Suzuki, and Yuichi Utsumi
Proceedings of the 14th Annual IEEE International Conference on Nano/Micro Engineered and Molecular Systems (IEEE-NEMS) April 11-14, 2019, Bangkok, Thailand, pp. 139-142

15. **"X-ray radiolysis-based three dimensional additive manufacturing process"**
S. Saegusa, I. Sakurai, I. Okada, T. Fukuoka, S. Suzuki, Y. Utsumi, and A. Yamaguchi
2019 International Conference on Electronics Packaging (ICEP), April 17 -20, 2019

16. **"On-chip Synthesis of An Nanoparticles by Microwave-induced Reaction in Microchannel Embedded in the Post-Wall Waveguide"**
Yamaguchi, M. Kishihara, T. Fukuoka, M. Takeuchi, and Y. Utsumi
The 23rd International Conference on Miniaturized Systems for Chemistry and Life Science (μTAS 2019).

Review

1. **"マテリアルズ・インフォマティクスによる材料開発"**
藤井将
工業材料, 2019 年 6 月号 vol67, No.6, p78 日刊工業新聞社

2. **"軟 X 線を用いた逆コンプトン散乱による高エネルギーガンマ線ビームの開発"**
村松憲仁，岡部雅大，鈴木伸介，伊達仲，清水肇，大熊春夫，神田一浩，宮本修治，原田哲男，渡邊健夫，宮部学，時安敦史
加速器, 16(3), 154-160 (2019).

3. **"放射光光励起反応とプロセスへの展開"**
山口明啓，櫻井郁也，岡田育夫，内海裕一
エレクトロニクス実装学会, 2020 年 23 巻 1 号, pp. 46-52.

1. **"Development of a positron annihilation measurement system by implantation of 17 MeV gamma beam into bulk materials"**
   K. Sugita, S. Miyamoto, M. Terasawa, A. Iwase, K. Umezawa, and F. Hori
   AIP Conference Proceedings2182, 040007 (2019) : https://doi.org/10.1063/1.5135839
   The 18th International Conference on Positron Annihilation (ICPA-18)

2. **"GDR cross sections updated in the IAEA-CRP"**
   H. Utsunomiya, I. Gheorghe, K. Stopani, S. Belyshev, H. Wang, G. Fan, T. Ari-izumi, Y.-W. Lui, D. M. Filipescu, D. Symochko, M. Krzysiek, S. Miyamoto
   ND2019 (International Conference on Nuclear Data for Science and Technology, May 19-24, 2019: China National Convention Center, Beijing)
   http://nd2019.medmeeting.org/Content/78040

3. **"Development of the gamma-ray tracking detector at RCNP and its performance test at NewSUBARU"**
   Kohda, Y. Yamamoto, N. AOI, E. Ideguchi, M. K. Raju, H. Thi Ha, T. T. Pham, S. Miyamoto, T. Shizuma, N. Imai, K. Wimmer, P. Doornenbal, M. L. Cortes, J. Hwang
   High Resolution Gamma-Ray Spectroscopy at the RIBF, TU Darmstadt, Germany April 10, 2019

4. **"Fast positron beam penetration and annihilation in materials"**
   K. Sugita, S. Miyamoto, M. Terasawa, K. Umezawa and F. Hori
   SLOPOS15, (2019) Sep. 2-6 Prague, Czech.

5. **"Development of high energetic gamma beam induced positron annihilation apparatus at NewSUBARU"**
   Kento Sugita, Shuji Miyamoto, Mititaka Terasawa, Satoshi Hashimoto, Sho Amano, Kenji Umezawa, Fuminobu Hori
   16th. Particle Accelerator Society of Japan, p.126 (2019)

6. **"Automatic operation of NewSUBARU ring for automatic energy variable measurement of Compton scattered gamma rays"**
   Satoshi Hashimoto, Shuji Miyamoto, Yasuyuki Minagawa, Kazuyuki Kajimoto
   16th. Particle Accelerator Society of Japan, p.1052 (2019)

7. **"Present status of the NewSUBARU synchrotron light facility"**
   Satoshi Hashimoto, Yoshihiko Shoji, Shuji Miyamoto, Yasuyuki Minagawa, Kazuyuki Kajimoto, Yousuke Hamada
   16th. Particle Accelerator Society of Japan, p.1254 (2019)

8. **"Analysis of Students' University Selection Reports"** (Oral)
   Yoshihiko Shoji
   International Congress on Advanced Applied Informatics, July 7-12, 2019, Toyama, Japan

9. **"Cognitive Acceleration Program in Undergraduate School"** (Oral)
   Yoshihiko Shoji
   International Congress on Advanced Applied Informatics, July 7-12 ,2019, Toyama, Japan

10. **"Characterization of amorphous carbon films using near edge X-ray absorption fine structure measurement"** [invited]
    Kazuhiro Kanda
    The ASIAN Conference on X-ray Absorption Spectroscopy 2019 (ACXAS2019), 2019.8.28-30

Chiangmai, Thailand

11. **"NEXAFS evaluation for the lumen of DLC coated small diameter long-sized medical objective tube by using AC high-voltage burst plasma CVD method"**
Yuichi Imai, Kazuhiro Kanda, Yasuhiro Fujii, Susumu Ouzawa, Daiki Ousaka, Tatsuyuki, Nakatani
12th International Symposium on Advanced Plasma Science and its Applications for Nitrides and Nanomaterials / 13th International Conference on Plasma-Nano Technology & Science (ISPlasma2020/IC-PLANTS2020), 10P2-52, March 8-11, Nagoya University (Higashiyama Campus), Nagoya, Japan, (2020)

12. **"Nano-polycryetalline diamond and compressed graphite systhesized from neutron-irradiated highly oriented pyrolytic graphite"**
Keisuke Niwase, Mititaka Terasawa, Shin-ichi Honda, Masahito Niibe, Masafumi ichikawa, Shusaku Nakamura, Yuji Higo
32nd Advanced Materials World Congress (IAAM), Sydney, Australia, Feb. 2-5, 2020.

13. **"Soft X-ray Absorption and Emission Spectra of Monolayer h-BN film"**
Masahito Niibe, Satoru Suzuki, and Takashi Tokushima
20th Int'l Symp. On Boron Borides and Related Materials (ISBB), Niigata Japan, 22-27, Sep. 2019.

14. **"Soft X-ray Absorption and Emission Spectra of Trace Boron doped in HOPG"**
Masahito Niibe, Noritaka Takehira, and Takashi Tokushima
20th Int'l Symp. On Boron Borides and Related Materials (ISBB), Niigata Japan, 22-27, Sep. 2019.

15. **"Study of Electroic Structure of Silicene on Al(111) Substrate"**
Y. Sato, Y. Fukaya, C. H. Chen, A. Huang, H. T. Jeng, M. Niibe, and I. Matsuda
20th Int'l Symp. On Boron Borides and Related Materials (ISBB), Niigata Japan, 22-27, Sep. 2019.

16. **"Electron trrucuture of rare-earth aluminum/chromium boride R(Al0.95Cr0.05)B4 studied by B-K soft X-ray emission and absorption spectroscopy"**
Masahito Niibe, M. Cameou, N.T. Cuong, T. Kindo, K. Yubuta, S. Okada and I. Matsuda
The 40th Int'l Conf. on Vacuum Ultraviolet and X-ray Physics (VUVX19), San Francisco USA, 1-5, July 2019.

17. **"Photocatalytic Characteristics of Au/TiO2/Au Nanostructure Induced by Ultraviolet Irradiation"**
Retsuo Kawakami, Hirofumi Koide, Yuki Yoshitani, Shin-ichiro Yanagiya, Toshihiro Okamoto, Masanobu Haraguchi, Akihiro Furube, Masahito Niibe, Yoshitaka Nakano, Chisato Azuma and Takashi Mukai
15th International Symposium on Sputtering & Plasma Processes, Kanazawa Japan, Jun. 2019.

18. **"Laser-plasma-source for soft X-ray microscope"** (Invited)
S.Amano
6th International Congress on Microscopy & Spectroscopy (INTERM2019), Oludeniz, Turkey, May 12-18, 2019.

19. **"Development of Time-Division Depth-Profiling Techniques in Multi- Layered Dielectric Thin Films by using Near-Ambient-Pressure Hard X-ray Angle-Resolved Photoemission Spectroscopy"**
Satoshi Toyoda, Tomoki Yamamoto, Masashi Yoshimura, Hirosuke Sumida, Susumu Mineoi, Masatake Machida, Akitaka Yoshigoe, Akira Yoshikawa, Satoru Suzuki, Kazushi Yokoyama
2019 Int. Workshop on Dielectric Thin Films for Future Electron Devices – Science and Technology – (2019 IWDTF), Tokyo, November 19, 2019.

20. **"Preparation and Characterization of Graphene/Bi(Fe,Mn)O3 Structure on SrRuO3-buffered SrTiO3 Substrate"**
S. Nakashima, S. Yamagata, Y. Fuchiwaki, S. Suzuki, and H. Fujisawa
Materials Research Meeting 2019 (MRM2019), Yokohama, December 11, 2019.

21. **"Time series analysis of depth profiles in multi-layered stack-film interfaces studied by near-ambient-pressure hard x-ray angle-resolved photoemission spectroscopy"**
Satoshi Toyoda, Tomoki Yamamoto, Masashi Yoshimura, Hirosuke Sumida, Susumu Mineoi, Masatake Machida, Akitaka Yoshigoe, Akira Yoshikawa, Satoru Suzuki, Kazushi Yokoyama
Int. Conf. on Materials and Systems for Sustainability 2019 (ICMaSS2019), Nagoya, November 1, 2019.

22. **"EUV Lithography Research and Development Activities in Japan"** (Plenary Talk)
Takeo Watanabe
EUVL International Workshop, Jun. 2019, Berkeley, CA, USA, Jun. 13, 2019.

23. **"Resonant Soft X-ray Reflectivity for the Chemical Analysis in Thickness Direction of EUV Resist"**
Takuma Ishiguro, Jun Tanaka, Tetsuo Harada, and Takeo Watanabe
ICPST36, Chiba, Japan, Jun. 25, 2019.

24. **"Resonant Soft X-ray Scattering for the Stochastic Origin Analysis in EUV Resist"**
Jun Tanaka, Takuma Ishiguro, Tetsuo Harada, and Takeo Watanabe
ICPST36, Chiba, Japan, Jun. 25, 2019.

25. **"Photopolymer Science and Technology Related to EUV Lithography at University of Hyogo"** (Invited)
Takeo Watanabe
Proceedings pf APSMR Annual Meeting 2019, Sapporo, July 26-29, 2019.

26. **"Fundamental Studies of EUV Resist at the NewSUBARU Synchrotron Light Source"** (Invited)
Takeo Watanabe and Testuo Harada
ELENA International Conference 2019, Lueven, Belgium, Sep. 4, 2019.

27. **"Development of an EUV and OoB Reflectometer in NewSUBARU Synchrotron light Facility"** (Invited)
Keisuke Tsuda, Tetsuo Harada, Takeo Watanabe
Speed Presentation on BACUS 2019, Monterey, USA, Sep. 17, 2019.

28. **"EUVL fundamental works at University of Hyogo"** (Invited)
Takeo Watanabe, Tetsuo Harada
International Symposium on EUV Lithography 2019, Monterey, USA, Sep. 17, 2019.

29. **"Fundamental Research Activities of Extreme Ultraviolet Lithography at NewSUBARU Synchrotron Facility"**
Takeo Watanabe and Tetsuo Harada
MNE2020, Rhodes, Greece, Sep. 23, 2019.

30. **"Development of VUV and soft X-ray reflectometers for EUV-optics and optical-index measurements in NewSUBARU"**
Tetsuo Harada, Takeo Watanabe
XIO 2019, Sendai, Japan, Oct. 26, 2019,

31. **"Development of High-Power EUV Irradiation Tool in Hydrogen Atmosphere"**
Ayato Ohgata, Tetsuo Harada, and Takeo Watanabe
MNC2019, Hiroshima, Japan, Oct. 28, 2019.

32. **"EUV Resist Research Activites at NewSUBARU"**
Takeo Watanabe
IEUVI Resist International Workshop 2020
San Jose, USA, Feb. 23, 2019.

33. **"Future EUV lithography with shortening the wavelength"**
Takeo Watanabe, Takuto Fujii, Fuuka Yoshizawa, Hironori Matsumoto, Takuma Ishiguro, and Tetsuo Harada
Speed Talk at SPIE Advanced Lithography 2020, San Jose, USA, Feb. 26, 2019.

34. **"The evaluation method of the origin of LWR in EUV resist"**
Takeo Watanabe and Tetsuo Harada
SPIE Advanced Lithography 2020, San Jose, USA, Feb. 27, 2019.

35. **"Development of an EUV and OoB Reflectometer in NewSUBARU Synchrotron light Facility"**
Keisuke Tsuda, Tetsuo Harada, Takeo Watanabe
Photomask Japan 2019, Yokohama, Japan, Apr. 16, 2019.

36. **"Development of High-Power EUV Irradiation tool in H2 atmosphere"**
Ayato Ohgata, Tetsuo Harada, Takeo Watanabe
Photomask Japan 2019, Yokohama, Japan, Apr. 16, 2019.

37. **"Development of an EUV and OoB Reflectometer in NewSUBARU Synchrotron light Facility"** (Invited)
Keisuke Tsuda, Tetsuo Harada, Takeo Watanabe
Poster Session on BACUS 2019, Monterey, USA, Sep. 17, 2019.

38. **"Development of high-power EUV irradiation tool in hydrogen atmosphere"**
Tetsuo Harada, Ayato Ohgata, Takeo Watanabe
International Symposium on EUV Lithography 2019, Monterey, USA, Sep. 17, 2019.

39. **"The stochastic origin analysis using the resonant soft X-ray scattering method in EUV resists"** (Invited)
Takeo Watanabe, Tetsuo Harada, Jun Tanaka, Takuma Ishiguro
International Symposium on EUV Lithography 2019, Monterey, USA, Sep. 16, 2019.

40. **"Analysis of LWR Origin in EUV Resist"**
Takeo Watanabe, Jun Tanaka, and Tetsuo Harada
ALC '19, Kyoto, Oct. 21, 2019.

41. **"Future EUV lithography with shortening the wavelength"**
Takeo Watanabe, Takuto Fujii, Fuuka Yoshizawa, Hironori Matsumoto, Takuma Ishiguro, and Tetsuo Harada
SPIE Advanced Lithography 2020, San Jose, CA, USA, Feb. 27, 2020.

42. **"Study on three dimensional additive magnufacturing process using X-ray radiolysis"**

Akinobu Yamaguchi, Ikuya Sakurai, Ikuo Okada, Atsushi Yamaguchi, Mari Ishihara, Takao Fukuoka, Satoru Suzuki, Yuichi Utsumi
IEEE NEMS April 11th, 2019.

43. **"Anisotropic pyrochemical etching of PTFE by Synchrotron radiation"** (Oral)
Masaya Takeuchi, Akinobu Yamaguchi, Yuichi Utsumi
IEEE NEMS April 11th, 2019.

44. **"X-ray radiolysis-based three dimensional additive manufacturing process"** (Oral)
S. Saegusa, I. Sakurai, I. Okada, T. Fukuoka, S. Suzki, Y. Utsumi, and A. Yamaguchi
20th International Conference on Electronic Packaging (ICEP 2019), April 17th – 20th, 2019, Toki-messe, Nigata, Japan

45. **"Study on the physical mechanism of uniaxial magnetic anisotropy induced in Ni layer on LiNbO3 substrate"** (Oral)
Yamaguchi, T. Ohkochi, M. Oura, K. Yamada, Y. Utsumi, A. Nakao
10th International Symposium on Metallic Multilayers (MML), June 17th-21st, 2019, IMDEA Nanocienciain Campus Universitario de Cantoblanco, Spain

46. **"Enhancement of damping constant in Ni wire deposited on LiNbO3 substrate"** (Poster)
Yamaguchi, K. -J. Kim, A. Nakao, and K. Yamada
10th International Symposium on Metallic Multilayers (MML), June 17th-21st, 2019, IMDEA Nanocienciain Campus Universitario de Cantoblanco, Spain

47. **"Deposition of Polytetrafluoroethylene Assisted by Synchrotron Radiation Irradiation"** (Oral)
M. Takeuchi, H. Izumi, M. Ishihara, T. Kobayashi, A. Yamaguchi, Y. Utsumi
The 36th International Conference of Photopolymer Science and Technology, June 25th-27th, 2019, Makuhari Messe

48. **"Modification of the Transmittance of Bulk Polytetrafluoroethylene via Synchrotron Radiation Irradiation"** (Oral)
Masaya Takeuchi, Toshiro Kobayashi, Akinobu Yamaguchi, and Yuichi Utsumi
The 36th International Conference of Photopolymer Science and Technology, June 25th-27th, 2019, Makuhari Messe

49. **"Additive manufacturing process by X-ray-induced-photochemical reaction"** (Oral)
A. Yamaguchi, I. Okada, I. Sakurai, S. Saegusa, Y. Utsumi
The 10th Japan-China-Korea Join Conference on MEMS/NEMS, 2019, July 16th-18th, Asahikawa, Japan

50. **"Thermal Evaporation of a Polytetrafluoroethylene Film Under AtmosphericPressure Assisted by Synchrotron Radiation Pre-Irradiation"** (Oral)
M. Takeuchi, A. Yamaguchi, Y. Utsumi
The 10th Japan-China-Korea Join Conference on MEMS/NEMS, 2019, July 16th-18th, Asahikawa, Japan

51. **"XPS and XMCD-PEEM Studies of uniaxial magnetic anisotropy induced in Ni layer deposited on LiNbO3 substrate"**
A. Yamaguchi, T. Ohkochi, M. Oura, K. Yamada, A. Naoko, Y. Utsumi
10th Joint European Magnetic Symposia, August 26th-30th, 2019, Uppsala Konsert & Kongress, Uppsala, Sweden

52. **"Evaluation of Gilbert damping in magnetic wires on LiNbO3 using rectifying effect"**
A. Yamaguchi, K. –J. Kim, T. Lee, A. Nakao, T. Ohkochi, K. Yamada
10th Joint European Magnetic Symposia, August 26th-30th, 2019, Uppsala Konsert & Kongress, Uppsala, Sweden

53. **"Study on X-ray radiolysis-induced-chemical reaction at interface between liquid and substrate for additive manufacturing process"** (Poster)
A. Yamaguchi, I. Sakurai, I. Okada, M. Ishihara, T. Fukuoka, K. Elphick, E. Jackson, A. Hirohata, Y. Utsumi
45th International conference on micro & nano engineering, September 23rd-26th, 2019, in Rhodes island, Greece.

54. **"Ferromagnetic/Ferroelectric heterojunction-induced modulation of magnetic properties of artificial magnets"** (Poster)
A. Yamaguchi, R. Nakamura, S. Saegusa, K. Yamada, T. Saiki, A. Nakao, Y. Utsumi, T. Ogasawara, M. Oura, T. Ohkochi
45th International conference on micro & nano engineering, September 23rd-26th, 2019, in Rhodes island, Greece.

55. **"On-chip synthesis of ruthenium complex in a microchannel by microwave heating"** (Poster)
M. Takeuchi, M. Kishihara, T. Kobayashi, A. Yamaguchi, T. Matsumura-Inoue, Y. Utsumi
45th International conference on micro & nano engineering, September 23rd-26th, 2019, in Rhodes island, Greece.

56. **"On-chip synthesis of Au nanoparticles by microwave-induced reaction microchannel embedded in the post-wall waveguide"** (Poster)
A. Yamaguchi, M. Kishihara, T. Fukuoka, M. Takeuchi, Y. Utsumi
The 23rd International Conference on Miniaturized Systems for Chemistry and Life Science, (μTAS 2019) October 27th-31st, 2019, Congress Center Basel, Basel, Switzerland

57. **"Anisotropic pyrochemical etching of polytetrafluoroethylene by soft X-ray"** (Poster)
K. Fujitani, M. Takeuchi, A. Yamaguchi, Y. Utsumi
MNC 2019, October 28th-31st, 2019,Hiroshima, Japan

58. **"Aggregation and dispersion of Au-nanoparticles and decorated polystyrene beads with SERS-activity in optofluidic chip"** (Oral)
A. Yamaguchi, Y. Utsumi, T. Fukuoka
Okinawa Colloids 2019, November 3rd-8th, 2019, Bankoku Shinryoukan, Okinawa, Japan

59. **"Longevous Plasmonic Nanotags for On-dose-authentication of Medical Tables in Supply Chain Security"** (Poster)
T. Fukuoka, H. Nakanishi, Y. Mori, A. Yamaguchi
Okinawa Colloids 2019, November 3rd-8th, 2019, Bankoku Shinryoukan, Okinawa, Japan

60. **"Study on magnetization dynamics in magnetic wires on LiNbO3"** (Oral)
S. Saegusa, R. Nakamura, T. Ogasawara, Y. Utsumi, K. Yamada, T. Ohkochi, T. Kinoshita, M. Oura, and A. Yamaguchi
Materials Research Meeting 2019, December 10th-14th, 2019, Yokohama, Japan

61. **"Study on mechanism and control of uniaxial magnetic anisotropy induced in the**

ferromagnetic/ferroelectric heterojunction using XMCD-PEEM and XPS" (Poster)
R. Nakamura, S. Saegusa, A. Nakao, Y. Utsumi, K. Yamada, T. Ohkohic, T. Kinoshita, M. Oura, and A. Yamaguchi
Materials Research Meeting 2019, December 10th-14th, 2019, Yokohama, Japan

Ph.D. (Engineering)

Masaya Takeuchi (University of Hyogo)
"Construction of deep x-ray lithography platform for microstructures with high aspect-ratio and precision and its applications"

Master of Science

Tomoki Yamamoto (University of Hyogo)
"Soft X-ray photoemission spectroscopy of Au/Si in oxygen atmosphere and automatic analysis of the experimental data"

Master of Engineering

Mana Yoshifuji (University of Hyogo)
"Fabrication of High Aspect Ratio Transmissive Diffraction Grating for 10 nm EUV Resist Resolution Evaluation"

Laboratory of Advanced Science and Technology for Industry
University of Hyogo

3-1-2 Kouto, Kamigori, Ako-gun, Hyogo 678-1205 Japan

兵庫県立大学 高度産業科学技術研究所
〒678-1205 兵庫県赤穂郡上郡町光都 3-1-2